

3-11-2011

# Radiation Effects on the Electrical Properties of Hafnium Oxide Based MOS Capacitors

Jesse C. Foster

Follow this and additional works at: <https://scholar.afit.edu/etd>

Part of the [Nuclear Commons](#)

---

## Recommended Citation

Foster, Jesse C., "Radiation Effects on the Electrical Properties of Hafnium Oxide Based MOS Capacitors" (2011). *Theses and Dissertations*. 1449.

<https://scholar.afit.edu/etd/1449>

This Thesis is brought to you for free and open access by the Student Graduate Works at AFIT Scholar. It has been accepted for inclusion in Theses and Dissertations by an authorized administrator of AFIT Scholar. For more information, please contact [richard.mansfield@afit.edu](mailto:richard.mansfield@afit.edu).



**RADIATION EFFECTS ON THE  
ELECTRICAL PROPERTIES OF HAFNIUM  
OXIDE BASED MOS CAPACITORS**

THESIS

Jesse C. Foster, Captain, USAF  
AFIT/GNE/ENP/11-M07

**DEPARTMENT OF THE AIR FORCE  
AIR UNIVERSITY**

**AIR FORCE INSTITUTE OF TECHNOLOGY**

**Wright-Patterson Air Force Base, Ohio**

APPROVED FOR PUBLIC RELEASE; DISTRIBUTION UNLIMITED

The views expressed in this thesis are those of the author and do not reflect the official policy or position of the United States Air Force, the Department of Defense or the United States Government. This material is declared a work of the U.S. Government and is not subject to copyright protection in the United States.

AFIT/GNE/ENP/11-M07

RADIATION EFFECTS ON THE ELECTRICAL PROPERTIES OF HAFNIUM  
OXIDE BASED MOS CAPACITORS

THESIS

Presented to the Faculty  
Department of Engineering Physics  
Graduate School of Engineering and Management  
Air Force Institute of Technology  
Air University  
Air Education and Training Command  
in Partial Fulfillment of the Requirements for the  
Degree of Master of Science in Nuclear Engineering

Jesse C. Foster, B.S.N.E.  
Captain, USAF

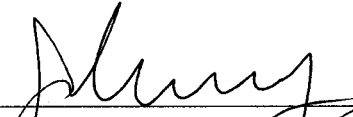
March 2011

APPROVED FOR PUBLIC RELEASE; DISTRIBUTION UNLIMITED

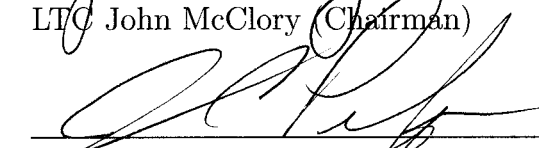
RADIATION EFFECTS ON THE ELECTRICAL PROPERTIES OF HAFNIUM  
OXIDE BASED MOS CAPACITORS

Jesse C. Foster, B.S.N.E.  
Captain, USAF

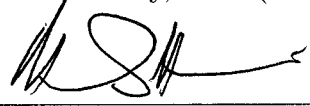
Approved:

  
\_\_\_\_\_  
LTC John McClory (Chairman)

6 Mar 11  
\_\_\_\_\_  
Date

  
\_\_\_\_\_  
James Petrosky, PhD (Member)

4 Mar 11  
\_\_\_\_\_  
Date

  
\_\_\_\_\_  
LtCol Christopher Williams (Member)

2 Mar 2011  
\_\_\_\_\_  
Date

## **Abstract**

Hafnium oxide-based MOS capacitors were investigated to determine electrical property response to radiation environments. In situ capacitance versus voltage measurements were analyzed to identify voltage shifting as a result of changes to trapped charge with increasing dose of gamma, neutron, and ion radiation. In situ measurements required investigation and optimization of capacitor fabrication to include dicing, cleaning, metalization, packaging, and wire bonding. A top metal contact of 200 angstroms of titanium followed by 2800 angstroms of gold allowed for repeatable wire bonding and proper electrical response. Gamma and ion irradiations of atomic layer deposited hafnium oxide on silicon devices both resulted in a midgap voltage shift of no more than 0.2 V toward less positive voltages. This shift indicates recombination of radiation induced positive charge with negative trapped charge in the bulk oxide. Silicon ion irradiation caused interface effects in addition to oxide trap effects that resulted in a flatband voltage shift of approximately 0.6 V also toward less positive voltages. Additionally, no bias dependent voltage shifts with gamma irradiation and strong oxide capacitance room temperature annealing after ion irradiation was observed. These characteristics, in addition to the small voltage shifts observed, demonstrate the radiation hardness of hafnium oxide and its applicability for use in space systems.

## Acknowledgements

This work could not have been completed without the support of many outstanding individuals. The first person that requires my thanks is my wife for her love, support, and most importantly her patience. Next my mother, for her love, support and for always being there both in mind and spirit. Last but certainly not least, my dad for always listening, understanding, and helping me through many difficulties.

The experimental work in this research effort afforded many opportunities and greatly added to my learning experience. In spite of rarely garnering the support of my committee, I would like to thank them for trusting my judgment and granting me the flexibility to guide much of my own learning. I understand that this flexibility was partly due to the enormous work load carried on a daily basis to make this program second to none. They should know that their efforts are recognized and greatly appreciated. Lastly, this type of work is seldom done without outstanding financial support. For this I specifically thank both LTC John McClory and Dr. James Petrosky.

I wish to thank the University of Nebraska-Lincoln for providing the PLD samples for this work. Without those samples, HfO<sub>2</sub> research would not have been started. Collaboration has been very beneficial for both AFIT and UNL. Taking the time to provide samples that are outside the research focus is recognized and greatly appreciated.

I spent a lot of time in and around the AFIT clean room primarily in the first two months of research. During this time Mr. Greg Smith provided excellent support. He taught me several different wafer prepping procedures as well as went out of his way on several occasions to help solve my electrical property issues. Additionally, I would like to thank Mr. Rich Johnson for taking the time to assist me with many metalizations. Rick, Rich, and Greg do an outstanding job in operating and maintaining the clean

room and providing support to many students.

The folks at AFRL were instrumental in the success of this work. This research could not have been completed without several individuals. They assisted specifically with metalizations, packaging and wire bonding, and providing samples to use in this work.

The gamma and neutron irradiations were performed at the Ohio State Nuclear Reactor Lab. I wish to thank the Associate Director, the Senior Research Associate, and both Senior Reactor Operators for their outstanding support of both the gamma and neutron experiments. I especially wish to thank the Senior Research Associate for taking the time to assist with experimental setups and with performing the activation analysis experiments that provided optimal flux height and the neutron energy spectrum. The OSURR personnel expertise and flexibility in working with AFIT students is nothing short of exceptional. The ion irradiations were performed at the Ion Beam Laboratory at Sandia National Laboratories. I spent two weeks at this facility and wish to thank the many individuals who made my visits not only a success but also very rewarding.

Jesse C. Foster



# Table of Contents

	Page
Abstract .....	iv
Acknowledgements .....	v
List of Figures .....	ix
List of Tables .....	xiii
List of Abbreviations .....	xiv
I. Introduction .....	1
1.1 Focus of Research .....	2
1.2 Outline of Thesis .....	3
II. Theory and Background .....	5
2.1 Radiation Effects .....	9
2.2 Previous Research .....	10
III. Device Preparation .....	14
3.1 Plasma Laser Deposition .....	15
3.2 Atomic Layer Deposition .....	16
3.3 Device Fabrication .....	16
3.3.1 Dicing .....	17
3.3.2 Polishing .....	18
3.3.3 Cleaning .....	19
3.3.4 Metalization .....	20
3.3.5 Annealing .....	24
3.3.6 Packaging and Wire Bonding .....	25
IV. Experimental Procedures .....	30
4.1 Gamma Irradiation Equipment and Dosimetry .....	30
4.2 Neutron Irradiation Equipment and Dosimetry .....	33
4.3 Ion Irradiation Equipment and Dosimetry .....	37
4.4 Data Collection .....	45
4.5 Pre-Characterization .....	49
4.6 Irradiations .....	59

	Page
V. Experimental Results .....	60
5.1 Rutherford Backscattering Results .....	60
5.2 Gamma Irradiation Results .....	63
5.3 Neutron Irradiation Results .....	66
5.4 Ion Irradiation Results .....	68
VI. Analysis and Discussion .....	74
6.1 Oxide Trapped Charge .....	75
6.2 Interface Trapped Charge .....	82
6.3 Annealing Effects .....	88
VII. Conclusions .....	91
Bibliography .....	95

## List of Figures

Figure	Page
1. Conceptual illustration of the creation of electron-hole pairs and displacement damage in a n-type silicon metal-oxide-silicon capacitor. . . . .	5
2. Conceptual illustration of the creation of electron-hole pairs and displacement damage in a p-type silicon substrate metal-oxide-silicon capacitor. . . . .	6
3. Illustration of the effect, in a CV plot, of oxide trapped charge for a hypothetical n-type device. . . . .	7
4. Illustration of the effect, in a CV plot, of oxide trapped charge for a hypothetical p-type device. . . . .	8
5. Illustration of the effect, in a CV plot, of interface trapped charge for a hypothetical n-type device. . . . .	8
6. Illustration of the effect, in a CV plot, of interface trapped charge for a hypothetical p-type device. . . . .	9
7. Thicknesses of all layers in the MOS capacitors used. . . . .	15
8. Diamond saw cutter . . . . .	17
9. Buehler MiniMet 1000 used for polishing . . . . .	19
10. Before and after pictures of polishing wafers . . . . .	20
11. Electron beam evaporator . . . . .	21
12. Copper crucible . . . . .	21
13. Electron beam evaporator shutter . . . . .	22
14. Electron beam evaporator mount . . . . .	23
15. Electron beam evaporator chamber . . . . .	23
16. Rapid Thermal Annealer . . . . .	25
17. Ultrasonic Compression Wedge Wire Bonder . . . . .	26

Figure	Page
18.	16-pin dual in-line package with sample . . . . . 27
19.	ALD metal contact diameter picture . . . . . 27
20.	Gamma irradiator pins . . . . . 31
21.	Gamma irradiator equipment setup . . . . . 31
22.	Gamma irradiator dose rate plot as function of height . . . . . 32
23.	Reactor pool illustration . . . . . 34
24.	Neutron profile . . . . . 35
25.	Neutron energy spectrum . . . . . 36
26.	Tandem accelerator . . . . . 38
27.	Ion beam analysis beam line . . . . . 39
28.	Ion beam analysis beam line mount . . . . . 40
29.	QASPR III beam line vacuum chamber . . . . . 40
30.	QASPR III beam line sample mounting . . . . . 41
31.	QASPR III beam line end station . . . . . 41
32.	Ionization plot from SRIM . . . . . 42
33.	Paper grid picture from QASPR III camera . . . . . 44
34.	Illuminated phosphorous strip picture . . . . . 44
35.	Error bar plot for measurement equipment used . . . . . 46
36.	Pre-irradiation CV plot for PLD #4 . . . . . 49
37.	Pre-irradiation CV plot for PLD #3 . . . . . 50
38.	Pre-irradiation CV plot for PLD #2 . . . . . 51
39.	Pre-irradiation CV plot for PLD #1 . . . . . 51
40.	Pre-irradiation CV plot for PLD #6 . . . . . 52

Figure	Page
41. PLD pin hole pictures . . . . .	53
42. PLD pre-irradiation IV plot . . . . .	53
43. ALD pre-irradiation IV plot . . . . .	54
44. ALD pre-irradiation CV plot . . . . .	55
45. ALD pre-irradiation GV plot . . . . .	56
46. ALD pre-irradiation adjusted capacitance plot . . . . .	57
47. ALD pre-irradiation adjusted conductance plot . . . . .	57
48. 50 nm SiO <sub>2</sub> conductance plot . . . . .	58
49. PLD Rutherford Backscattering spectrum . . . . .	62
50. ALD Rutherford Backscattering spectrum . . . . .	63
51. PLD #4: 0 V bias gamma irradiation results . . . . .	64
52. PLD #3: 5 V bias gamma irradiation results . . . . .	65
53. ALD #20: 0 V bias gamma irradiation results . . . . .	65
54. ALD #21: 5 V bias gamma irradiation results . . . . .	66
55. PLD #2: 0 V bias neutron irradiation results . . . . .	67
56. PLD #1: 5 V bias neutron irradiation results . . . . .	67
57. PLD #1: 5 V bias neutron irradiation conductance . . . . .	68
58. PLD #6: $1.5 \times 10^{11} \frac{\text{ions}}{\text{cm}^2}$ : irradiations 1-6 result . . . . .	69
59. PLD #6: $1.5 \times 10^{11} \frac{\text{ions}}{\text{cm}^2}$ : irradiations 6-10 result . . . . .	69
60. ALD #22: $10^8 \frac{\text{ions}}{\text{cm}^2}$ result . . . . .	70
61. ALD #22: $10^8 \frac{\text{ions}}{\text{cm}^2}$ trend . . . . .	71
62. ALD #23: $5 \times 10^8 \frac{\text{ions}}{\text{cm}^2}$ result . . . . .	72
63. ALD #23: $5 \times 10^8 \frac{\text{ions}}{\text{cm}^2}$ trend . . . . .	73

Figure	Page
64. ALD #20: normalized capacitance 0 V bias gamma irradiation plot .....	76
65. ALD #20: change in oxide trap density 0 V bias gamma irradiation plot .....	76
66. ALD #21: normalized capacitance 5 V bias gamma irradiation plot .....	78
67. ALD #21: change in oxide trap density 5 V bias gamma irradiation plot .....	78
68. ALD #22: normalized capacitance of pre- and post-irradiation #10 of $10^8 \frac{ions}{cm^2}$ irradiations .....	80
69. ALD #22: normalized capacitance trend of $10^8 \frac{ions}{cm^2}$ irradiations .....	80
70. ALD #22: change in oxide trap density of $10^8 \frac{ions}{cm^2}$ irradiation plot .....	81
71. ALD #23: Normalized capacitance of pre- and post-irradiation #10 of $5 \times 10^8 \frac{ions}{cm^2}$ irradiations .....	82
72. ALD #23: normalized capacitance trend of $5 \times 10^8 \frac{ions}{cm^2}$ irradiations .....	83
73. ALD #23: change in oxide trap density of $5 \times 10^8 \frac{ions}{cm^2}$ irradiation plot .....	83
74. Substrate doping density plot .....	85
75. ALD #23: change in interface trap density of $5 \times 10^8 \frac{ions}{cm^2}$ irradiation plot .....	86
76. 3 CV voltage sweeps illustrating annealing effects .....	88
77. Annealing oxide capacitance vs. irradiation # plot .....	89
78. Normalized capacitance for 3 voltage sweeps .....	90

## List of Tables

Table		Page
1.	Device Assembly Steps .....	17
2.	Metal Contact Summary .....	28
3.	Sample Preparation Summary .....	29
4.	Data Gathering Equipment Summary .....	48
5.	Irradiations Summary .....	59
6.	PLD RBS Results Summary .....	62
7.	ALD RBS Results Summary .....	63
8.	PLD #6: $1.5 \times 10^{11} \frac{\text{ions}}{\text{cm}^2}$ Irradiation Summary .....	70
9.	ALD #22: $10^8 \frac{\text{ions}}{\text{cm}^2}$ Irradiation Summary .....	71
10.	ALD #23: $5 \times 10^8 \frac{\text{ions}}{\text{cm}^2}$ Irradiation Summary .....	73
11.	ALD #20: 0 V Gamma Oxide Trap Analysis .....	77
12.	ALD #21: 5 V Gamma Oxide Trap Analysis .....	79
13.	ALD #22: $10^8 \frac{\text{ions}}{\text{cm}^2}$ Oxide Trap Analysis .....	81
14.	ALD #23: $5 \times 10^8 \frac{\text{ions}}{\text{cm}^2}$ Oxide Trap Analysis .....	84
15.	ALD #23: $5 \times 10^8 \frac{\text{ions}}{\text{cm}^2}$ Interface Trap Analysis .....	86
16.	$C_{OX}$ at -1 V for 10 Irradiations of $5 \times 10^8 \frac{\text{ions}}{\text{cm}^2}$ .....	89

## List of Abbreviations

Abbreviation		Page
SiO <sub>2</sub>	silicon dioxide . . . . .	1
DoD	Department of Defense . . . . .	1
HfO <sub>2</sub>	Hafnium dioxide . . . . .	1
TID	Total Ionizing Dose . . . . .	2
NIEL	Non-Ionizing Energy Loss . . . . .	2
EHPs	electron-hole pairs . . . . .	2
PLD	Pulsed Laser Deposition . . . . .	3
ALD	Atomic Layer Deposition . . . . .	3
MOSCAP	Metal Oxide Semiconductor Capacitor . . . . .	3
CV	capacitance versus voltage . . . . .	5
MOSFET	Metal Oxide Semiconductor Field Effect Transistor . . . . .	9
IC	integrated circuit . . . . .	9
V <sub>FB</sub>	flatband voltage . . . . .	11
V <sub>MG</sub>	midgap voltage . . . . .	12
AFRL	Air Force Research Laboratory . . . . .	16
PDA	Post Deposition Annealing . . . . .	24
GIF	Gamma Irradiation Facility . . . . .	30
ASTM	American Society for Testing and Materials . . . . .	32
CPE	charged particle equilibrium . . . . .	32
OSURR	Ohio State University Research Reactor . . . . .	33
IBL	Ion Beam Laboratory . . . . .	37
SNL	Sandia National Laboratory . . . . .	37



Abbreviation	Page
RBS	Rutherford Backscattering . . . . . 37
IBA	Ion Beam Analysis . . . . . 38
QASPR	Qualification Alternatives to the Sandia Pulsed Reactor . . . . . 39
BNC	Bayonet Neill-Concelman . . . . . 39
SRIM	Stopping Range of Ions in Matter . . . . . 42
GV	conductance versus voltage . . . . . 46
IV	Current versus voltage . . . . . 48
SIMNRA	Simulation for Nuclear Reaction Analysis . . . . . 60
$C_{MG}$	midgap capacitance . . . . . 75

# RADIATION EFFECTS ON THE ELECTRICAL PROPERTIES OF HAFNIUM OXIDE BASED MOS CAPACITORS

## I. Introduction

The study of high- $\kappa$  dielectrics to replace silicon dioxide ( $\text{SiO}_2$ ) is of interest to the Department of Defense (DoD) due to the potential improvement in the operational lifetime and performance of semiconductor devices in high radiation environments. Semiconductor manufacturers are incorporating high- $\kappa$  dielectrics in commercial electronics to reduce leakage current as oxide gates are designed thinner to improve device speed [1]. Unlike in terrestrial applications, the Air Force is concerned with radiation effects.  $\text{SiO}_2$  has been thoroughly studied for the past several decades and is known to be sensitive to radiation. This sensitivity not only affects device performance but also affects power consumption. Increased power consumption reduces the operational lifetime of non-solar powered space systems. High- $\kappa$  material radiation response has not been studied nor understood to the level of  $\text{SiO}_2$ . Therefore, if high- $\kappa$  based devices are to be used as key components in space power and control systems, the radiation response must be well understood.

Many gate oxides have been studied to replace  $\text{SiO}_2$ . Hafnium dioxide ( $\text{HfO}_2$ ) has emerged as a leader [2].  $\text{HfO}_2$  demonstrates attractive material properties: high dielectric constant (25), wide band gap (5.8 eV), and thermodynamic stability with silicon [3]. Additionally,  $\text{HfO}_2$  gates have been found to be unresponsive to gamma irradiation [4, 5]. Gamma irradiation is known to be a major contributor to device failure in  $\text{SiO}_2$  based devices. Other research has found strong resistance to heavy ion-induced oxide breakdown [6]. A single heavy ion event along with large capacitance

and high voltage has been suspected of destroying  $\text{SiO}_2$  insulators. This radiation induced failure is only compounded when the  $\text{SiO}_2$  is designed thinner, which results in even higher electric fields. These two results bode well for utilizing  $\text{HfO}_2$  as a gate oxide for space application. However, other research remains to be conducted including resistance to displacement damage.

## 1.1 Focus of Research

The space radiation environment contains protons, electrons, neutrons, heavy charged particles, and gamma rays. Oxide material exposed to this radiation exhibits Total Ionizing Dose (TID) effects and Non-Ionizing Energy Loss (NIEL) displacement damage effects. This work explores both by experimentally measuring the capacitance as a function voltage. This is performed on  $\text{HfO}_2$ -based devices before, during, and after gamma, neutron, and ion irradiation. The gamma irradiation addresses TID and potentially results in the formation of trapped charge both in the bulk oxide and at the oxide/silicon interface from the creation of electron-hole pairs (EHPs). Neutron and ion irradiation addresses NIEL that potentially results in the formation of trapped charge created from the displacement of hafnium and oxygen atoms.

This work was originally intended to determine the damage equivalence between neutron and ion irradiation of  $\text{HfO}_2$ . The damage equivalence between the two irradiation types would prove useful for future irradiations; if only one was performed, the damage from the other type could be predicted. Additionally, electrical measurements from both of these irradiations indicate  $\text{HfO}_2$ 's resistance to displacement damage effects. Gamma irradiation was also desired for comparison to other types of radiation and to obtain charge yield. Charge yield is the ratio of the number of EHPs produced to the amount of trapped charge produced in the oxide. This is useful in order to understand which radiation has a greater effect on the oxide's electrical

properties. This work unfolded very differently for reasons to be discussed throughout this thesis. Voltage shifts due to charge trap formation or elimination became the primary focus.

This research also investigated device preparation, fabrication, and oxide thickness verification. All samples consisted of  $\text{HfO}_2$  deposited on silicon substrate by either Pulsed Laser Deposition (PLD) or Atomic Layer Deposition (ALD). Metal contacts were needed in order to make in situ electrical measurements. A significant portion of the research effort involved determining optimal device preparation and fabrication for the purpose of taking electrical measurements. Oxide thickness was important for capacitance calculations, therefore certainty in these values was established through ion backscattering measurements.

## 1.2 Outline of Thesis

An outline of this thesis is included in order to gain understanding of what is included in this document beyond the table of contents. Chapter 2 begins by describing Metal Oxide Semiconductor Capacitor (MOSCAP) charge trapping theory. Models for radiation interaction with oxide material is discussed in terms of ionizing and non-ionizing radiation. Lastly, previous work involving  $\text{HfO}_2$ -based MOSCAP electrical response to radiation is discussed.

Chapter 3 briefly describes the details of PLD and ALD samples. This includes substrate type, resistivity, and oxide thickness. Since  $\text{HfO}_2$  deposition techniques and methods were not the focus of this work, these methods are not explored in detail. Device preparation and fabrication was a significant undertaking in this work and key steps are described including equipment, procedures, difficulties, and rationale for the techniques employed.

Chapter 4 provides details of all irradiation equipment. This includes details of

the gamma irradiator, nuclear reactor, and ion beam lines. Radiation effects experiments require the use of dosimetry to determine irradiation time and total dose. An explanation of how dose was calculated is presented since each irradiation was unique. Additionally, measurement equipment is discussed to include advantages and limitations encountered during experimentation. Pre-characterization of PLD and ALD devices is presented to highlight the differences in device electrical response before irradiation. Lastly, an irradiation summary table is presented to illustrate the scope of work.

Chapter 5 and 6 presents the raw results and analyses respectively from all irradiations. Chapter 7 gives a summary of device responses, as well as arguments for what causes them. Lessons learned are included in an effort to inform future researchers. Lastly, recommendations are provided to influence the direction of this research.

## II. Theory and Background

The voltage shifts that occur in capacitance versus voltage (CV) measurements indicate oxide and interface charge trap formation or elimination. Since this work researched  $\text{HfO}_2$  deposited on both n- and p-type silicon substrates, conceptual illustrations of traps are shown for both substrate types in Figures 1 and 2 respectively.

Gamma irradiation can cause ionization, or in other words, the creation of EHPs

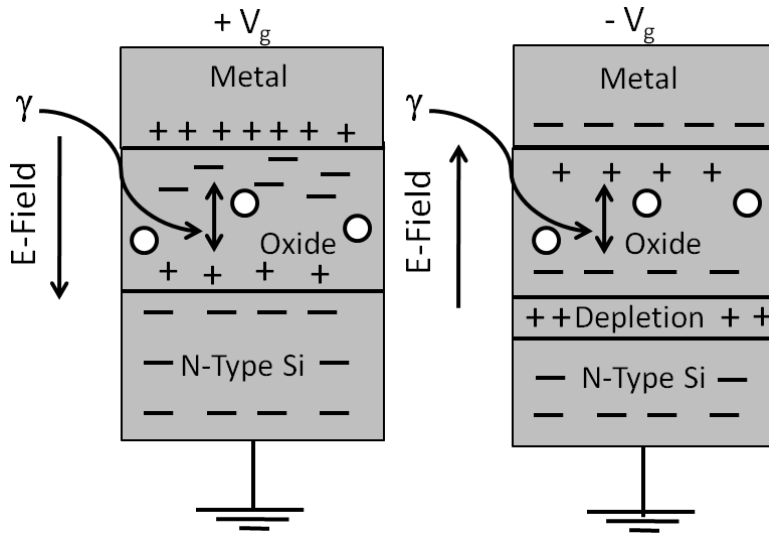


**Figure 1.** Irradiation creates electron-hole pairs or displacement damage sites in the oxide that can trap charge. An n-type device is shown where the depletion region is formed with a large negative gate bias. The variation of the depletion region thickness with gate bias is what changes the capacitance as a function of voltage and defines a CV plot.

through exciting valence band electrons in oxide molecules to conduction band energy levels. Neutron and ion irradiation can indirectly cause the creation of EHPs similarly to gamma irradiation as they slow down with increasing depth in the oxide. However, neutrons and ions can additionally dislodge oxide atoms and create displacement damage in the form of vacancies or interstitials. An electric field, created by the application of a gate voltage, can separate EHPs and make them mobile. The movement of these charges to either of the metal contacts through the oxide can be

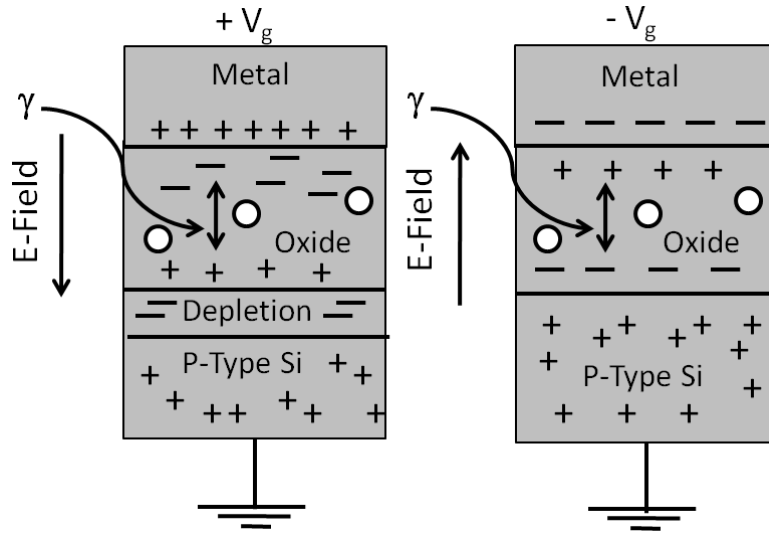


**Figure 2.** Irradiation creates electron-hole pairs or displacement damage in the oxide. A p-type device is shown where the depletion region is formed with a large positive gate bias. The variation of the depletion region thickness with gate bias is what changes the capacitance as a function of voltage and defines a CV plot.

impeded or stopped entirely by defects in the oxide. These defects are vacancies, interstitials, or dangling bonds that can be positively or negatively charged which could attract and trap mobile charge.

There were few expectations of how these irradiations would affect the oxide material. Some gamma irradiation expectations were provided in literature [4, 5]. Expectations in that work were strongly motivated by the pre-irradiation characteristics of the CV plot. Specifically, the pre-irradiation CV plots indicated whether the samples contained more positive or negative charge before irradiation. If the CV plots were near ideal without a high density of positive or negative charge, then shifting of the CV plot with irradiation would be dependent on what type of charge (positive or negative) was being trapped. However, if a high density of either positive or negative charge existed, then EHPs created in the oxide with irradiation could recombine with the high density charge thereby causing a shift in CV plots. Pre-characterization of the devices was therefore very important in this work and it shaped expectations.

Oxide trapped charge is evident by parallel voltage shifting of a CV plot. The effect

of oxide trapped charge in a hypothetical n-type device is illustrated in Figure 3. If

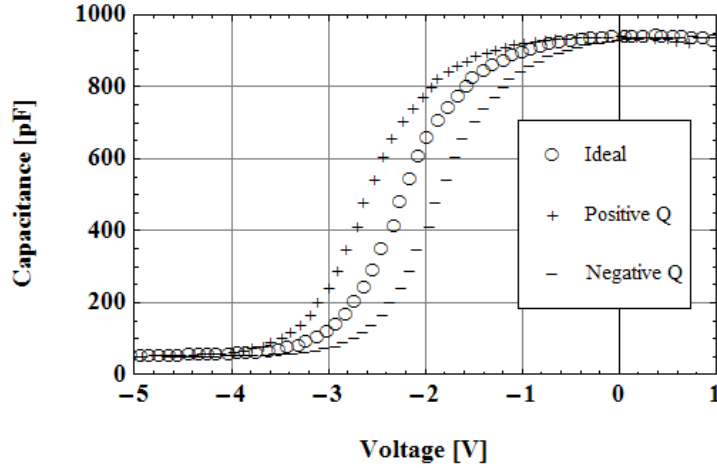


**Figure 3.** These plots illustrate the effect of oxide trapped charge for a hypothetical n-type device. If positive charge gets trapped or a recombination occurs for negatively trapped charge, the plot shifts to the left. If negative charge gets trapped or a recombination occurs for positively trapped charge, the plot shifts to the right.

positive charge was trapped or there was a decrease in negative trapped charge due to recombination, then a larger negative gate bias would need to be applied. This would shift the curve to the left. If negative charge was trapped or there was a decrease in positive trapped charge due to recombination, then a smaller negative gate bias would need to be applied. This would shift the curve to the right. The effect of oxide trapped charge in a hypothetical p-type device is illustrated in Figure 4. The parallel voltage shifting for a p-type device is explained in a similar fashion to that of a n-type device.

A change in interface trapped charge is evident in changes to the slope of a CV plot. The effect of interface trapped charge in a hypothetical n-type device is illustrated in Figure 5. The dynamics are not as simple as in oxide traps. In general, it is inferred that if net negative charge existed at the oxide/silicon interface then less negative gate bias would be needed resulting in a steeper slope. If net positive charge existed then more negative gate bias would be needed resulting in “stretch out” of the CV



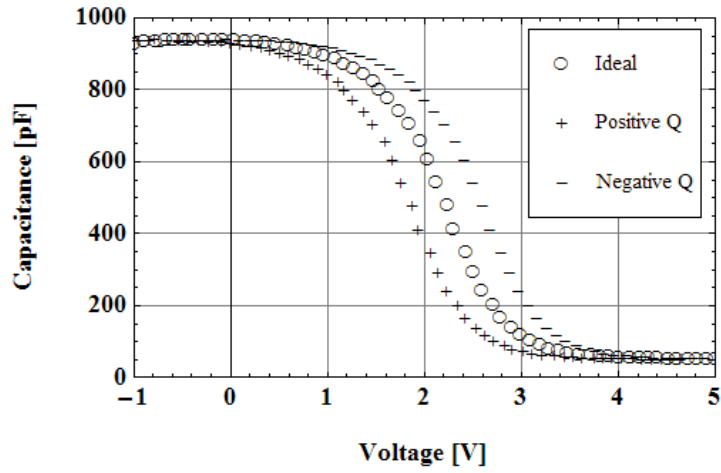


Figure 4. These plots illustrate the effect of oxide trapped charge for a hypothetical p-type device. If positive charge gets trapped or a recombination occurs for negatively trapped charge, the plot shifts to the left. If negative charge gets trapped or a recombination occurs for positively trapped charge, the plot shifts to the right.

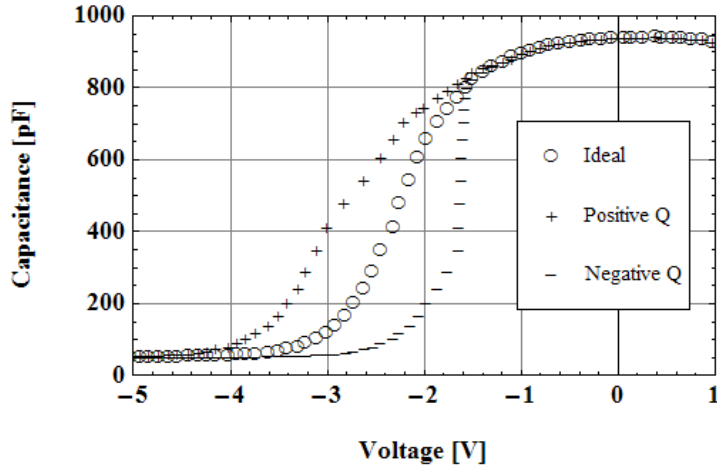


Figure 5. These plots illustrate the effect of interface trapped charge for a hypothetical n-type device. If net positive charge is trapped at the interface then the plot stretches out. If net negative charge is trapped at the interface then the plot becomes steeper.

plot. More specifically, it is not only that there are charges at the interface, but that the traps that hold the charge are in the silicon. Thus at one voltage the traps are empty, and as it changes, they become filled, inhibiting or enhancing the electric field, depending upon the charge that is trapped and field. The effect of interface trapped charge in a hypothetical p-type device is illustrated in Figure 6. Slope change for a p-type device is inferred in a similar fashion only opposite to a n-type device.

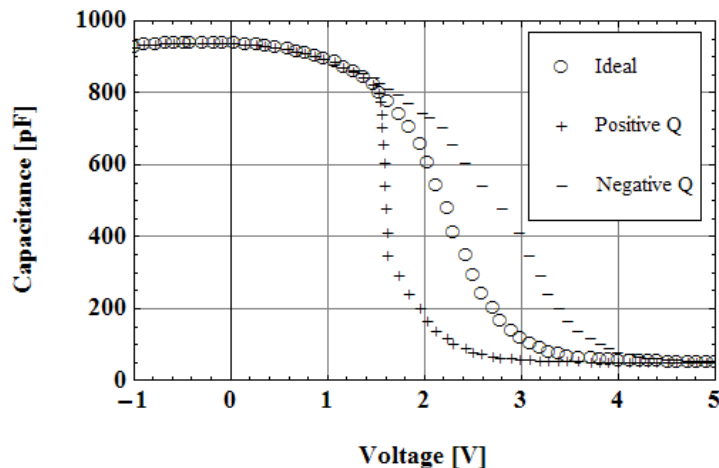


Figure 6. These plots illustrate the effect of interface trapped charge for a hypothetical p-type device. If net positive charge is trapped at the interface then the plot becomes steeper. If net negative charge is trapped at the interface then the plot stretches out.

## 2.1 Radiation Effects

This work employs the MOSCAP device for experimental testing. A MOSCAP was chosen because it represents the foundation for a Metal Oxide Semiconductor Field Effect Transistor (MOSFET). The MOSFET is the basic building block of an integrated circuit (IC). An observed change in a MOSCAP's operation will cause adverse effects in ICs. Radiation potentially cause changes in MOSCAPs operation through charge trapping, which can be measured. The changes in MOSCAP operation translate to changes in voltage at which a MOSFET is switched "on" or "off".

When gamma rays enter an oxide, they primarily create EHPs through ionization. These electrons and holes created in the oxide can immediately recombine, separate due to an electric field followed by recombination, separate and escape through metal contacts, or separate and form oxide or interface traps. A portion of this research is concerned with gamma irradiation total dose response of a HfO<sub>2</sub>-based MOSCAP both with and without a strong electric field. With no electric field electrons and holes are expected to either recombine, become trapped, or flow out of the oxide. With an electric field in the right direction, the charge can move to the oxide/silicon interface and become trapped at the interface. This behavior is known to occur in similar SiO<sub>2</sub>-based MOS devices. [7]

When neutrons impact a material, they either pass through the material with no interaction or lose energy by colliding with the atoms. When ions enter semiconductor material there are three possible outcomes: they pass through the material with no energy loss, lose their energy through ionization, or lose energy by colliding with the atoms. An additional portion of this research is concerned with NIEL of the particles in the oxide. NIEL is a measure of the energy transferred to the atoms of the oxide lattice during irradiation. The effect of neutrons or ions can change depending on particle type, target type, binding energy of the material, and energy of the bombarding particle. The primary NIEL effect is displacement damage of atoms leading to vacancies or interstitials [8]. These damage types potentially act as charge traps in the material that cause changes in electrical properties.

## 2.2 Previous Research

Most HfO<sub>2</sub> based MOS capacitor research has focused on TID effects and minimally on NIEL. This is not surprising since previous research with SiO<sub>2</sub> based MOS capacitors, as outlined on page 112 by Holmes-Siedle, indicate a larger vulnerability

to TID as opposed to NIEL [8]. Low and high total dose  $^{60}\text{Co}$  gamma irradiations have been performed by Ergin [4] and Kang [5] respectively. Related researchers performed 10 keV X-ray irradiations using hafnium-silicate capacitors [9, 10]. Little research has been found on NIEL effects due to ion or neutron irradiation. One related paper was found that studied heavy ion (340 MeV gold) induced breakdown in several different high- $\kappa$  MOS capacitors [6].

Ergin performed ex situ CV measurements with gamma irradiation at a dose range of 0.1-16 Gy with no bias on  $\text{HfO}_2$  based MOS capacitors of varying thicknesses. Gate voltage was varied from -4 to 2 V. A bidirectional voltage shift was found at 2 Gy. A positive flatband voltage ( $V_{FB}$ ) shift was attributed to acceptor-like interface states formed at low doses. Negative  $V_{FB}$  shift was explained by donor-like interface states at high dose. Oxide and interface trap density were extracted from CV plots, and used to calculate a trapping efficiency.  $\text{HfO}_2$  trapping efficiency was found to be three times smaller than  $\text{SiO}_2$ , and was attributed to a lower defect density in  $\text{HfO}_2$ .

Kang subjected (100) p-type silicon substrate  $\text{HfO}_2$  MOS capacitor samples to 10 Mrad(Si)  $^{60}\text{Co}$  gamma irradiation under both positive and negative bias. In addition to gamma irradiation, (111) silicon substrate samples were irradiated to 100 Mrad(Si) using ultraviolet irradiation from a 50 W deuterium lamp in a vacuum chamber. The most notable observation was the absence of stretch out in the CV relationship after irradiation. Stretch out in a CV curve is an indication interface traps. This is markedly different than  $\text{SiO}_2$  response to gamma irradiation as illustrated by Winokur [7]. Winokur showed stretch out with a small 30 krad( $\text{SiO}_2$ ) or 34 krad(Si) dose on  $\text{SiO}_2$  based capacitors. At 1 Mrad( $\text{SiO}_2$ ) or 1.13 Mrad(Si), the CV curve of  $\text{SiO}_2$  capacitors had shifted by approximately 5 V.

Over the course of Kang's measurements, he noted that interface dangling bonds ( $P_b$  centers) were not generated at a density greater than  $3 \times 10^{10}$  per  $\text{cm}^2$ , the pre-

cision of the ESR measurements used, after 10 Mrad(Si) gamma irradiation. This agrees with there being no CV stretch out. This result indicates that HfO<sub>2</sub> is intrinsically radiation harder. Two explanations were proposed to this result: 1) the absence of oxide dangling bonds (E' centers) or 2) blocking of hydrogenic movement toward the interface. This explanation started with relating HfO<sub>2</sub> to SiO<sub>2</sub>. In SiO<sub>2</sub> capacitors, P<sub>b</sub> centers and E' centers dominate trapping in the semiconductor. With SiO<sub>2</sub>, there is thermodynamic stability when hydrogen passivated P<sub>b</sub> centers are transferred into E' centers. Thermodynamic stability means that there is a reduction in Gibbs free energy. The argument is that in HfO<sub>2</sub> capacitors, the E' centers are not being generated, which gives little thermodynamic motivation for interface trap formation. The second explanation involves the motion of a hydrogenic species to the interface. This interface trap formation model in SiO<sub>2</sub> was established by Oldham [11]. Kang noted that hydrogenic motion might not be occurring at all. He states that similar blocking of hydrogen to the interface was found in nitrided oxides which somehow suppresses P<sub>b</sub> formation.

Before the thermal stability of HfO<sub>2</sub> on silicon was realized, some researchers used hafnium silicate (Hf<sub>8</sub>Si<sub>25</sub>O<sub>67</sub>) based MOS capacitors. It was suggested that hafnium could be developed initially as a silicate with the concentration of hafnium gradually increasing until processing techniques improved to deposit HfO<sub>2</sub> on silicon directly. Felix [9, 10] irradiated hafnium-silicate capacitors with 10 keV X-rays to total doses of 500 krad (SiO<sub>2</sub>) or 1000 krad (SiO<sub>2</sub>) respectively. The V<sub>FB</sub> and midgap voltage (V<sub>MG</sub>) linearly increases with dose, but both were significantly larger than thermal SiO<sub>2</sub> oxides of similar electrical thickness. Even though the shifts were larger, for practical hafnium silicate thicknesses in MOS devices, the V<sub>MG</sub> shift would be approximately 50 times lower, and hence would not rule out hafnium silicate as an option for use in MOS devices.

No research was found in the area of NIEL or displacement damage effects on HfO<sub>2</sub> based MOS capacitors. However, an understanding of the displacement damage effects on SiO<sub>2</sub> based MOS devices exists. Srour [12] illustrated that lifetime, mobility, and carrier concentration degrades with increasing neutron fluence according to the Messenger Spratt equation. This is shown as Equation 1,

$$\frac{1}{\tau} - \frac{1}{\tau_o} = k * \phi, \quad (1)$$

where  $\tau_o$  and  $\tau$  is charge carrier lifetime before and after irradiation respectively,  $k$  is the damage constant, and  $\phi$  is the fluence. The lifetime can be replaced by mobility or carrier concentration. This understanding was initially developed from Messenger and Spratt [13] in the form of gain degradation.

### III. Device Preparation

All samples used in the radiation effects experiments were  $\text{HfO}_2$  deposited on silicon with no capping layer. All experimental measurements were conducted in situ except for one ion irradiation. In situ measurements were preferred in order to maximize data and minimize variability in irradiation equipment. In situ allows continuous data gathering at specified time intervals throughout irradiations without having to remove devices for measurement. Ex situ would introduce variability from having to shut down irradiation equipment (reactor or ion beam) in order to remove a device from an irradiation chamber. Exact replication of irradiation between ex situ measurements could not be guaranteed. In situ measurements ensured integrity of observed effects by being able to rule out the possibility of effects seen due to variations in the irradiation equipment.

In general, each sample required dicing to fit in packages, application of metal contacts, and wire bonding to the contacts. Assembling these samples into devices proved to be a major undertaking in this research. The common device under investigation was the MOS capacitor. The major features of all devices used in this research is illustrated conceptually in Figure 7. In addition to device fabrication, two  $\text{HfO}_2$  samples were used: pulsed laser deposited and atomic layer deposited. ALD samples were obtained due to difficulty in interpreting CV plot characteristics of the PLD devices. The uncharacteristic CV plots of the PLD devices fueled a root cause investigation which included experimentation with various device assembly steps. This involved applying different types and thicknesses of metal contacts, polishing procedures, cleaning procedures, and annealing procedures.

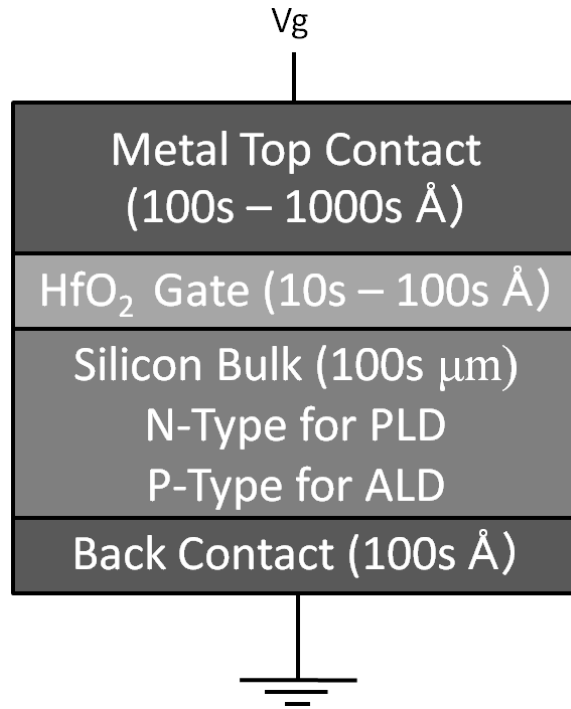


**Figure 7.** All MOS capacitor devices consisted of HfO<sub>2</sub> deposited on n- or p-type silicon and encased with top and bottom metal contacts.

### 3.1 Plasma Laser Deposition

The PLD HfO<sub>2</sub> samples were obtained from the University of Nebraska-Lincoln. HfO<sub>2</sub> was deposited on n-type silicon (100) substrate with 0.01-0.02 Ω·cm resistivity. The films were deposited at 300, 500, and 750°C at 2 different thicknesses. Additional details on the deposition of HfO<sub>2</sub> thin films on silicon substrate using PLD can be found in [14] and [15]. Due to the nonuniform deposition behavior of the process, thickness measurement results were not known with certainty. Thicknesses, measured on a needle point Tencor thin film measurement apparatus, ranged from 15 nm to more than 50 nm for both thin and thick samples. A Rutherford Backscattering experiment revealed thicknesses at approximately 80 nm and 150 nm for two separate thin samples. Further PLD characteristics are discussed in the pre-characterization section of the following chapter.



## 3.2 Atomic Layer Deposition

ALD samples of  $\text{HfO}_2$  were deposited on a Cambridge Nanotech Fiji F200 Atomic Layer Deposition System by Air Force Research Laboratory (AFRL) Sensors Directorate personnel. Tetrakis(dimethylamido)hafnium(IV) or  $(\text{Hf}[\text{N}(\text{CH}_3)_2]_4)_2$  was used as the  $\text{HfO}_2$  precursor. With silicon wafers and gas delivery lines heated to approximately  $250^\circ\text{C}$  and  $150^\circ\text{C}$  respectively,  $75^\circ\text{C}$  precursor was deposited for approximately 6.5 hours for a 50 nm sample at a nominal pressure of 0.19 Torr. All the depositions were performed on 1-10  $\Omega\cdot\text{cm}$  p-type silicon wafers. A wafer with 50 nm  $\text{HfO}_2$  was chosen for irradiation in this work. This wafer had a visible uniform oxide layer and the thickness was confirmed by Rutherford Backscattering experiments. Additional details and analysis of ALD deposition of  $\text{HfO}_2$  from other researchers can be found in [16] and [17].

## 3.3 Device Fabrication

In order to take in situ electrical measurements, the bare samples were assembled into MOS capacitor devices. This process included the steps shown in Table 1 with the exception that the polishing was not needed for the ALD samples because they contained doubled-sided polished silicon. Annealing was only attempted for several PLD samples in an effort to improve electrical characteristics through trap removal. Additionally, wire bonding was not possible for all samples due to the nature of the metal contacts. The correct metal contact recipe was discovered through much trial and error. All steps are explained with additional detail as to what is important or needed for device assembly in the following subsections. A summary of all samples is presented in the final subsection. A useful guide for MOS capacitors in general including device fabrication was found in a book by Nicollian and Brews [18] Chapter 12.9 pages 628-634.

**Table 1. Device Assembly Steps**

<b>Assembly Step</b>	<b>Description</b>	<b>Equipment Used</b>
Dicing	cut samples to fit packages	diamond saw cutter
Polishing	remove SiO <sub>2</sub>	polishing paper
Cleaning	remove organics	O <sub>2</sub> or ultrasonic cleaner
Metalization	apply contacts	evaporate or sputter
Annealing	remove defects, seat contact	rapid thermal annealer
Packaging	adhere sample to package	conductive silver epoxy
Wire Bonding	bond wire to contacts	ultrasonic compression wedge

### **3.3.1 Dicing.**

A 16-pin, dual in-line semiconductor package was selected to house the samples. This gave the necessary dimensions for the samples to fit inside the package. Samples were diced to approximately 20 mm<sup>2</sup>. This was performed on an automated MicroAce Loadpoint Limited diamond saw cutter as shown in Figure 8. The samples were

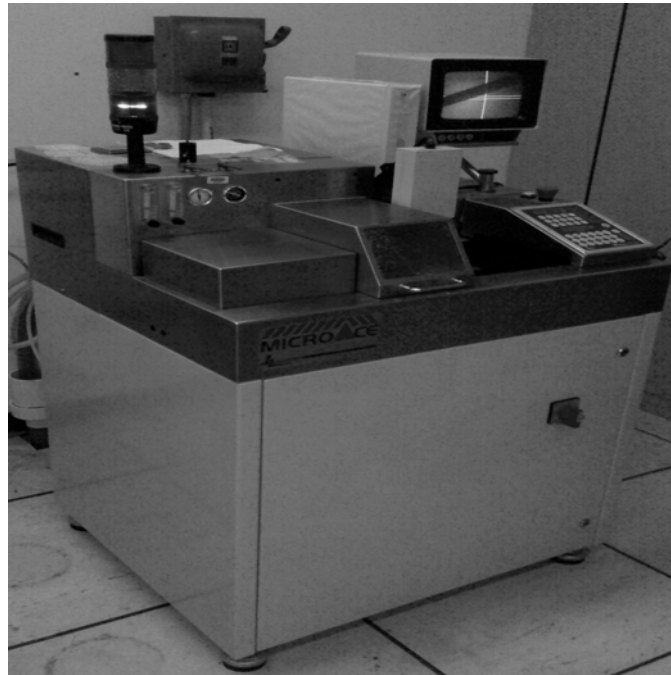


**Figure 8. HfO<sub>2</sub> samples were diced in approximately 20 mm<sup>2</sup> squares on an automated MicroAce Loadpoint Limited diamond saw cutter.**

mounted on thin plastic and heated to allow for sample adhesion to the plastic before

cutting. This was necessary in order to hold the samples in place during the cutting process. For most samples, dicing took place before metal contacts were applied. However, the ALD samples had metal contacts applied before cutting. AFRL had a large clean room where oxide deposition and metalization occurred in the same clean room. It was decided that applying contacts to one 2 inch diameter wafer followed by dicing as opposed to dicing followed by metalization and cleaning for each  $20 \text{ mm}^2$  was more efficient. In the case of metalization before dicing, the samples required a layer of photoresist in order to protect the contacts from being removed by the deionized water used to keep the saw cool during the cutting process. Photoresist is a light-sensitive material used in several industrial processes, such as photolithography and photoengraving to form a patterned coating on a surface. Photoresist was used in this case because it was readily available and could be removed easily with acetone without damaging the  $\text{HfO}_2$  layer after dicing.

### **3.3.2 Polishing.**

Only the PLD samples were polished. During PLD device pre-characterization, CV results were uncharacteristic. Upon examination of other bare PLD samples, a layer of  $\text{SiO}_2$  was identified on the backside. The  $\text{SiO}_2$  layer on the backside of the silicon substrate needed to be removed for electrical measurements. Common practice calls for chemically etching the silicon substrate with 1 percent HF solution followed by  $\text{HfO}_2$  and metal contact deposition [18]. However, in an effort not to degrade the  $\text{HfO}_2$  on the front side, the  $\text{SiO}_2$  layer was removed by grinding and polishing the backside silicon substrate with a Buehler MiniMet 1000 Grinder/Polisher shown in Figure 9. Both 600 grit and polishing paper in combination with an alpha alumina water mixture was used to remove the back oxide layer. This process was complete when the silicon backside changed from a dull rainbow to a glassy finish. Images of



**Figure 9.** The Buehler MiniMet 1000 was used to remove  $\text{SiO}_2$  from the backside of many PLD samples.

samples both before and after this process are shown in Figure 10. The samples are adhered to the Buehler mount by wax. The mount was placed on a heater and the samples placed in the melted wax on the mount. The mount was then allowed to cool so the samples did not move during polishing. Following polishing, the mount was reheated in order to remove the samples. The wax was removed from the samples with acetone. Since  $\text{SiO}_2$  grows very quickly on silicon, the samples were immediately taken to a clean room after polishing where ultrasonic cleaning was performed followed by backside metalization.

### **3.3.3 Cleaning.**

The samples required cleaning to ensure that there were no organic materials that could interfere with metal deposition. If this was not performed, the metal might not adhere to the oxide or substrate layer. This could lead to distorted electrical measurements and sample degradation. Two cleaning processes were used for this work, based on where the cleaning and metalization was performed. Ultrasonic cleaning took place inside the clean room. The samples were given a 5 minute ultrasonic bath

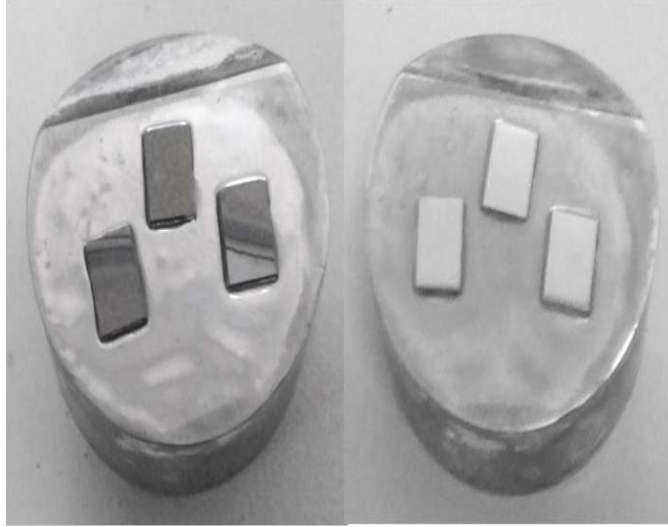


**Figure 10.** Both pictures show samples mounted in wax on the Buehler cylindrical attachment. The  $\text{SiO}_2$  side is facing up. The left picture is samples before polishing and the right is after. The  $\text{SiO}_2$  is removed when the dull rainbow is removed.

inside a beaker with acetone followed by methanol and isopropanol. The ultrasonic bath was performed in a Branson Ultrasonic Cleaner filled slightly with deionized water. The filled beaker with the samples was placed inside the deionized ultrasonic cleaner tub. Following cleaning, they were blown dry with  $\text{N}_2$  so as not to leave residue on samples that could interfere with metalization.  $\text{O}_2$  cleaning was also performed in a clean room. The samples were placed inside an  $\text{O}_2$  chamber for 5 minutes. This was a dry cleaning process and the samples did not require to be blown dry.

#### **3.3.4 Metalization.**

After cleaning, the samples were taken directly to either the Electron Beam Evaporator or sputtering chamber. The evaporator is shown in Figure 11. The evaporator had a 6.5 KW power supply and deposited metal at a rate of approximately  $2\text{-}3 \text{ \AA}/\text{s}$ . It operated at approximately 8 percent power for aluminum and 18 percent power for gold. A crucible held the target metal as shown in Figure 12. The chamber was held in a vacuum of approximately  $5\text{-}6 \times 10^{-6}$  Torr during metalization. Two vacuum



**Figure 11.** The electron beam evaporator was used for most metalizations to apply both front and back contacts on the samples. The picture shows the chamber, controls, and pumps.



**Figure 12.** A copper crucible held a cylindrical pellet of the contact metal. An electron beam evaporated the metal from inside the crucible.

pumps were used to adjust the pressure in the chamber to the appropriate level. This normally took 1 hour. A shutter was used to control metal deposition as shown in Figure 13. A quartz crystal was used to determine the rate at which metal was de-

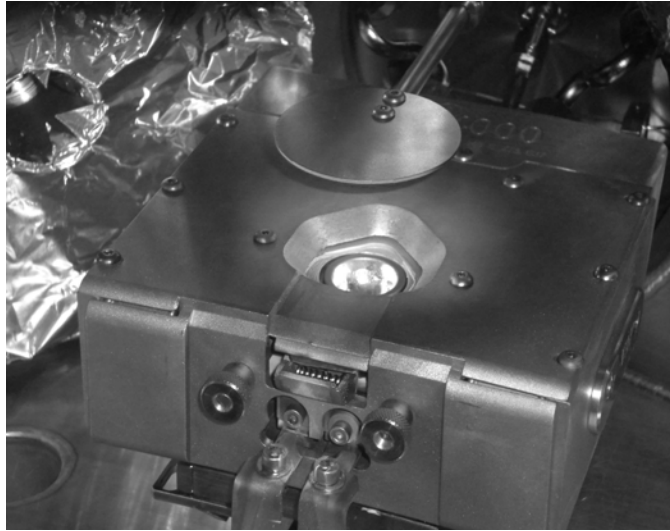


**Figure 13.** The shutter inside the electron beam chamber controlled the rate at which metal was evaporated onto the samples.

posited. A coil generated the electron beam to melt and evaporate the metal that was inside the crucible. It used a figure eight pattern to control the melting of the metal. Water was used to keep the copper hearth cool. A circular mounting apparatus that was used for metalization is shown in Figure 14. The front contacts were applied using a thin aluminum shadow mask with equally separated drilled out circular dots. The mask was placed in one of the open slots and the samples were affixed to the mask. The mounting apparatus was attached to the inside of the chamber as shown in Figure 15. During metalization, the mounting device rotated in order to give a uniform distribution of metal across the sample. Either 700 or 750  $\mu\text{m}$  diameter contacts were deposited on the PLD samples. The ALD samples had larger contacts with approximately a 1200  $\mu\text{m}$  diameter. The backside was covered with either aluminum or gold to between 500-800  $\text{\AA}$ .

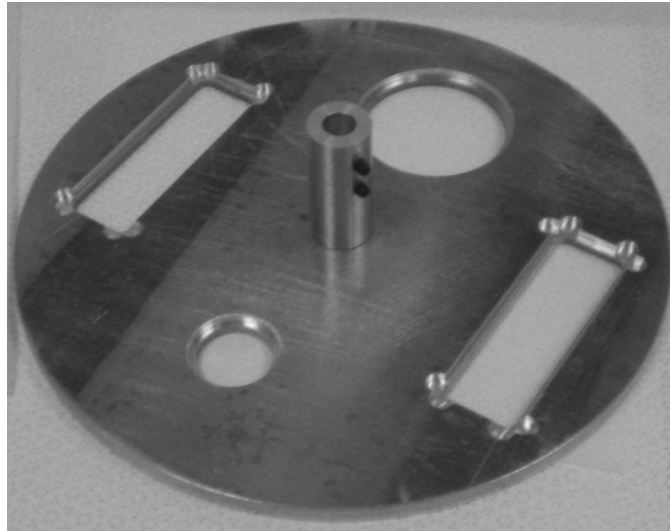


Figure 14. A circular chamber attachment was used for device mounting. A circular mask was placed in one of the slots and the samples were affixed on top of the mask.



Figure 15. The chamber attachment was affixed to a rotating metal dowel in the top part of the chamber. The attachment rotated inside the chamber to provide a uniform distribution of metal on the sample.



In order for wire bonding to work, it was found through trial and error that the total top metal contact thickness should be no less than 1000 Å. Nicollian and Brews [18] recommends a thickness no less than 3000 Å for wire bonding. A 750 Å aluminum contact allowed for bonding in this research, however the electrical characteristics were poor. The best recipe found was using a 200 Å seed layer of an active metal, titanium, followed by approximately 2800 Å of gold. Titanium provided good adhesion to the oxide and the gold-to-gold bonding allowed for a solid electrical connection between the wire and the top contact.

### 3.3.5 Annealing.

An annealing step was performed for several samples in an attempt to improve the electrical characteristics of previously tested PLD devices. The reason for performing this step was to reduce a high density of inherent electron or hole traps in the oxide and to create an ohmic contact by allowing for more adhesion between the back contact metal and the silicon substrate [18]. However, it was suggested early in the root cause investigation that a high trap density could severely affect device electrical characteristics [19]. Additionally, electrical characteristics could be distorted if an ohmic contact was not achieved by scratching or polishing the backside silicon surface. In order to ensure an ohmic contact was made with or without scratching, annealing was performed to adhere the metal contact to the silicon substrate. Several samples were annealed at 450°C for 30 seconds on a Surface Science Integration Rapid Thermal Annealer (RTA), shown in Figure 16. This temperature and time was assumed reasonable after a thorough literature search where similar Post Deposition Annealing (PDA) was performed with HfO<sub>2</sub> MOS capacitors [3, 20, 19, 21]. Unfortunately, the annealing did not improve the electrical characteristics of the PLD samples since pin-holes were discovered in the oxide material. This will be illustrated and discussed



**Figure 16.** Selected PLD samples were annealed by heating them to 450°C for 30 seconds. Samples sat loosely on a 3 inch diameter silicon wafer inside the chamber.

in the pre-characterization section of the Experimental Procedures chapter.

### **3.3.6 Packaging and Wire Bonding.**

Following metalization, the samples were packaged and wire bonded. They were packaged by using Epo-TEK H20E-HC conductive silver epoxy to adhere the sample inside the package enclosure. In order to allow the epoxy to cure, the packages were heated to 100°C for 1 hour in an Omegalux LMF-6525 oven. Following packaging, the samples were wire bonded with 0.0007” gold wire using a Kulicke and Soffa Model 4526 Analog Ultrasonic Compression Wedge Wire Bonder shown in Figure 17.

In order to wire bond, the package was first affixed to a package mount that an operator holds in place. The gold wire was thread through a needle point and the operator first attaches gold wire to a gold lead directly around the sample inside the package. The wire was then fed to a top metal contact approximately 2 mm away. Since the bonder utilizes an ultrasonic signal and compression to attach the wire, metal contacts that are too thin or of a different material than the wire sometimes will not allow for good adhesion. Also, if two metals are used on the sample, extra



**Figure 17. A Kulicke and Soffa Model 4526 Analog Ultrasonic Compression Wedge Wire Bonder was used to affix 0.0007" diameter wire to the top circular contacts of the samples.**

care needs to be taken to ensure compatibility. For example, even though gold wire could be attached to 750 Å aluminum does not mean that the gold wire would attach to a combination of 750 Å aluminum followed by 250 Å gold. This happened when one metal was softer than the other and the metal was not strong enough to withstand the compressive force of the wire bonder. If the wire did not attach to the top contact, silver paint was used in an attempt to attach the wire. This method was largely unsuccessful and when it was successful the electrical characteristics were poor. In addition to all the above, much success rested with the skill and experience of the wire bonder operator, specifically when it came to deciding how much compression was needed to ensure wire adhesion. A finished packaged and wire bonded device is shown in Figure 18. Top contact diameters were verified on a microscope. An example of this measurement of a full top contact for an ALD sample with wire attached to the center is shown in Figure 19.

A summary of all sample contact thicknesses is given in Table 2. A summary of how all samples were prepared is given in Table 3. Note that not all samples were

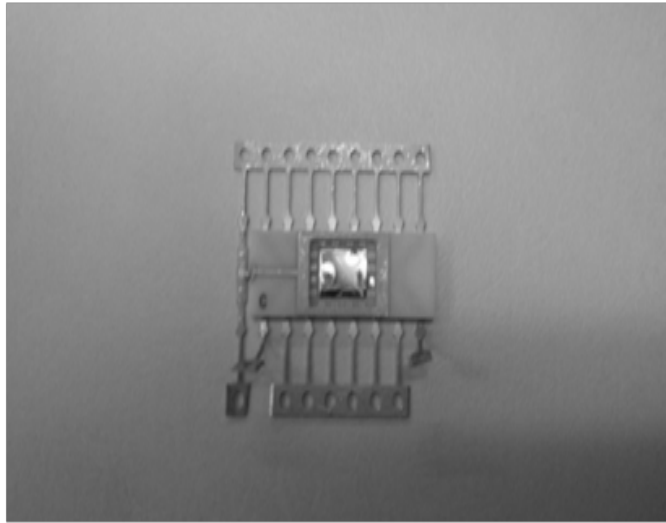


Figure 18. Samples adhered to the 16-pin dual in-line package by silver epoxy. Gold wires were attached from the inside leads surrounding the package to the top metal contact.

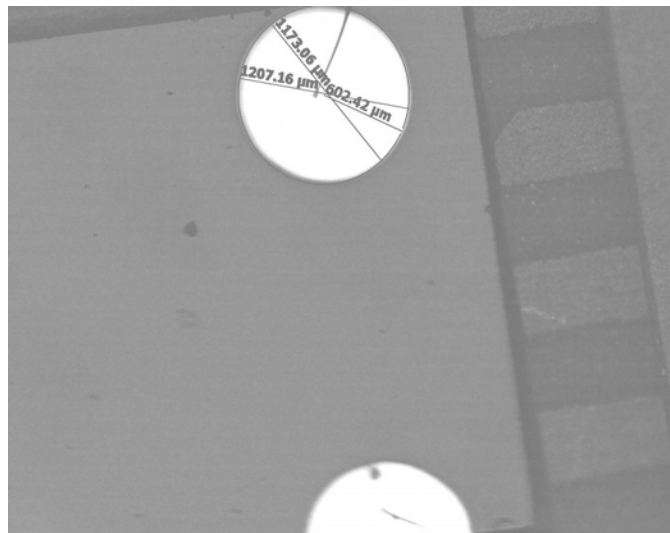


Figure 19. The ALD contact diameter was measured using a calibrated microscope. The image shows the diameter of a full contact to be approximately  $1200 \mu\text{m}$ . The image also illustrates half contacts as well as the package leads surrounding the sample.

used in irradiation experiments. Specifically, if samples were not wire bonded they were not used since the experiments were designed for in situ measurements. Those samples could have been used for ex situ measurements with the availability of a probe machine. Also, not all wire bonded samples resulted in good electrical measurements. This was due to the quality of the oxide as discussed earlier. Only the samples that had the best electrical characteristics were considered for use.

**Table 2. Metal Contact Summary**

ID	Deposition	Front	Thickness	Back	Thickness
1	750 Thick	Ti/Al/Au	100/500/1000	Au	820
2	750 Thick	Al	750	Al	750
3	300 Thick	Al	750	Al	750
4	300 Thick	Al	750	Al	750
5	750 Thick	Al	750	Al	750
6	750 Thin	Ti/Au	200/2800	Au	500
7	500 Thin	Ti/Au	200/2800	Au	500
8	750 Thin	Ti/Au	200/2800	Au	500
9	500 Thin	Ti/Au	200/2800	Au	500
10	300 Thick	Al/Au	750/250	Au	750
11	300 Thick	Al/Au	750/250	Au	750
12	500 Thin	Al/Au	750/250	Au	750
13	500 Thin	Al/Au	750/250	Au	750
14	500 Thick	Al/Au	750/250	Au	750
15	500 Thick	Al/Au	750/250	Au	750
16	750 Thin	Al/Au	750/250	Au	750
17	750 Thin	Al/Au	750/250	Au	750
18	750 Thick	Al/Au	750/250	Au	750
19	750 Thick	Al/Au	750/250	Au	750
20	ALD 50nm	Ti/Au	200/2800	Au	500
21	ALD 50nm	Ti/Au	200/2800	Au	500
22	ALD 50nm	Ti/Au	200/2800	Au	500
23	ALD 50nm	Ti/Au	200/2800	Au	500

**Table 3. Sample Preparation Summary**

ID	Deposition	Wire	Polish	Anneal	Cleaning	Metalization
1	750 Thick	Y	N	N	Ultrasonic	Evaporator
2	750 Thick	Y	Y	N	Ultrasonic	Evaporator
3	300 Thick	Y	Y	N	Ultrasonic	Evaporator
4	300 Thick	Y	Y	N	Ultrasonic	Evaporator
5	750 Thick	Y	Y	N	Ultrasonic	Evaporator
6	750 Thin	Y	N	N	O <sub>2</sub>	Sputtering
7	500 Thin	Y	N	N	O <sub>2</sub>	Sputtering
8	750 Thin	Y	N	N	O <sub>2</sub>	Sputtering
9	500 Thin	Y	N	N	O <sub>2</sub>	Sputtering
10	300 Thick	Y	Y	Y	Ultrasonic	Evaporator
11	300 Thick	N	Y	Y	Ultrasonic	Evaporator
12	500 Thin	N	Y	Y	Ultrasonic	Evaporator
13	500 Thin	N	Y	Y	Ultrasonic	Evaporator
14	500 Thick	N	Y	Y	Ultrasonic	Evaporator
15	500 Thick	N	Y	Y	Ultrasonic	Evaporator
16	750 Thin	N	Y	Y	Ultrasonic	Evaporator
17	750 Thin	N	Y	Y	Ultrasonic	Evaporator
18	750 Thick	N	Y	N	Ultrasonic	Evaporator
19	750 Thick	N	Y	N	Ultrasonic	Evaporator
20	ALD 50nm	Y	N	N	O <sub>2</sub> Chamber	Sputtering
21	ALD 50nm	Y	N	N	O <sub>2</sub> Chamber	Sputtering
22	ALD 50nm	Y	N	N	O <sub>2</sub> Chamber	Sputtering
23	ALD 50nm	Y	N	N	O <sub>2</sub> Chamber	Sputtering

## IV. Experimental Procedures

Since this work spanned three different types of irradiations, a review of how dosimetry was conducted is necessary for each type of irradiation. For all irradiations, total dose is given in rad(Si). Rad(Si) is an accepted dose reporting unit by the radiation effects community. In all cases, dosimetry was performed to determine the time necessary for each irradiation. Inherent error in determining total dose will also be discussed but will be summarized in later sections.

In addition to dosimetry, a few experimental details require explanation in order to understand both the results and analysis of this work. Since a large difference existed between the capacitance and current measurements of the PLD and ALD devices, pre-irradiation characteristics of each type of device are reviewed to understand why this difference existed. Lastly, a summary of all samples as well as the equipment used in all irradiations is provided to serve as a guide for the results and analysis chapters.

### 4.1 Gamma Irradiation Equipment and Dosimetry

The Gamma Irradiation Facility (GIF) houses an 11,000 gallon pool of water that contains a  $^{60}\text{Co}$  irradiator. The facility contains a 6" diameter 15' long, dry tube that sits inside a circular configuration of  $^{60}\text{Co}$  pins. The pins fit inside the empty rings outside the dry tube as shown in Figure 20. The dry tube is equipped with a lead shielded elevator. The lead shields contain grooves where cables can be fed in order to take in situ electrical measurements. This experimental configuration is shown in Figure 21. The loading elevator has a 4" diameter surface for placing experimental devices. The height of the surface is adjustable from the bottom of the tube since the usable dose profile falls off with increasing height as illustrated in Figure 22.

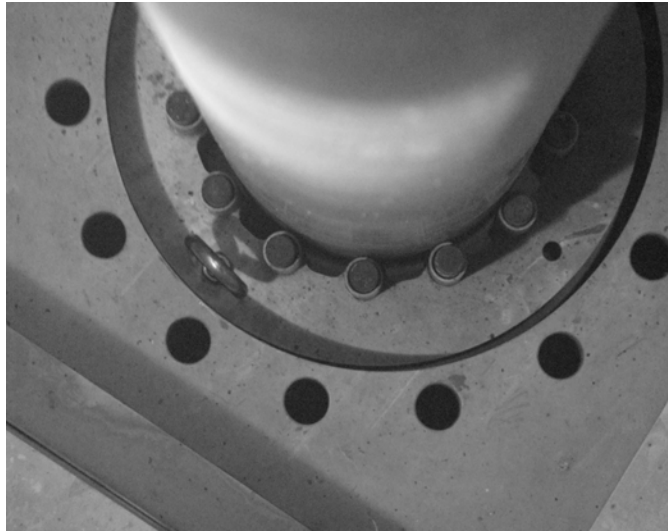


Figure 20. The GIF consisted of a <sup>60</sup>Co circular pin configuration surrounding the irradiation chamber. All this was submerged approximately 15' deep in an 11,000 gallon pool of water.

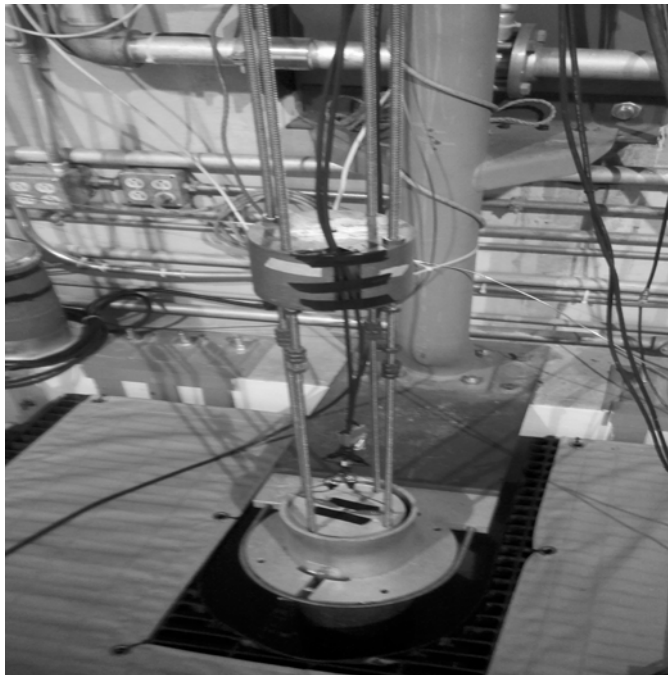


Figure 21. BNC cables were fed from measuring equipment to the outer leads of a device package located on a mounting station toward the bottom of the GIF elevator. The cables were fastened by electrical tape inside the grooves of the lead shields.



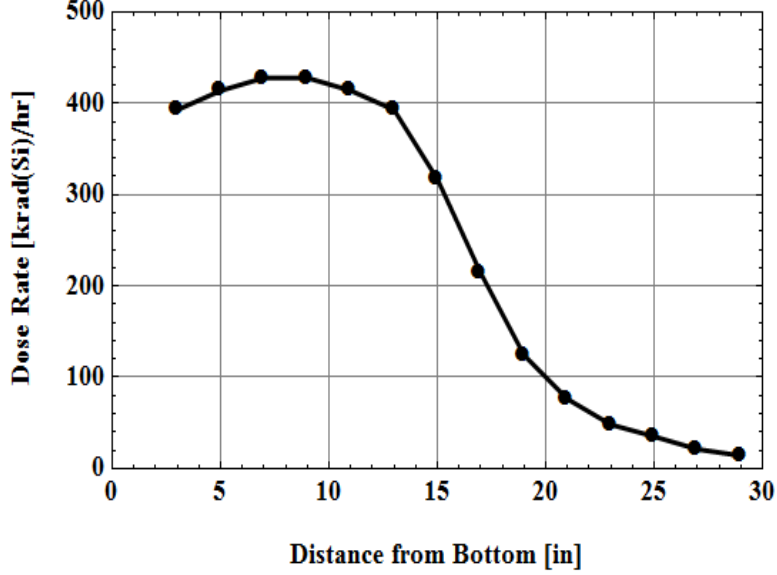


Figure 22. The gamma dose rate varies as function of distance from the bottom of the irradiation chamber. Accounting for the time since calibration and utilizing a factor of 7 difference between water and silicon mass attenuation coefficients, the dose rate was obtained in rad(Si).

The dose rate was measured by ceric cerous sulfate dosimeters, on 28 January 2002 to 200 krad(tissue)/hr at a distance of 9" from the bottom of the tube. Additional details on the use of ceric cerous dosimeters for gamma dose calibration can be found in the International Organization for Standardization and American Society for Testing and Materials (ASTM) standard 51205-09 [22]. On 20 October, 2010 the dose rate was 63 krad(tissue)/hr at the same distance. The total dose of gamma rays in rad(Si) was calculated by converting from dose in tissue to silicon. When the photon-induced dose in one material is known, a conversion to another material can be made by using a ratio of the mass energy absorption coefficients [23]. This is shown in Equation 2,

$$D_{Si} = D_{Tissue} \times \frac{\left(\frac{\mu_{en}}{\rho}\right)_{Si}}{\left(\frac{\mu_{en}}{\rho}\right)_{Tissue}}, \quad (2)$$

where  $D$  is the dose,  $\mu_{en}$  is the mass energy absorption coefficient, and  $\rho$  is the density of the respective material. The only condition necessary in using this equation is that of charged particle equilibrium (CPE). CPE exists when electron energy entering

a material equals the electron energy exiting. In photon dosimetry, the generated electrons deposit energy into a material, not the photons. If photons directly impact a material, the possibility exists that some electrons will escape the back end of the material. For the purposes of this work, CPE was assumed to exist for the original ceric cerous dosimetry experiment. This is assumed because the irradiation chamber material is 0.125" thick aluminum. Additionally, during irradiation, the ceric cerous is contained in a 600 mL beaker. All dose values given indicate exposure levels of the samples in rad(Si). If this dosimetry practice was followed correctly in 2002 according to [22], the estimate of the uncertainty of an absorbed dose should be less than 4%. Additional details of CPE and dosimetry for radiation hardness testing can be found in the 1992 Nuclear and Space Radiation Effects Conference short course notes [23].

The values of 0.723 and 0.105 were used as the mass energy absorption coefficients for silicon and soft tissue respectively. They were obtained from interpolation in the tables of values available from the National Institute of Standards and Technology website [24]. The expected dose in silicon is about 7 times higher than tissue. The calculated dose in rad(Si) is shown in Figure 22 as a function of distance from the bottom of the irradiation chamber.

## **4.2 Neutron Irradiation Equipment and Dosimetry**

The neutron irradiation experiment took place at Ohio State University Research Reactor (OSURR). The OSURR is a uranium reactor that can operate at a maximum of 500 KW. A 20-foot deep pool of water provides cooling, neutron moderation, and gamma shielding. A vertical irradiation chamber developed by Gray [25] was used for the experiment. The irradiation chamber consists of a 20.5' long, 7" outside diameter aluminum tube (6061 T6 aluminum) with 0.125" thick walls. The chamber was moved into contact with the reactor with the top of the chamber tube against

a bracket during each experiment. The chamber allowed access to the high neutron flux position adjacent to the reactor core while allowing access to the samples and mounting apparatus. The basic configuration is shown in Figure 23.

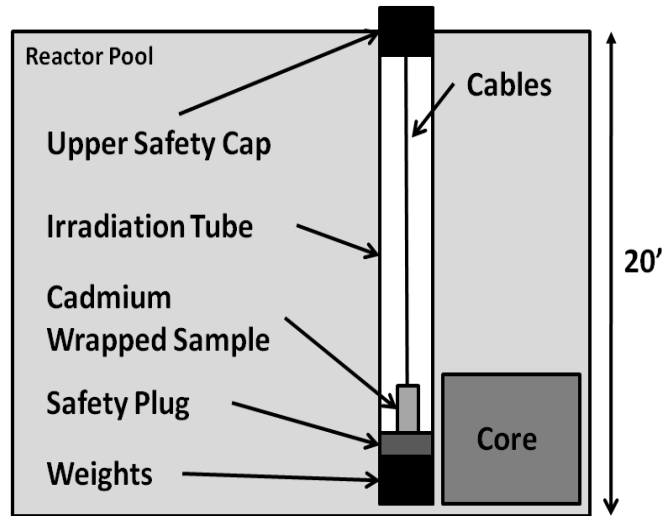


**Figure 23.** A 7" diameter irradiation tube was placed next to the reactor to utilize a high neutron flux from the reactor core. Safety plugs for streaming radiation were located in the top and bottom of the tube during reactor operation. Weights were located at the bottom of the tube to hold it in place.

The samples were mounted inside a small plastic bottle that was wrapped in 1 mm thick cadmium to reduce thermal neutrons that cause activation. Ignoring resonance absorption lines, Cd has nearly a 4 order of magnitude increase in neutron absorption cross section below neutron energy of 0.2 eV. Neutrons of energy greater than 1.5 eV pass through Cd with little attenuation ignoring resonance absorption. Although activation is reduced with Cd, fission gamma rays are a significant source of additional accumulated dose. Because a high 1-MeV (eq) neutron dose was required for this investigation, no further shielding was pursued in an effort not to further reduce this dose. Electrical attachments were made through the use of alligator clips that were connected to BNC cables. The plastic bottle was taped to the side of a plastic rod that was attached to a 7" diameter foundation. The location of the bottle

was approximately 12" from the bottom of the tube.

Dosimetry was performed, with great assistance from the OSURR staff, by measuring both the total neutron flux and the neutron energy spectrum. The flux profile in the irradiation chamber was measured by irradiating a long copper wire held vertically 25" from the bottom of the chamber and measuring the activity of segments of the wire at 1" intervals. A distance of 12" from the bottom of the tube was selected in order to maximize the neutron flux. All irradiations were made with the samples at this position. The flux profile is given in Figure 24.

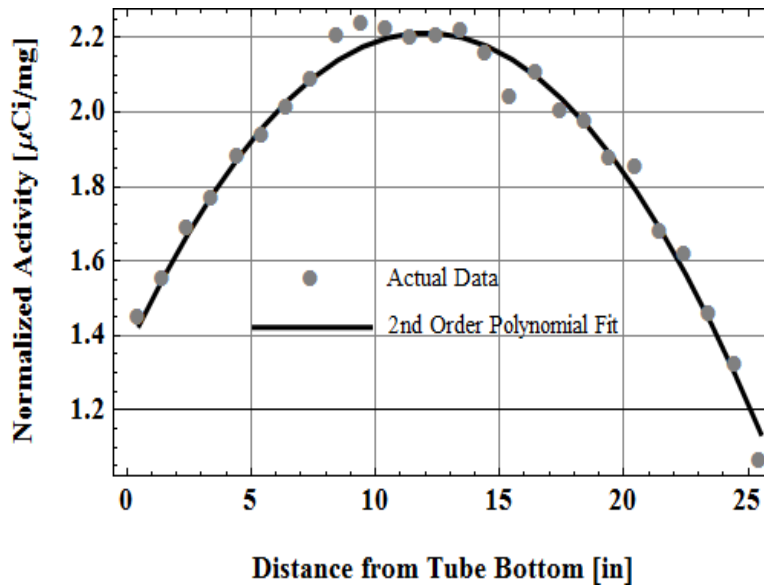
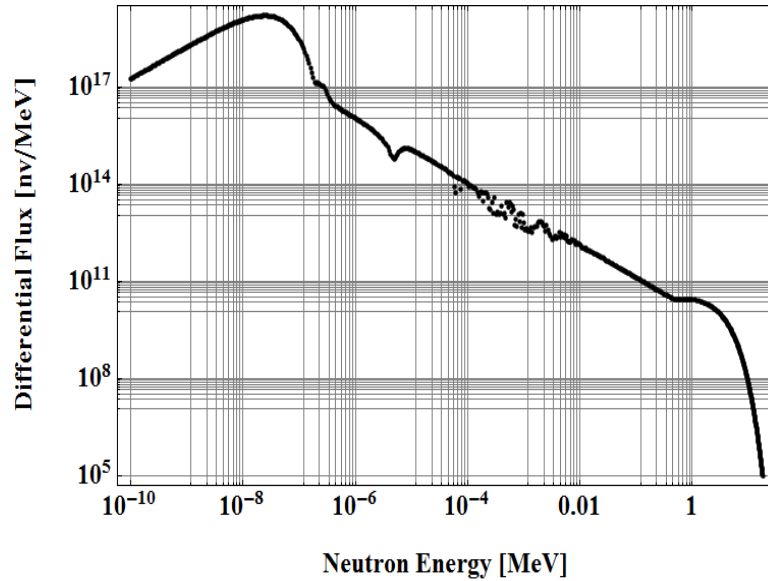


Figure 24. A neutron profile was obtained from activation analysis of small metal wires. This profile provides optimum placement of devices at approximately 12 inches from the bottom of the irradiation tube. The highest neutron flux was desired in order to cause the maximum amount of displacement damage.

The neutron energy spectrum was measured by activation analysis. Gold, copper, and cobalt wires were irradiated at a position 12" from the bottom of the tube. One wire set was bare and the other two were enclosed in cadmium. The reactor was operated for 30 minutes at 100 KW. The wires were removed and their activities were counted using a high purity germanium gamma detector. The spectrum was unfolded

by OSURR staff using the SNL-SAND II program. Additional details for unfolding procedures can be found in the SAND II users manual [26]. The resulting neutron spectrum is shown in Figure 25.



**Figure 25.** A neutron energy spectrum was collected through activation analysis for a location 12” from the bottom of the irradiation tube. This information was necessary in order to calculate the 1-MeV (eq) neutron fluence.

At 450 KW power, a neutron flux of  $6.87 \times 10^{10}$  n/cm<sup>2</sup>·s of 0.5 MeV and greater neutrons was measured. Neutron flux is linearly proportional to reactor power [27]. Because of uncertainty in the measurement of the energy spectrum, the fluence has an error of greater than 25% [28]. The fluence used in this experiment, based on times of irradiation and reactor power, is shown in the irradiation section of the experimental procedures chapter.

In order to determine the displacement damage effectiveness of neutrons, the OSURR neutron energy spectrum is reduced to a mono-energetic source with a damage effectiveness equivalent to the full energy spectrum. The 1-MeV equivalent or 1-MeV (eq) neutron fluence for silicon is reported for purposes of radiation testing of electronic devices. The method for performing this procedure is outlined in the ASTM

standard E722(2002) [29]. Using Equation 3 from [29], 1-MeV (eq) neutron dose can be determined. 1-MeV (eq) is the fluence required of 1 MeV mono-energetic neutrons to cause the same amount of damage as the entire neutron spectrum for a given material. In this case, the given material is silicon and the ASTM standard provides the necessary damage functions.

$$\phi_{EQ,1MeV,MAT} = \frac{\int_0^{20MeV} \phi(E) F_{D,MAT}(E) dE}{F_{D,1MeV,MAT}} \quad (3)$$

For Equation 3,  $\phi(E)$  is the incident neutron energy fluence spectral distribution,  $F_{D,MAT}$  is the neutron displacement damage function for the irradiated material (displacement damage per unit fluence) as a function of energy, and  $F_{D,Eref,MAT}$  is the displacement damage reference value designated for the irradiated material and for the specified equivalent energy,  $E_{ref}$ , as given in the ASTM standard. In order to obtain the 1-MeV (eq) dose, the 1-MeV (eq) fluence value was multiplied by a fluence-to-dose conversion factor. Holmes-Siedle [8] presents a plot of this factor as function of energy. The fluence-to-dose was taken to be approximately  $3 \times 10^{-11}$  [rad(Si)cm<sup>2</sup>] based on a 1-MeV (eq) neutron fluence.

### 4.3 Ion Irradiation Equipment and Dosimetry

This work involved two different ion irradiations, both performed at the Ion Beam Laboratory (IBL) located at Sandia National Laboratory (SNL). First, 2-MeV helium ions in the +2 charge state were used to perform Rutherford Backscattering (RBS) experiments in order to determine the stoichiometry and thickness of the HfO<sub>2</sub>. Dosimetry was not needed for this case because the objective was to obtain counts as a function of backscattered energy. Second, 1-MeV silicon ions in the +1 charge state were used to study the NIEL effects in HfO<sub>2</sub> samples. Silicon was used in order not to cause adverse effects in the silicon substrate. Different ions might cause interstitials

that would change electrical properties of the substrate. Dosimetry is important for this silicon case because the objective was to determine how the capacitance changed as a function of fluence and dose.

For both types of ion irradiations, a high voltage Tandem accelerator was used to accelerate ions to the desired energy. The Tandem is a two stage system that harnesses both attractive and repulsive coulombic forces. A positive terminal is located in the center of the accelerator shown in Figure 26. Negatively charged ions are fed into

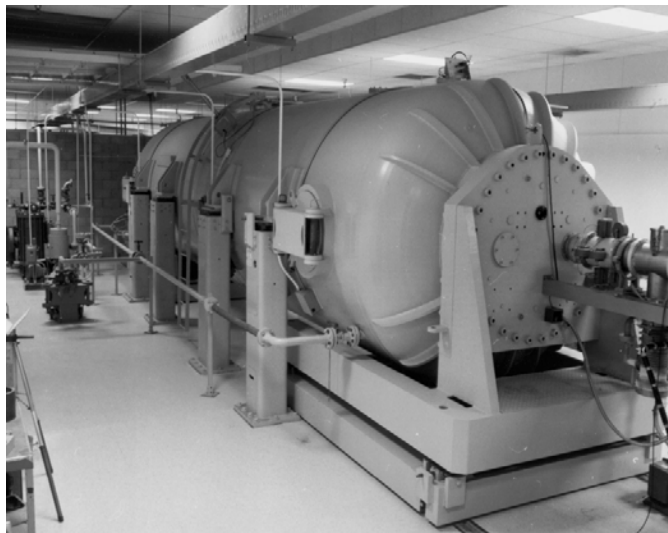


**Figure 26. The Tandem accelerator was used to generate and separate out the necessary ions and energies for all irradiations.**

the Tandem and they are attracted toward the positive terminal. As the ions pass through the positive terminal, electrons are stripped off creating positively charged ions. These ions are repulsed from the positive terminal accelerating the ions even further. Since the Tandem was used to accelerate ions for multiple end-stations, magnets are used to bend the accelerated ions to the appropriate beam line.

The RBS experiment was performed on the Ion Beam Analysis (IBA) beam line. The IBA is shown in Figure 27. 8 bare samples smaller than the size of a thumbnail could be placed inside the mounting device at one time. It contained adjustments

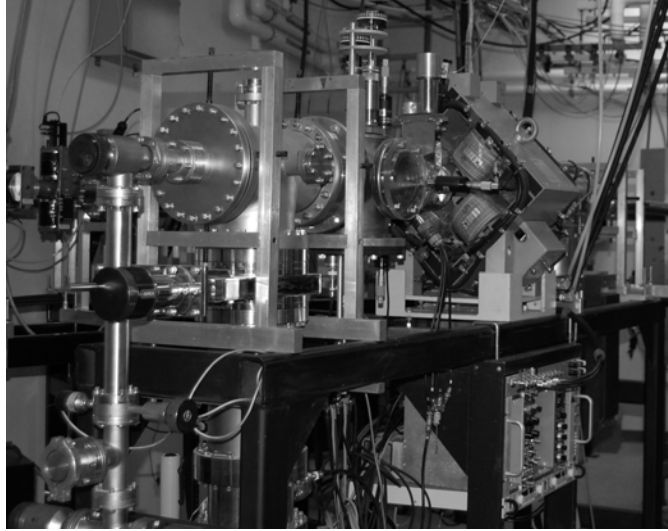


**Figure 27.** The Ion Beam Analysis beam line was utilized for Rutherford Backscattering experiments with 2-MeV helium (+2) ions.

whereby the sample and angle to the beam could be changed. This device is shown in Figure 28 and at the top of the IBA irradiation chamber in Figure 27. Further experimental details and results will be discussed in the Rutherford Backscattering Results section of the Experimental Results chapter.

The 1-MeV silicon ion irradiations were performed on the Qualification Alternatives to the Sandia Pulsed Reactor (QASPR) III beam line. The QASPR III irradiation chamber is shown in Figure 29. The samples were adhered to a horizontal mount on the inside door of the irradiation chamber as shown in Figure 30. Cables with alligator clips were fed to the sample to make electrical connections inside the chamber. Bayonet Neill-Concelman (BNC) connections were available outside the chamber so in situ measurements could be made. The BNC cables were attached to a Boonton 7200 Capacitance Meter. A Keithley 2400 Voltage Source Meter was connected to source voltage so capacitance measurements could be taken. This setup is illustrated in Figure 31.



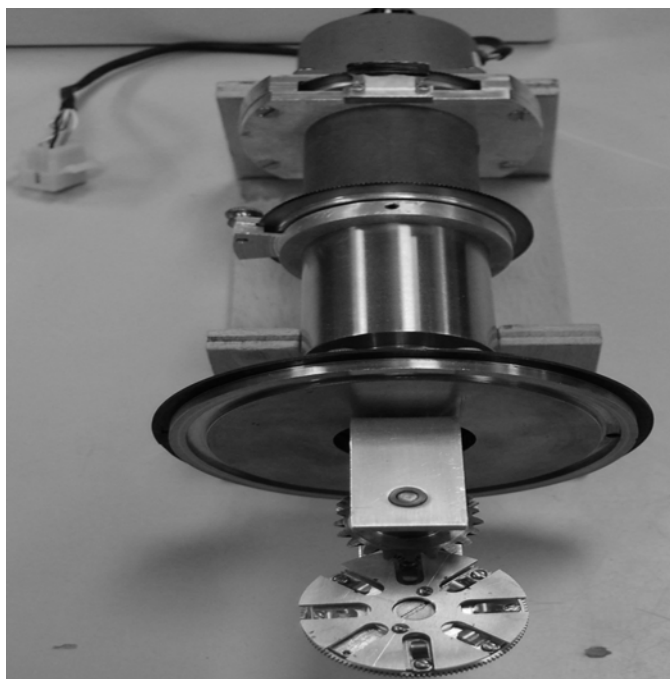


Figure 28. The Rutherford Backscattering sample mount could accommodate 8 samples at a time. The angle to beam could also be adjusted through controls located at the top end of the mount.

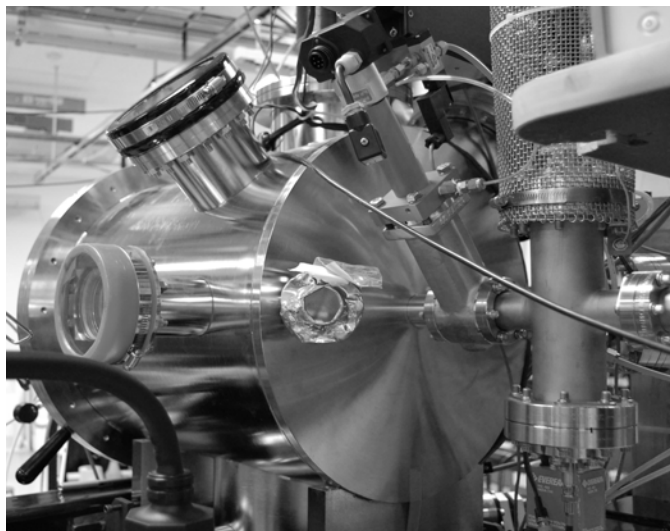


Figure 29. The QASPR III beam line irradiation chamber was approximately 2' in diameter and 3' deep. A small window allowed viewing of the device on the mount. Cryogenic pumps were used to the achieve a pressure of approximately  $10^{-6}$  Torr.

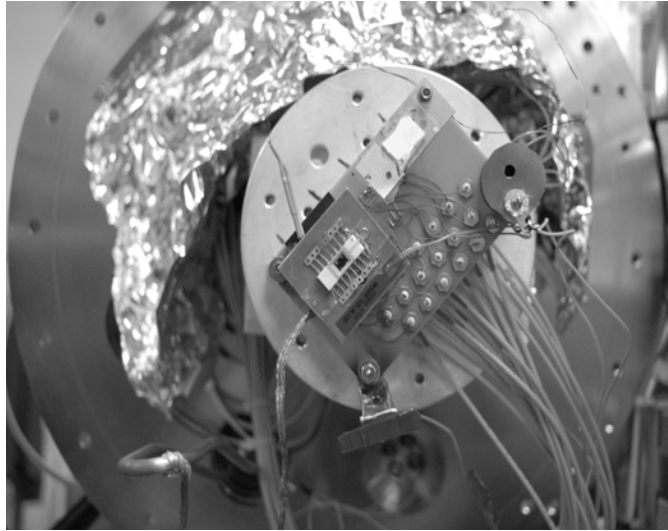


Figure 30. The QASPR III device mount inside the irradiation chamber consisted of a rectangular vertical strip of copper. The device was mounted with double sided scotch tape. BNC cables were fed inside the chamber to the outer leads of the device. Beam area calibration utilized a paper mesh grid and a phosphorous strip located above the device.



Figure 31. The measurement setup utilized a laptop, CV meter, and a voltage source. Cables were fed from the CV meter to the outside of the irradiation chamber. The QASPR III controls were many and elaborate, however in house Labview programs controlled the beam and an oscilloscope verified the current in the beam line.

The equation that determined dose in rad(Si) from [30] is Equation 4,

$$Dose = \frac{Constant \times \left(\frac{dE}{dx}\right)_{elec} \times \phi}{\rho_{Si}}, \quad (4)$$

where the constant is  $1.6 \times 10^{-6}$ ,  $\left(\frac{dE}{dx}\right)_{elec}$  is the ionization or electrical energy loss calculated by the Stopping Range of Ions in Matter (SRIM) simulation program [31],  $\phi$  is the fluence of the ion beam, and  $\rho$  is the density of silicon ( $2.32 \text{ g/cm}^3$ ). The constant is a conversion factor since SRIM gives the electrical energy loss in  $[\text{eV}/\text{\AA}]$ . The electrical energy loss from silicon ions as a function of depth in the samples is shown in Figure 32. The gray lines indicate separation between material in the device stack. From left to right the material is as follows: 2800  $\text{\AA}$  gold, 200  $\text{\AA}$  titanium, 500  $\text{\AA}$  oxide, 10,000  $\text{\AA}$  silicon substrate. A value of  $90 \pm 10 [\text{eV}/\text{\AA}]$  was used for all dose calculations.

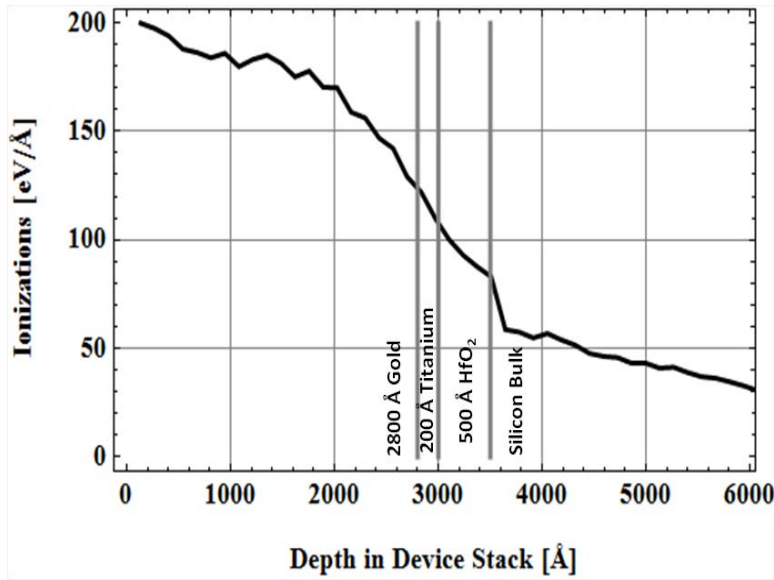


Figure 32. Dose calculations required an estimate of the electrical energy loss of silicon through the oxide. Ionization from bombarding silicon ions was simulated in SRIM. The electrical energy loss was approximated at 90 (eV/angstrom) in the oxide. The gray lines give separation to the device stack. From left to right: 2800  $\text{\AA}$  gold, 200 $\text{\AA}$  titanium, 500  $\text{\AA}$  oxide, 10,000  $\text{\AA}$  silicon substrate.

There are two sources of error in Equation 4. First, there is a small error in the accuracy of SRIM to calculate the electrical energy loss. This error can be larger if the energy loss is not constant across the thickness of the material in question. The second source of error is in the fluence. When the beam current is stable, as was the case in most irradiations, an in-house IBL Labview program was used to determine fluence stability. When the beam is not stable, fluence error arises from uncertainty in beam current and area. Ion fluence, from first principles, is calculated by Equation 5,

$$\phi_{ion} = \frac{I_{beam} \times t_{pulse}}{q \times A_{beam}}, \quad (5)$$

where  $I_{beam}$  is the beam current in amps,  $t_{pulse}$  is the pulse of the beam in seconds,  $q$  is the charge of an electron ( $1.6 \times 10^{-19}$ ) in coulombs, and  $A_{beam}$  is the area of the beam in  $\text{cm}^2$ . The beam current was approximated by measuring the current with a 100 ms pulse on a Tektronix DPO 7104 Oscilloscope into a Faraday Cup both before and after the actual beam shot on the sample. The beam area was found and adjusted in two steps. First, a high speed camera was calibrated to the location of the beam. The camera was located inside the irradiation chamber. The beam was located by applying beam pulses to a paper grid. The ions impacting the paper grid changed color as illustrated by the dark area inside the grid lines in Figure 33. Second, a phosphorous grid was used to illuminate and capture an image of the beam as illustrated by the white areas in Figure 34.

A Labview program written by an IBL staff member [30], takes the phosphorous illuminated image and calculates the area and the associated uncertainty. The area of the beam for the ion irradiations was adjusted to approximately fit the circular area of the electrical contacts, approximately  $0.0057 \text{ cm}^2$ , on the samples. It was important for the top contact to approximately encompass the beam area in order to ensure the dosimetry was correct. The size of the beam was adjustable through the

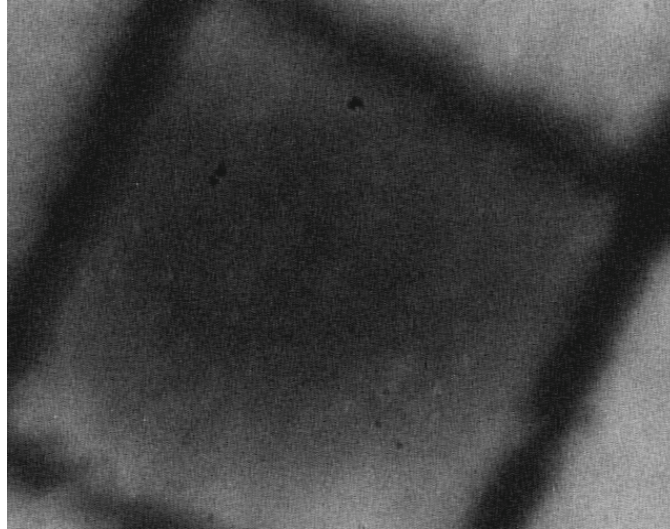


Figure 33. A paper grid was used to identify the beam and calibrate a chamber camera to the beam location in order to center the ion shots over the top contacts of the device. Live images from the camera to a TV screen helped witness gradual discoloration in the white areas of the grid during multiple pulsed shots. Each grid was approximately 1 mm<sup>2</sup>.

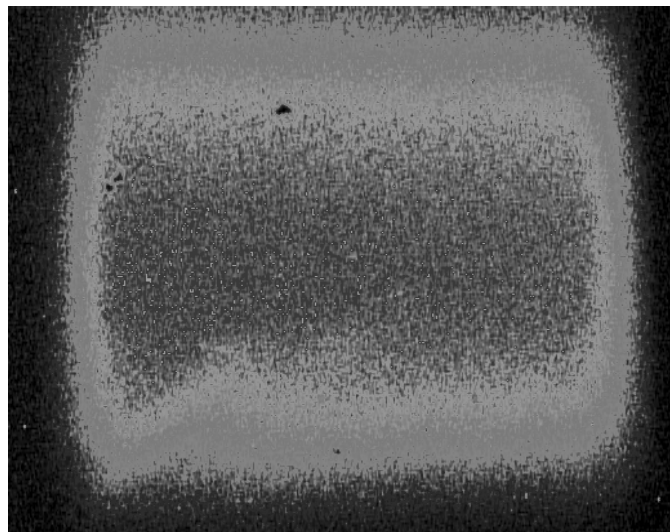


Figure 34. A phosphorous strip was used to illuminate the size and shape of the beam. The captured image from the camera was sent to a Labview program that calculated the area and associated uncertainty based on beam intensity. Beam intensity was identified through different colors of the image. Since this image was made black and white, larger intensity was located toward the center of the image.

use of slits in the piping of the beam line located several feet in front of the irradiation chamber. Thus, the uncertainty in the fluence value rests with the beam area and current. The beam was stable during the ALD irradiations where the IBL Labview program calculated this uncertainty.

#### 4.4 Data Collection

CV measurements were obtained in situ for all irradiated samples. A shift in the voltage at which the capacitance changes indicates an addition or loss of oxide traps. If the transition region slope changed, this indicated that interface traps were formed on the semiconductor side of the interface. Depending on amount of shifting as well as which direction these shifts occur provides insight into both electron and hole trap formation and movement in the oxide as discussed in Chapter 2. These insights provide valuable information as to how traps are formed and what can be done in the oxide to reduce trap formation.

All measurement equipment consisted of RG58 BNC connections from measurement equipment to device under test. All CV measurements were taken on a Keithley 4200 [32], Keithley 590, or Boonton 7200 capacitance meter. Only the Keithley 590 and the Boonton 7200 were used for the ALD irradiations. The Keithley 590 had a capacitance accuracy within 6% and was greatly reduced with decreasing capacitance. It was high due to the high conductance, approximately 7 mS, which is used to compute the accuracy of the measurement [33]. The voltage bias display had an accuracy of 0.05%. The Boonton 7200 had a capacitance accuracy within 1% and an external bias accuracy within 0.25% [34]. An example of pre-irradiation CV plots with associated error bars for the ALD gamma and ion irradiations is shown in Figure 35. The Keithley 590 was used for the gamma irradiation and plateaus at approximately 2 nF. The Boonton 7200 was used for the ion irradiation and plateaus at approxi-

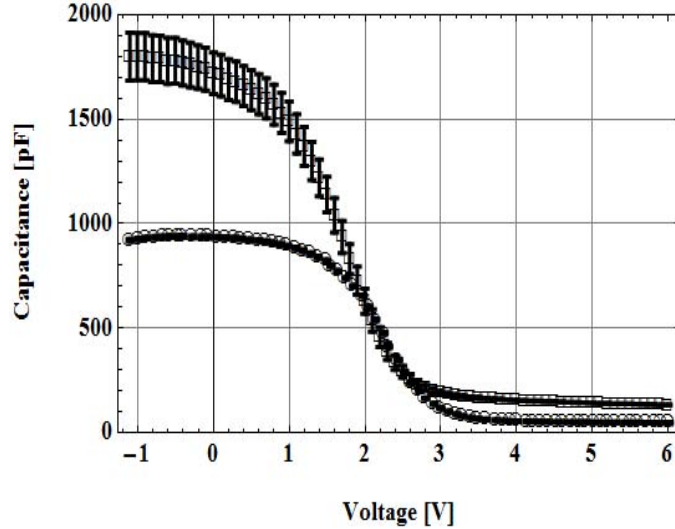


Figure 35. These pre-irradiation plots illustrate an example of measurement device accuracy for both an ion and gamma irradiation. The gamma irradiation plateaus out at approximately 2 nF and the ion irradiation plateaus at approximately 1 nF. Measurement error was due to the CV meter manufacturer’s stated level of accuracy. Error was minimized because all ALD measurements were taken in situ with nothing changing except for the effects that were occurring in the irradiated device.

matley 1 nF. Capacitance accuracy for all irradiations was limited to manufacturer’s stated error in the users manual because all measurements were taken in situ. That means instruments were not turned off, cables were not changed or adjusted, irradiation chamber pressure remained constant, etc. The only non-measurement error would be in dose or fluence as was discussed previously.

In the case of the Boonton 7200, a Keithley 2400 was used to source voltage. The 7200 could source it’s own voltage, however, the 2400 was used in order to simplify and reduce the number of steps necessary to have an operating Labview program. This was a time saving decision in order to maximize ion beam time.

The Keithley 4200 operated similarly to both the Keithley 590 and Boonton 7200 except that it plotted data immediately as it was taken. Multiple voltage sweeps programmed for specific time intervals were utilized that obtained CV and conductance versus voltage (GV) data. Constants and equations could be entered manually before measurement so calculation of device parameters could readily be obtained.

Additionally, all data from a full experiment was obtained automatically without requiring multiple data saving steps. When the 590 and 7200 was used, they were connected to a laptop with Labview through either a Universal Serial Bus or General Purpose Interface Bus connection that controlled voltage sweeps. In this case, each voltage sweep was automatic but had to be executed at each time interval or after each ion shot. The Boonton 7200 contained a range and reading rate disadvantage. It had the same capacitance range as the Keithley 590 at 2 nF, but was limited to 2 mS for conductance measurements as opposed to 20 mS for the Keithley 590 at 1 MHz. This limitation rendered conductance measurements useless for the final ion irradiations by cutting off measurements above 2 mS. This was unavoidable due to equipment unavailability. The reading rate was limited by the Labview code used to control both the Keithley 2400 and Boonton 7200. This code was originally used to obtain IV data from the Keithley 2400, but was modified to control and obtain CV data from the Boonton 7200. Time was not available to optimize the reading rate of this code, nor build a new code entirely before scheduled irradiations. The reason for utilizing different measurement devices in all irradiations were sample availability, irradiation facility schedule, or inoperability/unavailability of CV meters.

In all cases, except for the two PLD gamma irradiations, cable compensation and cable correction were performed in order to account for added capacitance due to cable length. This was not performed for the two PLD gamma irradiations due to the unfamiliarity with how to compensate for cables on the Keithley 4200. This was corrected for all subsequent irradiations. Table 4 gives a summary of all the experiments and what data gathering equipment was used. The table is organized by the order in which the irradiations occurred. The sample ID can be traced back to Tables 2 and 3, which give the details of how the device was fabricated. Note that Table 4 does not show the RBS irradiations. Count number as a function of energy was



desired in the RBS irradiations to extract stoichiometry of the sample and thickness of oxides in the devices. The stoichiometry gave quantitative insight into possible contamination of the oxide that would affect electrical measurements. Bare samples with no metal contacts were used for these experiments. This experiment, including data collection equipment will be discussed in the results chapter.

**Table 4. Data Gathering Equipment Summary**

Sample ID	Sample Type	Irradiation Type	Equipment
4	PLD	Gamma (0V)	4200
3	PLD	Gamma (5V)	4200
2	PLD	Neutron (0V)	4200
1	PLD	Neutron (5V)	4200
6	PLD	Ion (0V)	590 and 2400
20	ALD	Gamma (0V)	590
21	ALD	Gamma (5V)	590
22	ALD	Ion (0V)	7200 and 2400
22	ALD	Ion (0V)	7200 and 2400

Current versus voltage (IV) measurements were used in pre-characterization of all devices. They served as an important diagnostic tool to understand how well the oxide performed as an insulator. More IV data was desired in this work however was not taken for several reasons. The IV characteristics of the PLD devices did not warrant taking IV data during irradiation as will be illustrated in the next section. IV data was not taken for the ALD gamma irradiations due to complications using the 4200. The IV measurements did not seem to be correct due to either bad cabling or software offsets. Measurements were attempted on a Keithley 237, however these devices exceeded the limitations of the 237 by having extremely low currents. Time and beam availability were not available to troubleshoot the Keithley 4200 or develop an alternative.

## 4.5 Pre-Characterization

This section is presented to illustrate differences between pre-irradiated PLD and ALD devices. Electrical measurements of PLD devices were difficult to interpret and proved uncharacteristic in comparison to literature with similar  $\text{HfO}_2$  MOSCAPs [4]. A thorough literature review revealed that ALD was the preferred method for  $\text{HfO}_2$  deposition. No published research indicated the use of PLD for  $\text{HfO}_2$  deposition. Characteristics in CV and IV plots drove decisions to vary steps in the device preparation process in an attempt to improve electrical characteristics. Several examples of pre-irradiated CV plots for different PLD devices are illustrated in Figures 36-40. Non-linearity was the most notable feature of Figure 36 followed by a decreasing capacitance in the accumulation region. Figure 37 also illustrated non-linearity followed

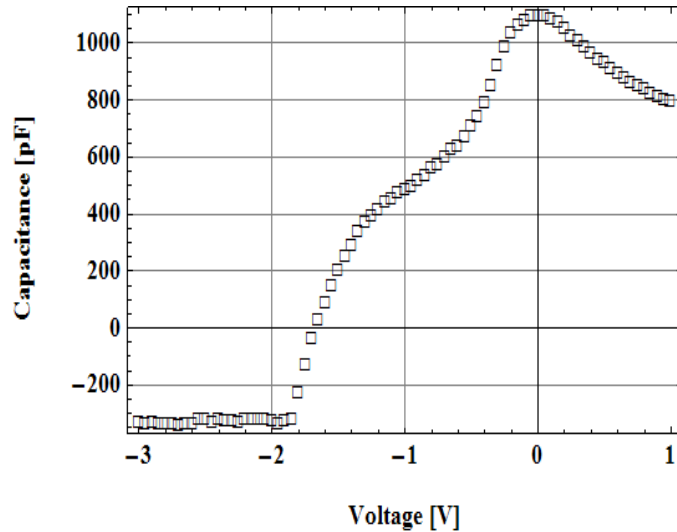


**Figure 36.** The pre-characterization CV curve for a  $300^\circ\text{C}$  thick PLD device (sample #4) used for 0 V bias gamma irradiation illustrated uncharacteristic behavior. The most notable feature is the non-linear slope in the depletion region followed by a decreasing slope in the accumulation region. Negative capacitance was due to not correctly compensating longer cables used in the experiment.

by decreasing capacitance past 0 V. Figure 38 revealed better slope characteristics than Figures 36 and 37. However the capacitance range is limited by 10 pF. A deca-

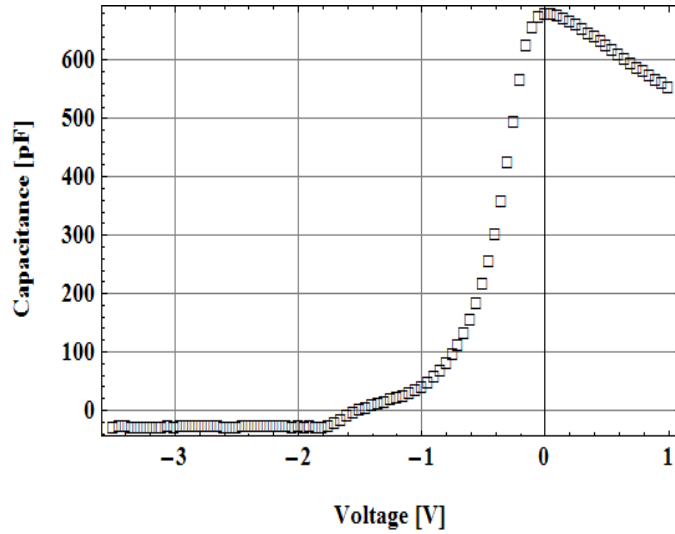


**Figure 37.** The pre-characterization CV plot for a 300°C thick PLD device (sample #3) used for the 5 V bias gamma irradiation also illustrated uncharacteristic behavior. It also featured an uncharacteristic slope in the depletion region of the plot. Negative capacitance values resulted from not correctly compensating for longer cables used in the experiment.

ing capacitance past 0 V seems to be a common characteristic of all PLD samples. Figure 39 is also limited in range and the slope appears more concave. Figure 40 has a large range, however the capacitance is again decreasing rapidly past 0 V.

The five pre-irradiated CV plots represent a cross section of all the PLD devices. A few notable observations were made from these plots. First, capacitance range widely varied between all devices. A couple of plots had a 800 pF range, while others had a 10 pF or smaller range. This calls into question the thickness of the oxide layer between devices because different oxide thicknesses give different capacitance values and ranges. Second, all curves had different slopes. This indicated a varying amount of traps. Third, the accumulation region capacitance drops with lower voltage, which is not expected. This gives indication of leaking charge or an added oxide layer that would decrease capacitance with increasing voltage. Cleaning, polishing, and annealing were attempted to alleviate these characteristics in the samples. Subsequent CV measurements indicate the same results.

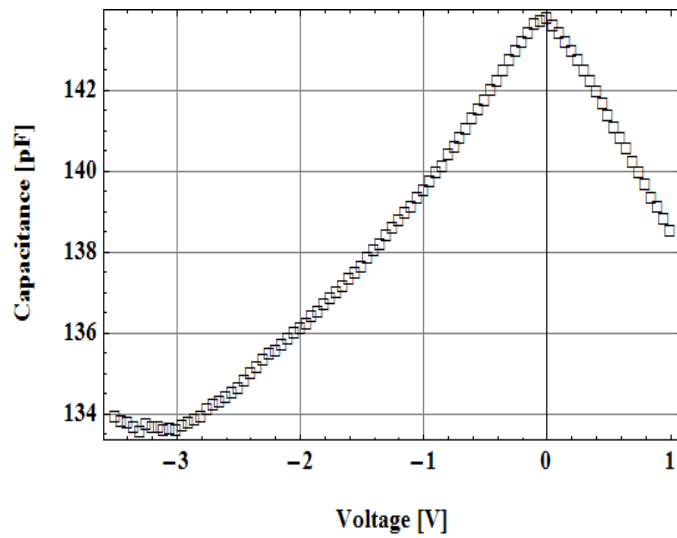


Figure 38. The pre-characterization CV plot for a 750°C thick PLD device (#2) used for the 0 V bias neutron irradiation suffered from a long gradual slope over a very narrow capacitance range of approximately 10 pF.

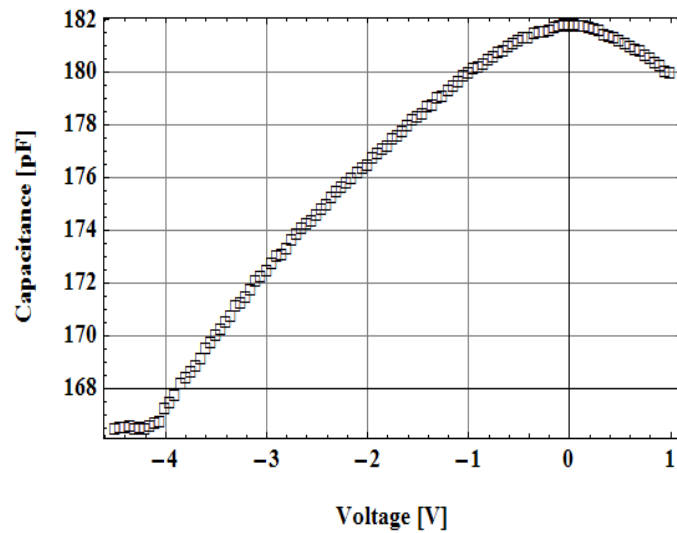
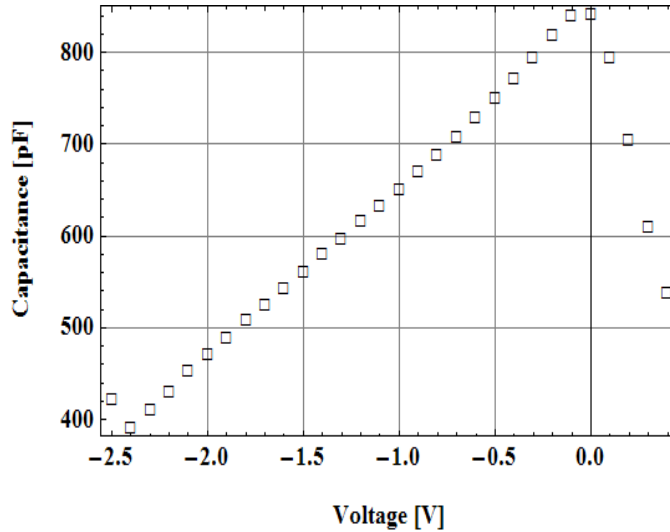


Figure 39. The pre-characterization CV plot for a 750°C thick PLD device (#1) used for the 5 V bias neutron irradiation also suffered from a long gradual slope over approximately 15 pF.



**Figure 40.** The pre-characterization CV plot for a 750°C thin PLD device (#6) used for the ion irradiation gave a very linear gradual slope over approximately 400 pF. The accumulated capacitance seemed to drop off very quickly after 0 V.

Since thickness of the PLD oxide was not known, an attempt was made to determine the thickness so that the capacitance could be calculated and compare with measured values. Four samples, 300°C and 500°C thick and thin, were measured on a Tencor needle point system. Values between 300°C and 500°C thin, and between 300°C and 500°C thick ranged by approximately 50 nm in spite of multiple measurement attempts. This inconsistency calls into question the thickness uniformity of the deposited oxide layer between samples. Pictures were taken of the samples in order to illustrate where thickness measurements were attempted as shown in Figure 41. This figure indicates pin holes in the oxide were created by PLD. The white in the figure is the silicon substrate. This potentially explains why the devices did not function as capacitors. However, IV plots indicated how well the insulator was working. IV plots are shown for a cross section of all PLD devices in Figure 42. Since mA's of current was traversing the devices over a 6 V range, pin holes covered by metal contacts provides a plausible explanation for the poor characteristics of the PLD devices.

The ALD samples, in contrast, demonstrated far superior capacitance character-

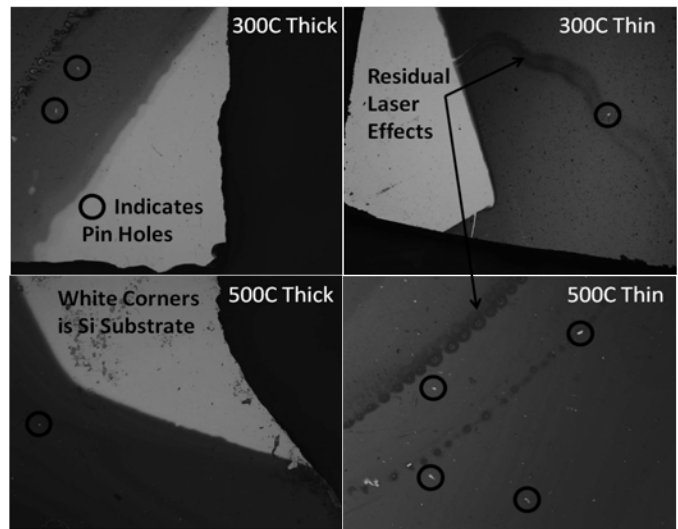


Figure 41. Images of four different PLD samples illustrate residual laser marks as well as pin holes in the oxide. White areas on corners are silicon substrate. White holes can be seen through the oxide. Metal contacts fit over these holes whereby electrical paths could be formed.

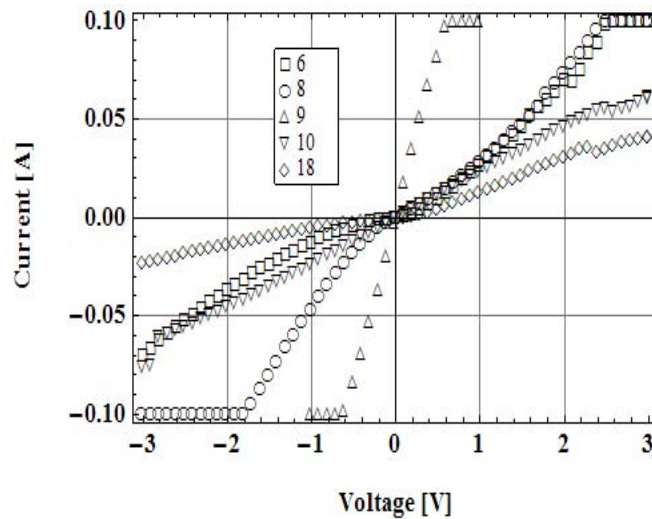
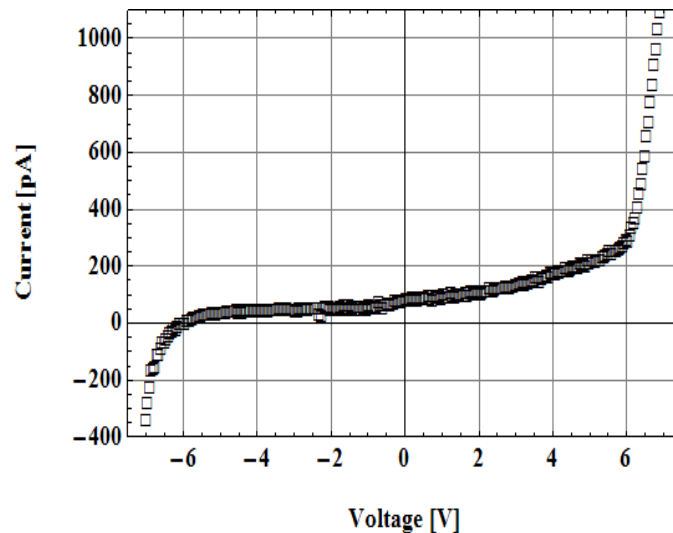


Figure 42. A cross section of all PLD device pre-characterization IV data was plotted. All PLD pre-characterization IV plots showed current in the mA range over a short voltage range.

istics than the PLD samples. This was clearly observed in both IV and CV plots for samples 20-23. An example of an ALD IV measurement for sample 20 is shown in Figure 43. This plot was very similar to all samples where current variation was less than 100s of pA over a large voltage range. The CV characteristics of all the



**Figure 43.** All ALD pre-characterization IV plots illustrate leakage current in the 100s of pA over a -7 to 7 V range.

ALD irradiated samples is shown in Figure 44. Notice that all plots are in the same capacitance range which suggests more uniform deposition of the oxide layer. The difference in accumulated capacitance values is the difference in area of the contacts used during irradiations and was anticipated.

In-spite of the outstanding CV characteristics demonstrated in the ALD samples, the dielectric constant needed to be verified for  $\text{HfO}_2$ . Verification was performed through the parallel plate capacitor equation, where  $C_{OX}$  was taken from the measured accumulated capacitance of the pre characterization curves of Figure 44. Thickness was also known and verified through experiments (see section 5.1). Dielectric values were nominally 10, much lower than 25 as discussed in earlier chapters. The reason for this is series resistance in the device because the backside of the silicon

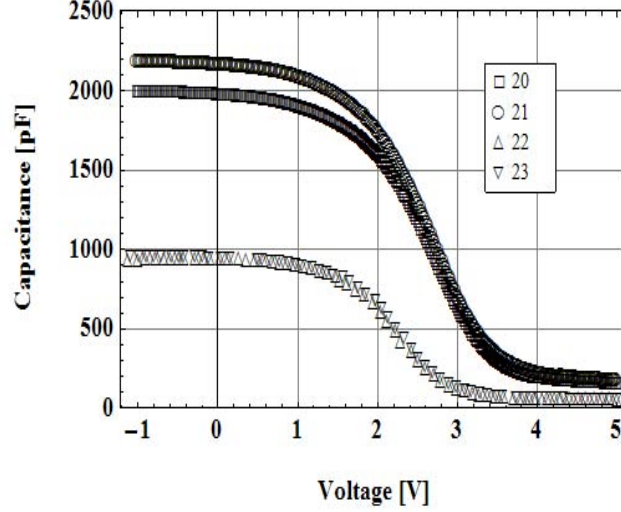


Figure 44. ALD CV curves were superior to the PLD CV curves. Capacitance range was 0 to 2 nF for the full contacts and 0 to 1 nF for the half contacts. The 2 top CV curves were used for gamma irradiation and the 2 bottom curves were used for ion irradiation. The capacitance range was very similar for all ALD samples as opposed to the limited range of some PLD samples.

wafer was used as an electrical connection. Without series compensation, the measured capacitance can be lower than the expected capacitance [18]. Nicolian and Brews (pages 222-226) provide equations, Equations 6-9, that can be used to make this correction

$$R_S = \frac{\left(\frac{G}{2\pi fC}\right)^2}{\left[1 + \left(\frac{G}{2\pi fC}\right)^2\right]G}, \quad (6)$$

$$a_R = G - [G^2 + (2\pi fC)^2]R_S, \quad (7)$$

$$C_{ADJ} = \frac{[G^2 + (2\pi fC)^2]C}{a_R^2 + (2\pi fC)^2}, \quad (8)$$

$$G_{ADJ} = \frac{[G^2 + (2\pi fC)^2]a_R}{a_R^2 + (2\pi fC)^2}, \quad (9)$$

where  $C$  is the measured parallel model capacitance,  $G$  is the measured conductance,  $f$  is the test frequency (1 MHz), and  $R_S$  is the series resistance. A representative example of pre-irradiated conductance plots for all ALD devices is shown in Figure 45 for sample 20. The conductance for the ALD samples appeared high at mS values



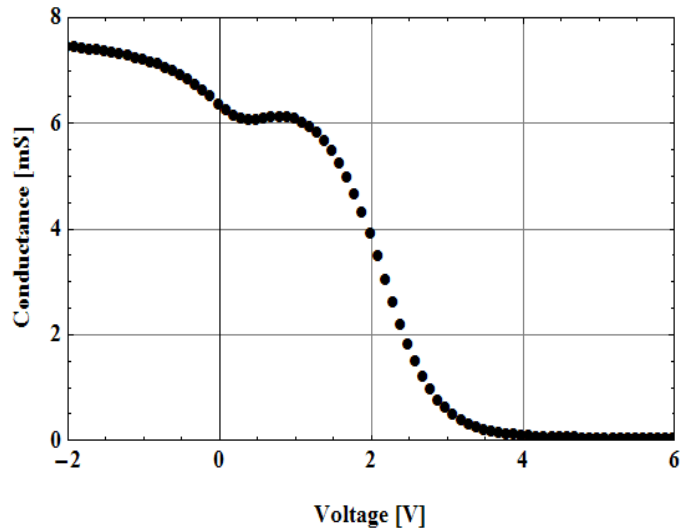


**Figure 45.** A representative example of a pre-irradiation conductance plot for all ALD devices. All plots were in the mS range and illustrated the similar feature of the plateau between 0 and 1 V.

and was shaped oddly with a plateau between 0 and 1 V. When Equation 8 was applied with the values from Figure 45,  $C_{ADJ}$  produced a conductance relation, as shown in Figure 46. However, when the adjusted  $C_{OX}$  values were used in the parallel plate capacitor equation, the dielectric constant was nominally 22. The parallel plate capacitor equation is shown as Equation 10,

$$C_{OX} = \frac{\kappa * \epsilon_o * A}{t}, \quad (10)$$

where  $C_{OX}$  is the oxide capacitance,  $\kappa$  is the dielectric constant,  $\epsilon_o$  is the permittivity of free space,  $A$  is the area of the gate metal, and  $t$  is the thickness of the oxide. This dielectric constant is within values published in literature: 30 [35], 26 [2], 25 [3], and 20 [17]. The difference between the measured and adjusted conductance is shown in Figure 47 for sample 20. When the adjustment is made, the conductance values are approximately half of the measured values.

The conductance plot should look like Figure 48. This was a result of measuring

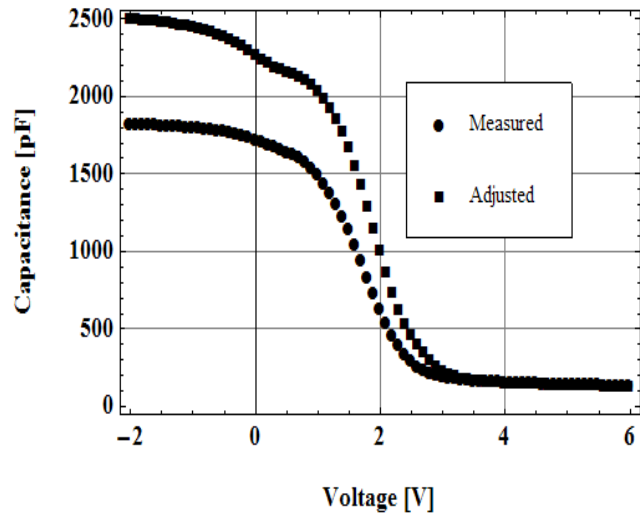


Figure 46. This plot illustrates the difference between the measured capacitance and the adjusted capacitance accounting for series resistance. Note that the adjusted capacitance takes on the features from the conductance plot due to the correction equations.

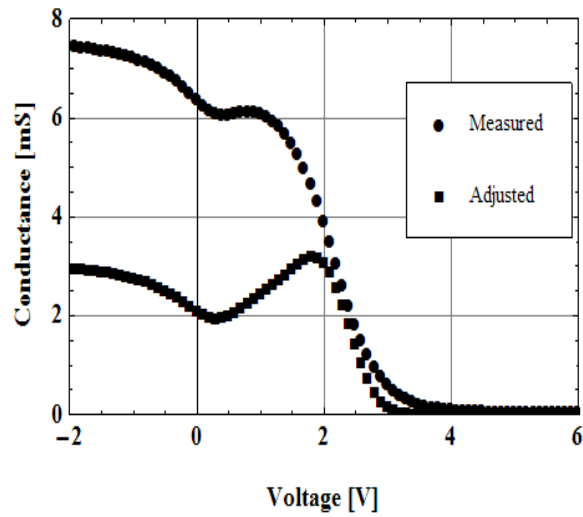


Figure 47. This plot illustrates the difference between the measured conductance and the adjusted conductance accounting for series resistance. The adjusted curve is approximately half the size of the measured conductance.

a 50 nm SiO<sub>2</sub> on n-type silicon with a poly-silicon gate of similar area as the ALD top contacts. It was measured with exactly the same equipment as the ALD devices. The only difference was that it was measured at 100 kHz. A 1 MHz frequency caused a bump in the slope of the CV plot around 0 V whereas the 100 kHz frequency illustrated a smooth characteristic high frequency CV plot. Note that Figure 48 is

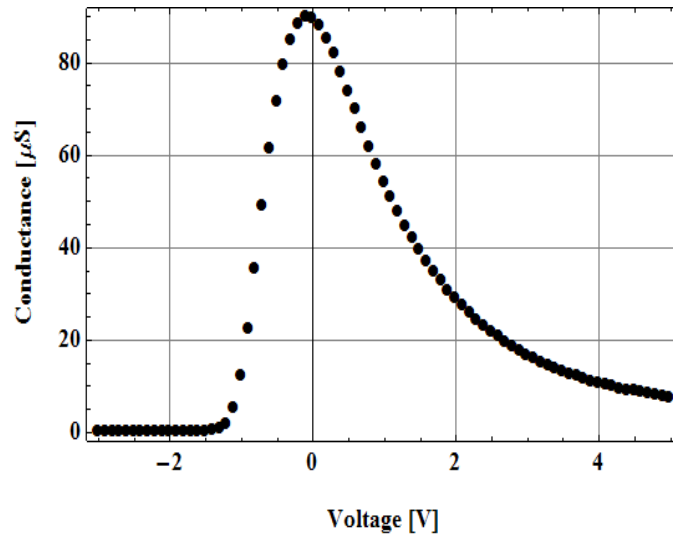


Figure 48. This plot came from a 50nm SiO<sub>2</sub> on top of n-type silicon substrate with a poly-silicon gate. It was measured with exactly the same equipment as all the other ALD devices. This plot illustrates what a conductance plot should look like. If a device was made properly, it should be in the  $\mu\text{S}$  range.

much different than that of ALD devices. Specifically, it is approximately 3 orders of magnitude lower, in the  $\mu\text{S}$  range. It is possible that the difference in test frequency contributed to the magnitude difference. Nicollian and Brews [18] mentioned, without quantification, that utilization of two different gate metals can also contribute to increased conductance due to differences in work functions. Reduction in gate area as well as adding a passivation layer could possibly reduce this large conductance.

Unfortunately, conductance measurements were not possible during all irradiations due to conductance range limitations of the different capacitance meters used. As a result, corrections were not possible for all measurements. The only corrections

that could be performed in this work were the ALD gamma irradiation measurements. All other CV plots shown in this document are “as measured” values.

## 4.6 Irradiations

Many irradiations were performed for this work and Table 5 gives a summary of all. CV results of these irradiations are presented in the next chapter. Only the ALD irradiations were analyzed beyond the raw results due to reasons discussed in the previous section. The PLD ion irradiation contained 9 irradiations of  $1.5 \times 10^{11}$  ions/cm<sup>2</sup> which totaled 56 Mrad(Si). The first ALD 1 MeV Si ion irradiation contained 10 irradiations of  $10^8$  ions/cm<sup>2</sup> totaling to 70 krad(Si). The second 1-MeV Si ion irradiation contained 10 irradiations of  $5 \times 10^8$  ions/cm<sup>2</sup> adding up to 250 krad(Si).

**Table 5. Irradiations Summary**

ID	Type	Irradiation	Duration	Dose <sub>tot</sub>
4	PLD	Gamma (0V)	140 min	1 Mrad(Si)
3	PLD	Gamma (5V)	140 min	1 Mrad(Si)
2	PLD	Neutron (0V)	2 hrs	25 krad(Si)
1	PLD	Neutron (5V)	2 hrs	25 krad(Si)
6	PLD	Ion (0V)	4 hrs	56 Mrad(Si)
20	ALD	Gamma (0V)	140 min	1 Mrad(Si)
21	ALD	Gamma (5V)	140 min	1 Mrad(Si)
22	ALD	Ion (0V)	2 hrs	70 krad(Si)
22	ALD	Ion (0V)	2 hrs	250 krad(Si)

## V. Experimental Results

The PLD devices gave inconclusive results for all irradiations. Little insight on radiation effects in  $\text{HfO}_2$  was extracted from this data. Regardless, those results are shown and plausible explanations are given to help explain the effects in the oxide. Gamma and ion irradiation results for the ALD devices are presented. Significant insight was obtained from these results. Specifically, very little shift toward less positive (lower) voltages in CV plots was measured for the gamma irradiation with both biased and unbiased samples. This indicates not only strong  $\text{HfO}_2$  resistance to gamma irradiation but also little electric field dependence. The ALD ion irradiation illustrated large reduction in the oxide capacitance with relatively small dose. However, the oxide also demonstrated rapid annealing possibly due to immediate recombination.

### 5.1 Rutherford Backscattering Results

RBS is an ion scattering technique that is used for compositional thin film analysis. RBS was used in this work to analyze the composition of samples and to verify oxide elemental concentration and thickness. During an RBS measurement, 2-MeV helium (+2) ions were directed onto a  $\text{HfO}_2$  sample and the energy distribution and yield of the backscattered helium ions at a given angle were recorded. Since the backscattering cross section for each element was known, it was possible to obtain quantitative depth profiles from the RBS spectra.

Hafnium and oxygen concentrations in the deposited  $\text{HfO}_2$  were found through a ratio of each elements areal density to that of the total  $\text{HfO}_2$  areal density. The thickness of the oxide was extracted by dividing the total  $\text{HfO}_2$  areal density by the atomic density. The areal density, in units of [atoms/cm<sup>2</sup>], was found using Simulation for Nuclear Reaction Analysis (SIMNRA) software simulations [36]. Conceptually,

areal density is described through the thin film equation, Equation 11 [37].

$$(Nt)_i = \frac{Y_i \times \cos(\theta)}{Q \times \Omega \times \sigma_i(E, \theta)} \quad (11)$$

In Equation 11,  $N$  is the atomic density,  $t$  is thickness,  $Y_i$  is the yield or area under the peaks, shown in Figures 49 and 50;  $Q$  is the number of ions hitting the surface of the sample,  $\Omega$  is the detector solid angle, and  $\sigma_i(E, \theta)$  is the scattering cross section for element  $i$  at energy  $E$  and scattering angle  $\theta$ . SIMNRA was used since Equation 11 only works for very thin films. SIMNRA more accurately determines the concentration because it iteratively determines areal density as the ion traverses the film, taking into account the ion energy loss and changes in  $\sigma_i(E, \theta)$ . Additional details on the thin film equation and the RBS technique can be found in [38] and [39].

The backscattered ions were detected in an Ortec silicon surface barrier detector. The backscattering angle was  $164^\circ$ . This backscattering angle was chosen because it was convenient to mount the backscattering detector at that location (i.e. it did not interfere with the incoming beam) and it helped to maximize the mass resolution or ability to resolve masses in the backscattering spectrum [37]. Additional information on backscattering angle selection can be found in [38]. The solid angle of the detector was approximately  $6.62 \times 10^{-3}$  steradians.  $10 \mu\text{C}$  of charge for each spectrum was collected which translates to  $3.12 \times 10^{13}$  helium (+2) ions hitting the sample. The sample tilt angle was  $0^\circ$ , which means that the beam axis was normal to the sample [37].

The RBS and SIMNRA simulation spectra for two PLD samples is shown in Figure 49. The PLD samples were obtained from packaged devices, specifically sample 9 and 16 described in Tables 2 and 3. Sample 9 was representative of the PLD ion irradiated device. In the spectra from left to right, the first small peak is oxygen, the drop off at the end of the plateau is silicon, and the large peak is hafnium. The

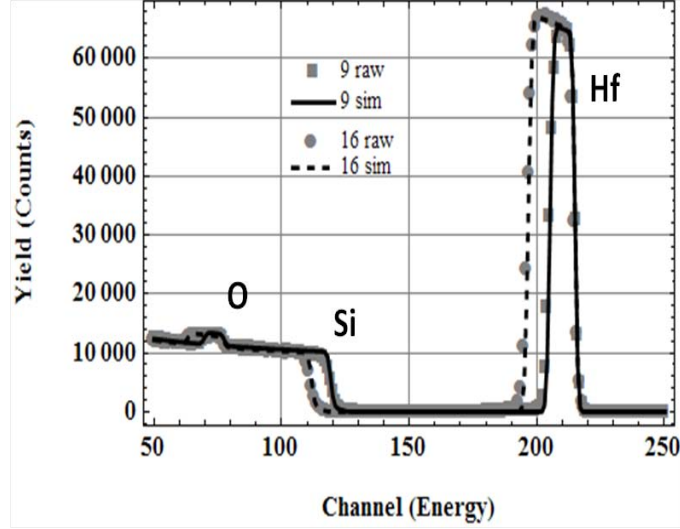


Figure 49. Results of the PLD devices indicate non-uniformity of oxide layer as well as discrepancies in stoichiometry. From left to right the notable features of the graph show oxygen, silicon, and hafnium. The width difference correlates to a thickness difference in the samples.

continuum results from a gradual energy loss dependent on the electron density and the ion distance traveled in the sample. Figure 49 shows a clear deviation in the PLD devices. Both samples were labeled thin and one turned out to be substantially thicker than the other, as illustrated by the difference in the widths of the peaks of both oxygen and hafnium. This result indicates non-uniform deposition of the  $\text{HfO}_2$ . A summary of these results is given in Table 6.

Table 6. PLD RBS Results Summary

Sample	Hf %	Oxygen %	Thickness [ $\text{at}/\text{cm}^2$ ]	Thickness [nm]
9	31	69	$6.85 \times 10^{17}$	82.45
16	33.5	66.5	$1.23 \times 10^{18}$	148.1

For comparison to the PLD samples, two ALD samples with no metal contacts were used for the RBS experiment. They were taken from opposite ends of a two-inch diameter circular wafer ( $\text{HfO}_2$  on Silicon) in order to check oxide uniformity and composition. The results of this experiment is shown in Figure 50. Uniformity was verified due to no difference in the widths of the peaks between the two samples. In

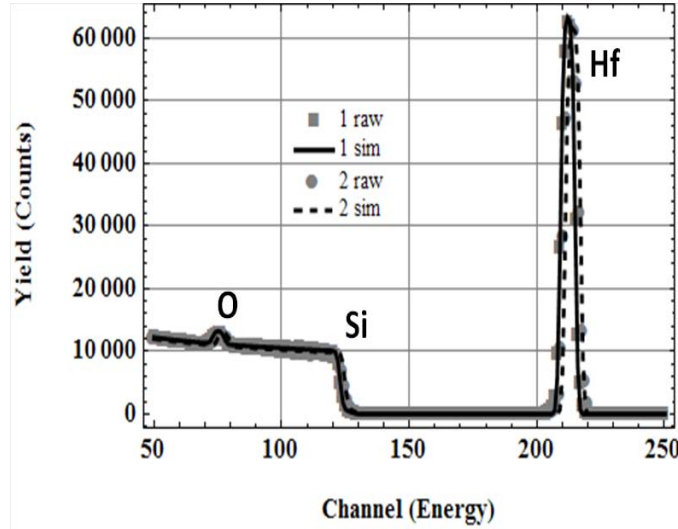


Figure 50. Two bare samples from different regions of one 2 inch wafer were used for RBS. Results of the ALD devices indicate uniformity of thickness and stoichiometry with the oxide layer.

spite of this uniformity, it is noteworthy to observe a 30% hafnium and 70% oxygen in the stoichiometry of these samples as opposed to the PLD samples being closer to the 33% and 66% as expected for exact  $\text{HfO}_2$  stoichiometry. Table 7 gives a summary of the ALD results.

Table 7. ALD RBS Results Summary

Sample	Hf %	Oxygen %	Thickness [ $\text{at}/\text{cm}^2$ ]	Thickness [nm]
ALD1	30	70	$4.05 \times 10^{17}$	48.75
ALD2	30	70	$4.18 \times 10^{17}$	50.31

## 5.2 Gamma Irradiation Results

The PLD gamma irradiation CV measurements provided little in terms of insight into damage mechanisms and hardness. The 0 V bias irradiation produced no change after a 1 Mrad(Si) irradiation. The results are shown in Figure 51 for sample 4. The negative capacitance was due to not correcting for and compensating the 15-foot BNC cables. Once correctly compensated, negative capacitance was not observed. The 5



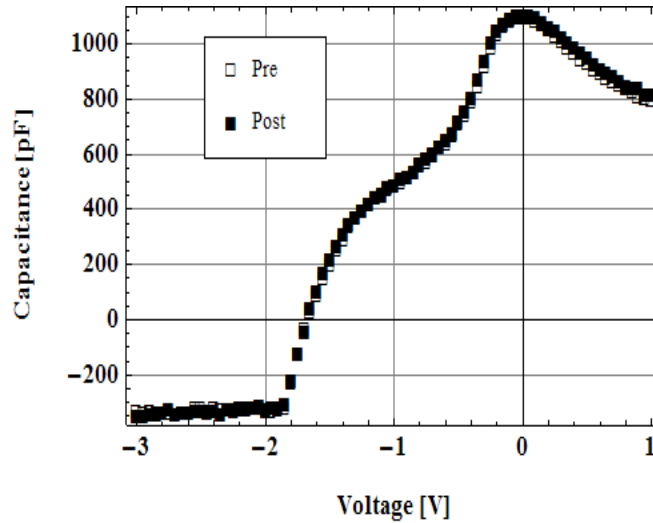


**Figure 51.** The 0 V bias PLD #4 gamma irradiation results indicate no change between pre- and post-irradiation measurements.

V PLD gamma irradiation did produce a change due to the strong electric field. The raw data of pre- and post-1 Mrad(Si) irradiation is shown in Figure 52 for sample 3. Upon inspection, the most noteworthy changes are a drop in the overall capacitance, as well as, possible shifting to a steeper slope in the CV plot. This would indicate trap density changes at the oxide/silicon interface.

The ALD devices were irradiated for the same amount of time, dose, and bias conditions. The 0 V bias irradiation result is shown in Figure 53 for sample 20 and indicates a small negative parallel shift to less positive voltages. This indicates possible recombination of holes with negatively charged fixed oxide traps. The 5 V bias was intended to move holes to the interface, however this is clearly not indicated in Figure 54 for sample 21. In fact, Figure 54 shows a plot nearly identical to that of the 0 V bias irradiation. No shifting with a strong electric field would indicate recombination of EHPs generated from gamma irradiation. The shifting is though to be due to localized hole recombination with negatively charged fixed oxide traps.

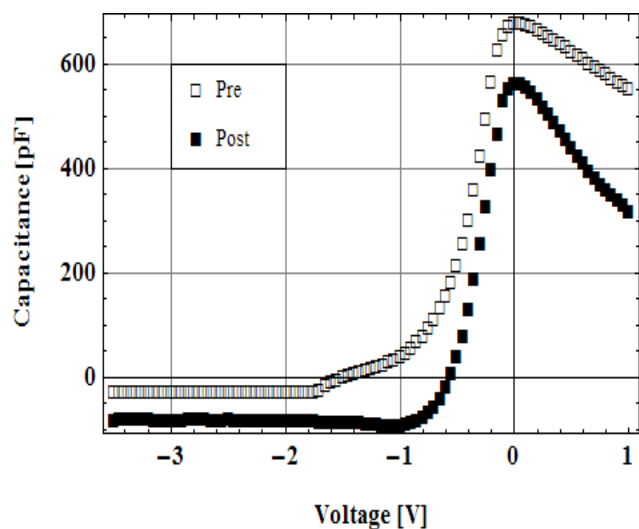


Figure 52. The 5 V bias PLD #3 gamma irradiation results show voltage shift and a change in depletion slope indicating interface trap recombination.

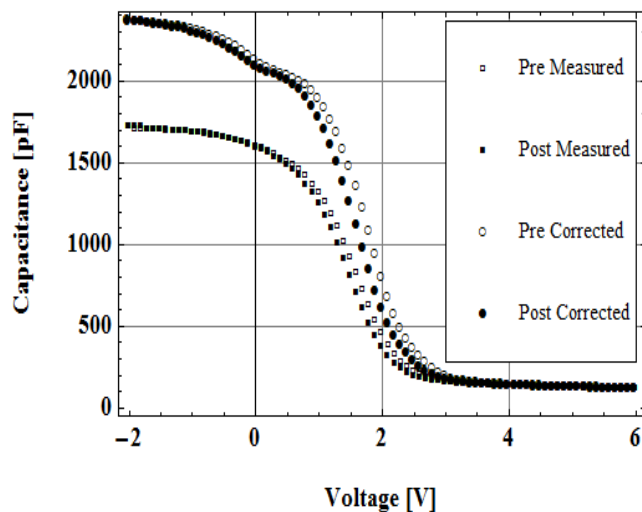


Figure 53. The 0 V ALD #20 gamma irradiation results show a slight voltage shift indicating negatively charged oxide trap recombination.

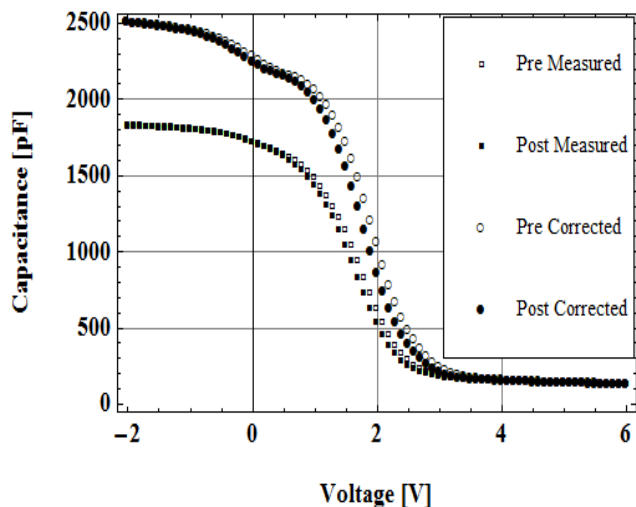


Figure 54. The 5 V ALD #21 gamma irradiation results show voltage shifting no different than the unbiased gamma irradiated device. This indicates quick local oxide trap recombination and no trap formation with a strong electric field.

### 5.3 Neutron Irradiation Results

Only PLD devices were neutron irradiated. Time and reactor schedule was not available to complete a neutron irradiation with the ALD devices. Both devices were irradiated for 2 hours. CV measurements were performed in situ at 10 minute intervals. A slight increase in the minimum capacitance and slope of a CV plot is shown in Figure 55 for sample 2. This change however is over approximately 1 pF. The 5 V irradiation illustrated a similar result as the 0 V bias irradiation only that the entire curve seems to shift in a more parallel fashion giving an increasing capacitance. This effect is seen in Figure 56 for sample 1. This effect could be explained by analyzing the conductance plot in Figure 57. The decreasing conductance indicates that the device is becoming more resistive. In addition to this shifting, it saturated at approximately 40 minutes during irradiation.

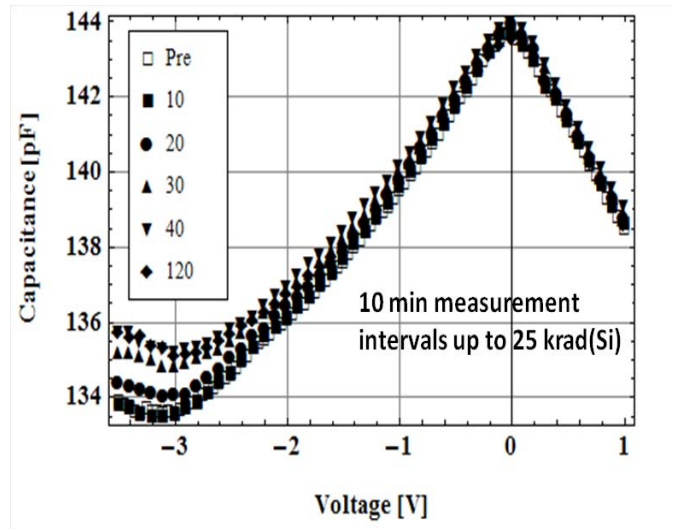


Figure 55. The 0 V PLD #2 neutron irradiation results indicate small shifting in the inversion region as well as saturation at 40 minutes of irradiation. The plots suffer in capacitance range and the shifts are within error of measurement.

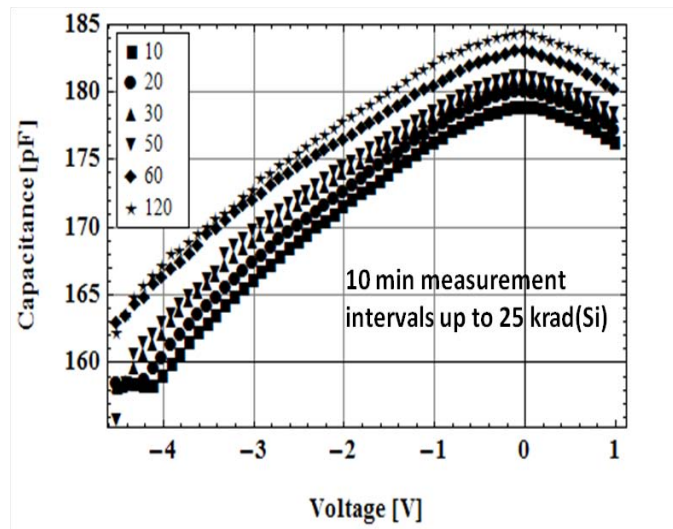


Figure 56. The 5 V PLD #1 neutron irradiation results indicate an overall increase in the CV plot throughout 2 hours of irradiation. The plots suffer in capacitance range and the shifts are within error of measurement.

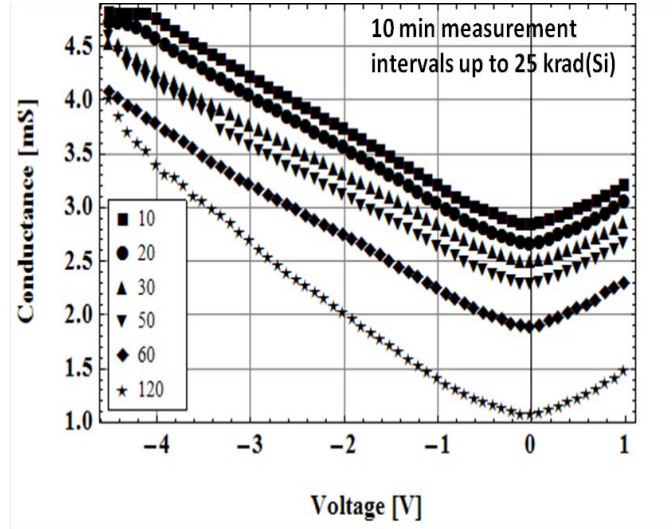


Figure 57. The 5 V PLD #1 neutron irradiation conductance plot illustrates that the device is becoming more resistive with increasing irradiation time.

#### 5.4 Ion Irradiation Results

Ion irradiation was performed with the PLD and ALD devices. Only one device, sample 6, was used for the PLD irradiation with 9 irradiations of  $1.5 \times 10^{11}$  [ions/cm<sup>2</sup>] and 1 final irradiation of approximately  $2.7 \times 10^{13}$  [ions/cm<sup>2</sup>]. The main features of the PLD result are shown in Figure 58 and 59. Pre- and post-irradiation results up through shot 6 is shown in Figure 58. Here minimum capacitance steadily increased along with the slope of the CV. There are possibly paths in the oxide being filled and charge is steadily building up forcing a shift to more negative voltages. The remaining PLD ion irradiations, whereby the trending discontinues and the overall plot seems to shift toward smaller capacitance, is shown in Figure 59. Characteristics of the beam during these irradiations were recorded and are shown in Table 8.

Two devices were used for the ALD irradiations with 10 iterations of  $10^8$  and  $5 \times 10^8$  ions/cm<sup>2</sup>. The first device results are shown in Figures 60 and 61 for sample 22. Pre- and post-final irradiation is shown in Figure 60. There is an overall decrease in the oxide capacitance and shifting to less positive voltages. This indicates a recom-

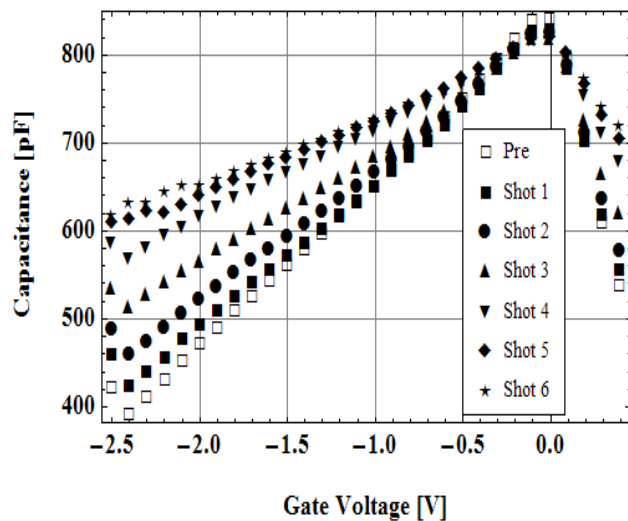


Figure 58. The PLD #6 ion irradiation results indicate a gradual flattening in the slope through 6 irradiations of  $1.5 \times 10^{11} \frac{\text{ions}}{\text{cm}^2}$ .

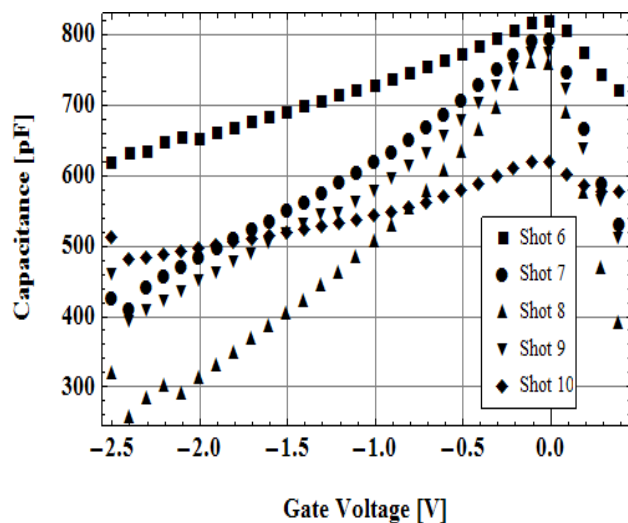


Figure 59. The remaining shots of the PLD sample #6 ion irradiation with  $1.5 \times 10^{11} \frac{\text{ions}}{\text{cm}^2}$  indicate a departure from the trend in Figure 47. A change in the structure of the oxide is a possible explanation due to a very high dose received by shot 7. Irradiation #10 flattens the CV entirely due to a 30 second irradiation.

**Table 8. PLD #6:  $1.5 \times 10^{11} \frac{\text{ions}}{\text{cm}^2}$  Irradiation Summary**

Shot	Pulse [s]	Current [nA]	$\phi_{cum} \times 10^{11} \frac{\text{ions}}{\text{cm}^2}$	Total Dose [Mrad(Si)]
1	0.135	5.5	1.55	6.23
2	0.135	5.5	3.10	12.5
3	0.143	5.2	4.65	18.7
4	0.152	4.9	6.20	24.9
5	0.186	4.0	7.75	31.2
6	0.233	3.2	9.30	37.4
7	0.375	2.0	10.9	43.6
8	0.746	1.0	12.4	49.8
9	1.25	0.6	14.0	56.1
10	30	0.45	294	1181

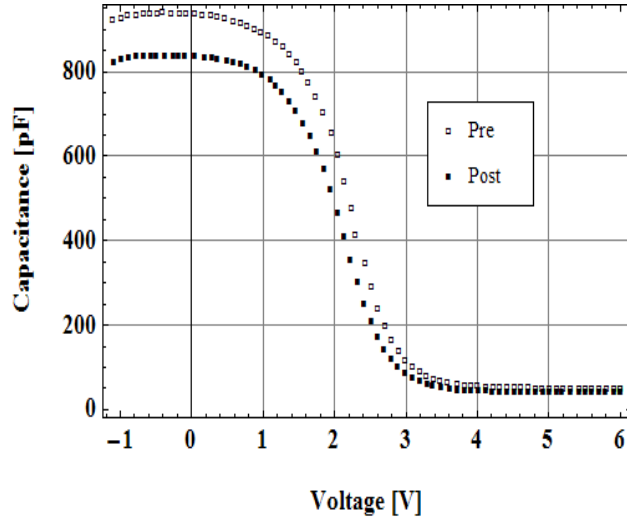


Figure 60. The ALD sample #22 ion irradiation of  $10^8 \frac{\text{ions}}{\text{cm}^2}$  illustrate a decrease in oxide capacitance and slight voltage shifting toward less positive voltages between pre- and post-irradiation #10 measurements.

combination of holes with some of the negatively trapped charge in the oxide. Overall trending with successive irradiation shots is shown in Figure 61. These shots were

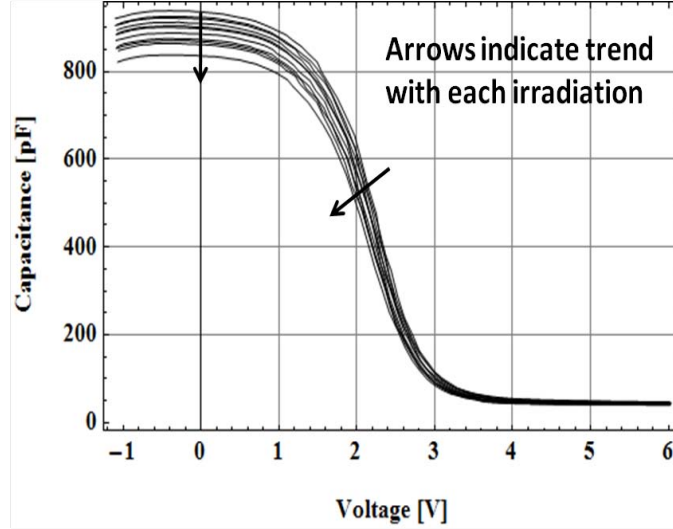


Figure 61. All measurement results of the ALD #22 ion irradiation with  $10^8 \frac{\text{ions}}{\text{cm}^2}$  shots illustrate trends with decreasing oxide capacitance and shifting toward less positive voltages.

much more stable and the fluence along with associated error could be given with some certainty. This is summarized in Table 9.

Table 9. ALD #22:  $10^8 \frac{\text{ions}}{\text{cm}^2}$  Irradiation Summary

Shot	$\phi \times 10^8 \frac{\text{ions}}{\text{cm}^2}$	Dose [krad(Si)]	$\phi_{cum} \times 10^8 \frac{\text{ions}}{\text{cm}^2}$	Total Dose [krad(Si)]
1	$1.05 \pm 0.23$	$6.52 \pm 1.60$	$1.05 \pm 0.23$	$6.52 \pm 1.60$
2	$1.08 \pm 0.24$	$6.70 \pm 1.67$	$2.13 \pm 0.33$	$13.22 \pm 2.53$
3	$1.03 \pm 0.21$	$6.39 \pm 1.48$	$3.16 \pm 0.39$	$19.61 \pm 3.27$
4	$1.02 \pm 0.25$	$6.33 \pm 1.70$	$4.18 \pm 0.47$	$25.94 \pm 4.08$
5	$1.07 \pm 0.25$	$6.64 \pm 1.72$	$5.25 \pm 0.53$	$32.59 \pm 4.89$
6	$1.01 \pm 0.23$	$6.27 \pm 1.59$	$6.26 \pm 0.58$	$38.86 \pm 5.61$
7	$1.07 \pm 0.24$	$6.64 \pm 1.66$	$7.33 \pm 0.63$	$45.50 \pm 6.37$
8	$1.02 \pm 0.21$	$6.33 \pm 1.48$	$8.35 \pm 0.66$	$51.83 \pm 7.06$
9	$1.10 \pm 0.24$	$6.83 \pm 1.67$	$9.45 \pm 0.70$	$58.66 \pm 7.84$
10	$1.39 \pm 0.32$	$8.63 \pm 2.21$	$10.8 \pm 0.77$	$67.28 \pm 8.88$

The second set of irradiations ( $5 \times 10^8 \text{ ions/cm}^2$ ) for sample 23 with the same experimental conditions as the  $1 \times 10^8 \text{ ions/cm}^2$  irradiations illustrated the same result



as the first, only to a larger extent. This is illustrated in Figures 62 and 63. Pre- and post-final irradiation is shown in Figure 62. 3 voltage sweeps were taken after each irradiation for statistical purposes and only results from the first voltage sweep are shown in the plots. The change with each irradiation is shown in Figure 63.

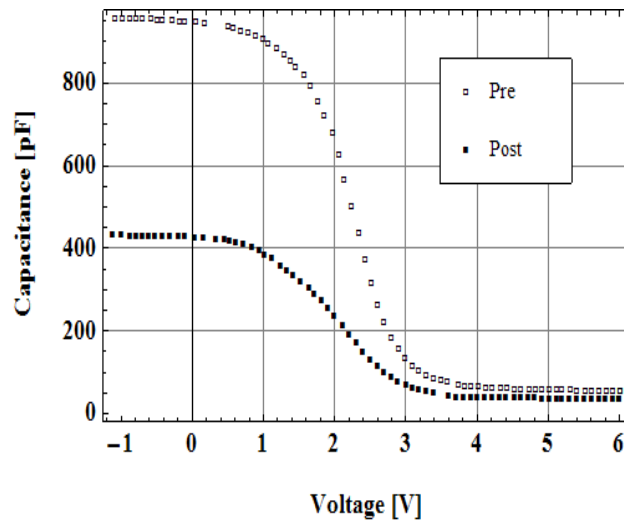


**Figure 62.** The ALD #23 ion irradiation of  $5 \times 10^8 \frac{\text{ions}}{\text{cm}^2}$  illustrate a decrease in oxide capacitance and voltage shifting toward less positive voltages between pre- and post-shot 10 measurements.

Notice that some irradiations cause larger differentials than others, this leads to the conclusion that some irradiations had a larger effects than others. As with the  $10^8$  irradiations, these irradiations were also stable and the fluence along with associated error could be given with some certainty. This is summarized in Table 10.

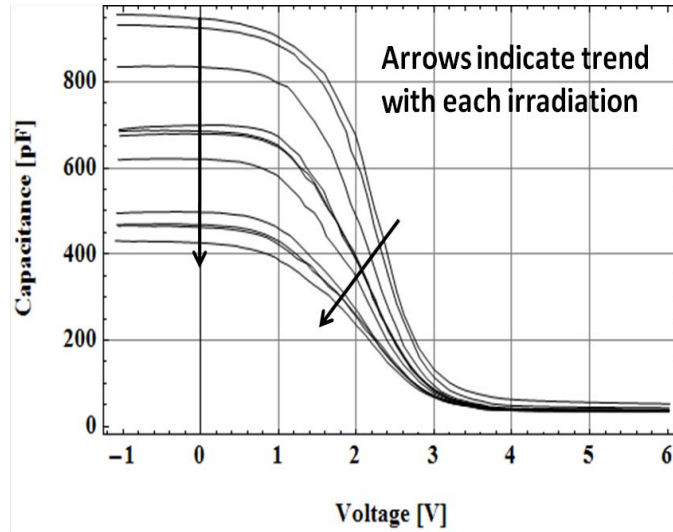


Figure 63. All measurement results of the ALD sample #23 ion irradiation with  $5 \times 10^8 \frac{\text{ions}}{\text{cm}^2}$  irradiations illustrate trends with decreasing oxide capacitance and shifting toward less positive voltages.

Table 10. ALD #23:  $5 \times 10^8 \frac{\text{ions}}{\text{cm}^2}$  Irradiation Summary

Shot	$\phi \times 10^8 \frac{\text{ions}}{\text{cm}^2}$	Dose [krad(Si)]	$\phi_{cum} \times 10^8 \frac{\text{ions}}{\text{cm}^2}$	Total Dose [krad(Si)]
1	$3.99 \pm 0.96$	$24.77 \pm 6.56$	$3.99 \pm 0.960$	$24.77 \pm 6.56$
2	$4.01 \pm 0.88$	$24.89 \pm 6.12$	$8.00 \pm 1.30$	$49.66 \pm 9.79$
3	$4.19 \pm 1.00$	$26.01 \pm 6.85$	$12.2 \pm 1.64$	$75.66 \pm 13.21$
4	$3.99 \pm 0.89$	$24.77 \pm 6.17$	$16.2 \pm 1.87$	$100.43 \pm 16.09$
5	$4.06 \pm 0.92$	$25.20 \pm 6.36$	$20.2 \pm 2.08$	$125.63 \pm 19.02$
6	$4.26 \pm 0.93$	$26.44 \pm 6.48$	$24.5 \pm 2.28$	$152.07 \pm 22.04$
7	$3.99 \pm 0.93$	$24.77 \pm 6.39$	$28.5 \pm 2.46$	$176.83 \pm 24.89$
8	$3.68 \pm 0.87$	$22.84 \pm 5.97$	$32.2 \pm 2.61$	$199.68 \pm 27.48$
9	$3.94 \pm 0.93$	$24.46 \pm 6.38$	$36.1 \pm 2.77$	$224.13 \pm 30.27$
10	$3.96 \pm 0.91$	$24.58 \pm 6.27$	$40.1 \pm 2.92$	$248.71 \pm 33.04$

## VI. Analysis and Discussion

The ALD gamma and ion irradiations produced changes in the CV characteristics that were a result of changes in the oxide and not due to either contamination of devices or irradiation equipment variations (i.e. beam current, equipment malfunction, etc). This experimental evidence was confirmation by the RBS experiment and that all irradiations were performed in situ in order to minimize equipment variation during irradiation.

In general,  $V_{MG}$  shifted by 0.2 V for all irradiations with plots of normalized capacitance (i.e.  $C/C_{OX}$ ). Since these irradiations were done to a high dose, this result shows  $\text{HfO}_2$ 's radiation resilience to both TID and NIEL effects. These radiation effects in  $\text{HfO}_2$  MOSCAPS show no dependence on gate bias. The results of the 0 V and 5 V gamma irradiation are nearly identical to within statistical uncertainty.

The ion irradiation showed a decreasing  $C_{OX}$  with each irradiation. The decreasing  $C_{OX}$  is suspected to result from the bombarding ions causing displacement damage in the metal contacts forming a thin metal/oxide layer that dominates overall capacitance in the device. This was unavoidable due to the thickness of the metal contacts and the ion energy required to reach the oxide layer. The metal contacts were required to be relatively thick (at least 1000 Å) for wire bonding and to allow in situ measurements. This makes it difficult for displacement damage to occur in the oxide only.

The  $5 \times 10^8$  ions/cm<sup>2</sup> irradiation illustrated interface trap formation as well as rapid annealing after each irradiation at room temperature. Quantitatively, the interface traps contributed to -0.6 V  $V_{FB}$  shift. Annealing refers to the recovery of  $C_{OX}$  after an ion irradiation shot. Recovery seemed to occur very quickly over a very large capacitance range.

## 6.1 Oxide Trapped Charge

The gamma irradiation results showed voltage shifting of approximately 0.2 V which leads to a suspicion of either the formation of positively trapped charge or the recombination of negatively trapped charge in the oxide. Also, a strong positive bias did not affect the formation or removal of trapped charge. This indicates either short EHP lifetime due to recombination or small trap density in the oxide that allows for EHPs to be removed from the oxide through the metal contacts.

In order to quantify changes in trapped charge, both midgap capacitance ( $C_{MG}$ ) and  $V_{MG}$  required extraction from the irradiation data.  $C_{MG}$  was calculated from Equation 12 found in [18],

$$C_{MG} = C_{OX} \left[ 1 - 0.5 \left( \frac{C_{OX}}{C_{OX} + C_{MIN}} \right) \right], \quad (12)$$

where  $C_{OX}$  is the oxide capacitance in the accumulation region and  $C_{MIN}$  is the minimum capacitance in the inversion region. Once  $C_{MG}$  was known,  $V_{MG}$  could be found by matching  $C_{MG}$  to the applied gate voltage in the experimental data.  $\Delta V_{MG}$  was used to quantify the formation or removal of oxide trapped charge through Equation 13 from [4],

$$\Delta N_{OT} = \frac{-C_{OX} \times \Delta V_{MG}}{q \times A}, \quad (13)$$

where  $N_{OT}$  is oxide trap density in [ $\#/cm^2$ ],  $q$  is the charge of an electron and  $A$  is the area of the gate.

In order to verify the existence of formation or removal of trapped charge, normalized capacitance plots were constructed. The normalized capacitance for the 0 V bias ALD gamma irradiation of sample 20 is shown in Figure 64. Total  $V_{MG}$  shifting was approximately -0.18 V after 1 Mrad(Si). The change in the oxide trap density seems to be linear with dose in Figure 65. This plot is not an indication of trap formation

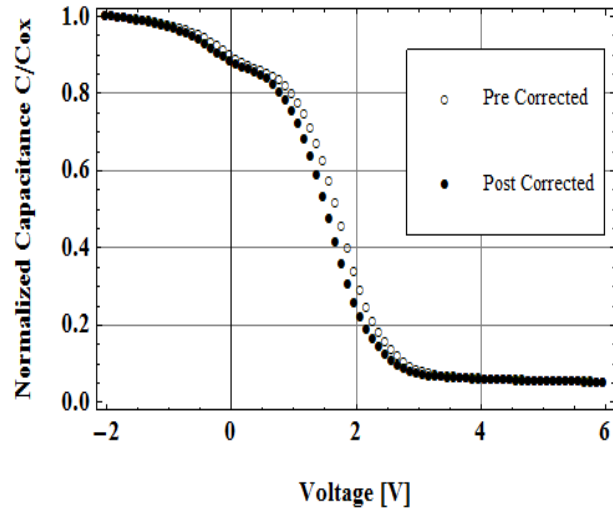


Figure 64. The normalized capacitance 0 V bias ALD #20 gamma irradiation plot illustrates a shift of approximately 0.2 V to less positive voltages. This is indicative of recombination of negatively trapped charge in the oxide.

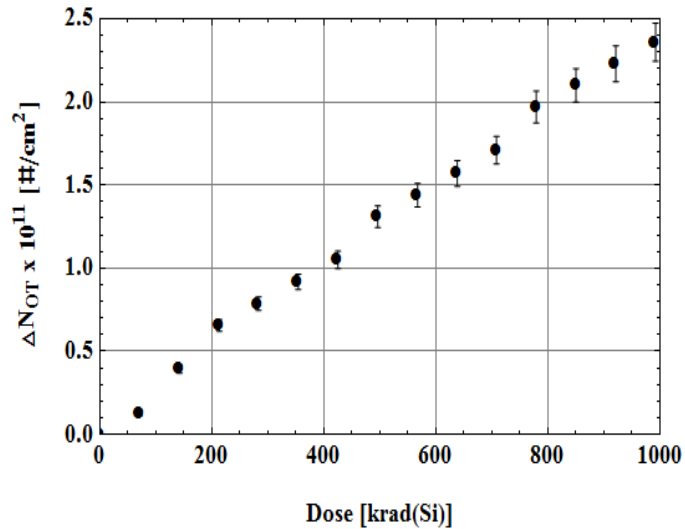


Figure 65. There is a linear increase with the change in oxide trap density with increasing dose for the 0 V bias ALD #20 gamma irradiation.

but rather the number of recombinations that occurred to remove negatively trapped charge. The reason for this has to do with the location of the CV plot prior to irradiation. If no negative charge was in the oxide prior to irradiation, the curve would be shifted to the left where the slope would begin to decrease around 0 V. This is not the case. In order to verify this theory, an inspection of the metal-semiconductor work function was necessary. This is presented in the next section. Table 11 is a summary of the 0 V bias gamma irradiation analysis where  $C_{OX}$  is approximately 2371 pF and the area is 0.0113 cm<sup>2</sup>.

**Table 11. ALD #20: 0 V Gamma Oxide Trap Analysis**

Time [min]	Total Dose [krad(Si)]	$V_{MG}$ [V]	$\Delta V_{MG}$ [V]	$\Delta N_{OT} \times 10^{11} [\frac{\#}{cm^2}]$
0	0	1.69	0	0
10	71 ± 3	1.68	-0.01	0.13 ± 0.02
20	142 ± 6	1.66	-0.03	0.39 ± 0.02
30	213 ± 9	1.64	-0.05	0.66 ± 0.03
40	283 ± 11	1.63	-0.06	0.79 ± 0.04
50	354 ± 14	1.62	-0.07	0.92 ± 0.05
60	425 ± 17	1.61	-0.08	1.05 ± 0.05
70	496 ± 20	1.59	-0.10	1.31 ± 0.06
80	567 ± 23	1.58	-0.11	1.44 ± 0.07
90	638 ± 26	1.57	-0.12	1.57 ± 0.08
100	708 ± 28	1.56	-0.13	1.71 ± 0.08
110	779 ± 31	1.54	-0.15	1.97 ± 0.10
120	850 ± 34	1.53	-0.16	2.10 ± 0.10
130	921 ± 37	1.52	-0.17	2.23 ± 0.11
140	992 ± 40	1.51	-0.18	2.36 ± 0.11

The normalized capacitance for the 5 V bias ALD gamma irradiation of sample 21 is shown in Figure 66. Total  $V_{MG}$  shifting was approximately -0.15 V after 1 Mrad(Si). The change in the oxide trap density seems to be linear with dose as with the 0 V bias irradiation in Figure 67. Table 12 is a summary of the 5 V bias gamma irradiation analysis where  $C_{OX}$  is approximately 2508 pF and the area is 0.0113 cm<sup>2</sup>. The shifting was a little less than the 0 V bias. This is most likely due to less recombination with negatively trapped charge as a result of a strong electric field.

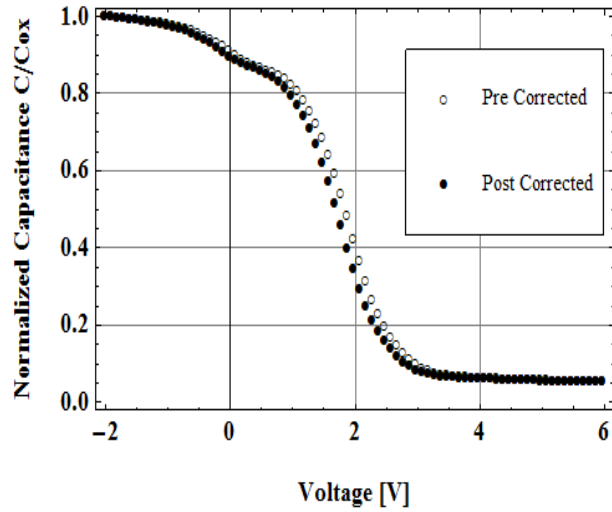


Figure 66. The normalized capacitance 5 V bias ALD #21 gamma irradiation plot illustrates a shift of approximately 0.2 V to less positive voltages. This is indicative recombination of negatively trapped charge in the oxide. Also note no bias dependence on voltage shifting.

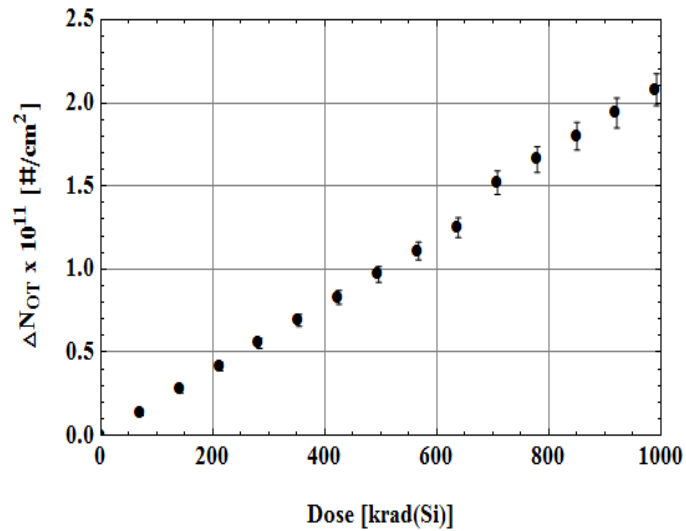


Figure 67. There is a linear increase with the change in oxide trap density with increasing dose for the 5 V bias ALD #21 gamma irradiation.

**Table 12. ALD #21: 5 V Gamma Oxide Trap Analysis**

Time [min]	Total Dose [krad(Si)]	$V_{MG}$ [V]	$\Delta V_{MG}$ [V]	$\Delta N_{OT} \times 10^{10} [\frac{\#}{cm^2}]$
0	0	1.83	0	0
10	$71 \pm 3$	1.82	-0.01	$0.14 \pm 0.02$
20	$142 \pm 6$	1.81	-0.02	$0.28 \pm 0.02$
30	$213 \pm 9$	1.80	-0.03	$0.42 \pm 0.03$
40	$283 \pm 11$	1.79	-0.04	$0.55 \pm 0.03$
50	$354 \pm 14$	1.78	-0.04	$0.69 \pm 0.04$
60	$425 \pm 17$	1.77	-0.06	$0.83 \pm 0.04$
70	$496 \pm 20$	1.76	-0.07	$0.97 \pm 0.05$
80	$567 \pm 23$	1.75	-0.08	$1.11 \pm 0.05$
90	$638 \pm 26$	1.74	-0.09	$1.25 \pm 0.06$
100	$708 \pm 28$	1.72	-0.11	$1.52 \pm 0.07$
110	$779 \pm 31$	1.71	-0.12	$1.66 \pm 0.08$
120	$850 \pm 34$	1.70	-0.13	$1.80 \pm 0.08$
130	$921 \pm 37$	1.69	-0.14	$1.94 \pm 0.09$
140	$992 \pm 40$	1.68	-0.15	$2.08 \pm 0.10$

The normalized capacitance of  $10^8$  ion irradiation for sample 22 is shown in Figures 68 and 69. Pre- and post-final irradiation is shown in Figure 68. The normalized shift is illustrated in Figure 69. Total  $V_{MG}$  shifting was approximately -0.13 V. This is less than both gamma irradiations, which is not unexpected since the total dose was approximately 70 krad(Si). The change in oxide trap density as a function of dose is shown in Figure 70. Here the plot indicates a linear increase with a  $R^2$  of approximately 0.94. However, it is not as readily apparent as with the gamma irradiation with a  $R^2$  of approximately 0.99. The reason for this is the resolution of the measurement device, Boonton 7200. Not as many points were used for the voltage sweep as with the gamma irradiation. Table 13 is a summary of the  $10^8$  ion irradiation analysis summary where  $C_{OX}$  is approximately 939 pF and the area is  $0.0057 \text{ cm}^2$ .

The normalized capacitance of the  $5 \times 10^8$  ion irradiation for sample 23 is shown in Figures 71 and 72. The pre- and post-irradiation is shown in Figure 71. This illustrates not only  $V_{MG}$  shifting but also a slope change which would indicate inter-



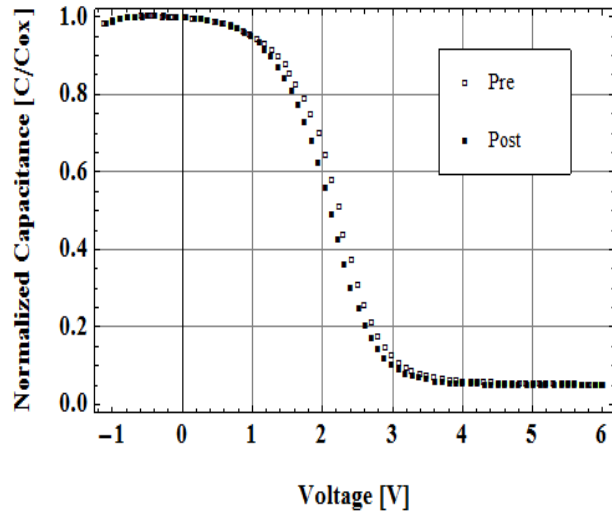


Figure 68. Normalized capacitance of pre- and post-irradiation #10 of ALD #22 with  $10^8 \frac{\text{ions}}{\text{cm}^2}$  irradiations indicate formation of oxide trapped charge with parallel shifting toward less positive voltages.

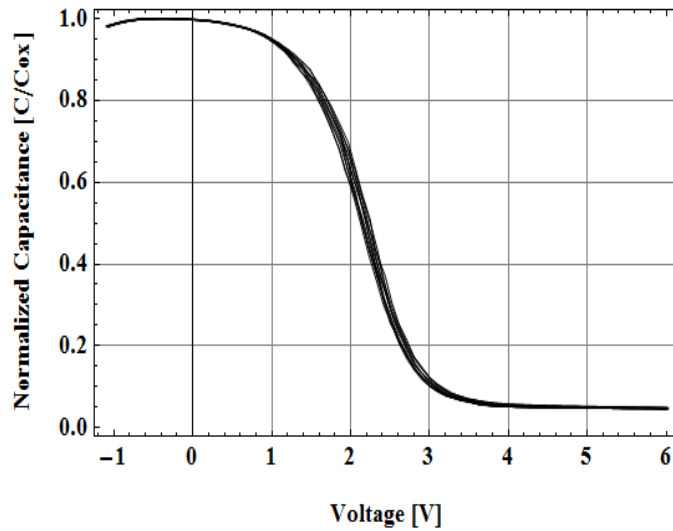


Figure 69. Normalized capacitance of all  $10^8 \frac{\text{ions}}{\text{cm}^2}$  irradiations illustrate the trend for formation of oxide trapped charge in ALD #22.

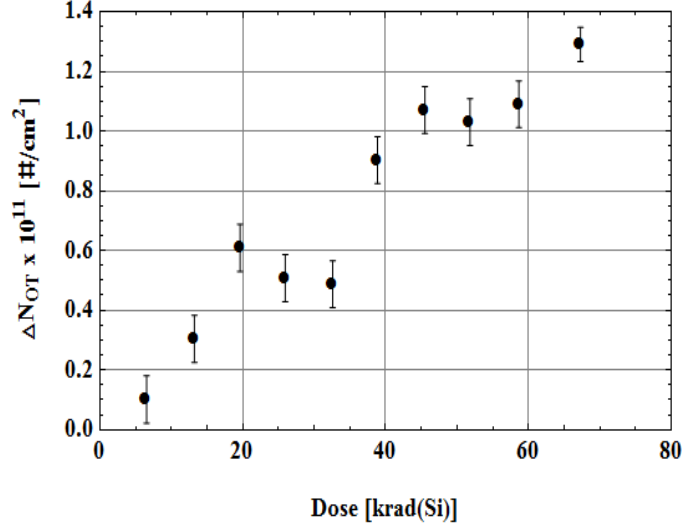
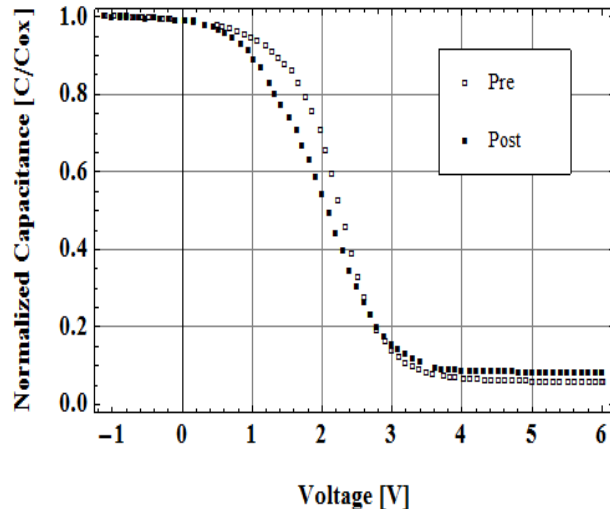


Figure 70. There is a linear increase with the change in oxide trap density with increasing dose for ten shots of  $10^8$  ion irradiation of ALD #22. This linear increase is not as apparent as the gamma irradiation due to the resolution of the measurement device used.

Table 13. ALD #22:  $10^8 \frac{ions}{cm^2}$  Oxide Trap Analysis

Shot #	Total Dose [krad(Si)]	$V_{MG}$ [V]	$\Delta V_{MG}$ [V]	$\Delta N_{OT} \times 10^{10} [\frac{\#}{cm^2}]$
0	0	2.22	0	0
1	$7 \pm 2$	2.21	$-0.01 \pm 0.01$	$1.01 \pm 0.79$
2	$13 \pm 3$	2.19	$-0.03 \pm 0.01$	$3.04 \pm 0.79$
3	$20 \pm 3$	2.16	$-0.06 \pm 0.01$	$6.09 \pm 0.79$
4	$26 \pm 4$	2.17	$-0.05 \pm 0.01$	$5.07 \pm 0.79$
5	$33 \pm 5$	2.18	$-0.05 \pm 0.01$	$4.87 \pm 0.78$
6	$39 \pm 6$	2.13	$-0.09 \pm 0.01$	$9.03 \pm 0.78$
7	$46 \pm 6$	2.12	$-0.11 \pm 0.01$	$10.7 \pm 0.8$
8	$52 \pm 7$	2.12	$-0.10 \pm 0.01$	$10.3 \pm 0.8$
9	$59 \pm 8$	2.12	$-0.11 \pm 0.01$	$10.9 \pm 0.8$
10	$67 \pm 9$	2.09	$-0.13 \pm 0.01$	$12.9 \pm 0.6$

face trap formation. Interface trap formation is discussed in the next section. The normalized trend is illustrated in Figure 72. Total  $V_{MG}$  shifting was approximately



**Figure 71.** Normalized capacitance of pre- and post-irradiation #10 of ALD #23 with  $5 \times 10^8 \frac{\text{ions}}{\text{cm}^2}$  irradiations indicate formation of oxide and interface trapped charge with shifting and slope change toward less positive voltages.

-0.22 V. This is a greater shift than all other irradiations. The total dose here was approximately 250 krad(Si), which is a quarter of the dose from the gamma irradiation. The change in oxide trap density as a function of dose is shown in Figure 73. Here the plot does not indicate linearity. A line fit gives approximately 0.8 for  $R^2$ . Rather, there seems to be a saturation where there is no further change. It is possible that from the combined effects of TID and NIEL most of the negative charge that originally existed in the oxide was removed. Table 14 is a summary of the  $5 \times 10^8$  ion irradiation oxide trap analysis summary where  $C_{OX}$  is approximately 956 pF and the area is  $0.0057 \text{ cm}^2$ .

## 6.2 Interface Trapped Charge

The  $5 \times 10^8$  ion irradiation clearly indicated the existence of interface traps from Figure 71. A similar looking plot explaining interface trapped charge is illustrated in

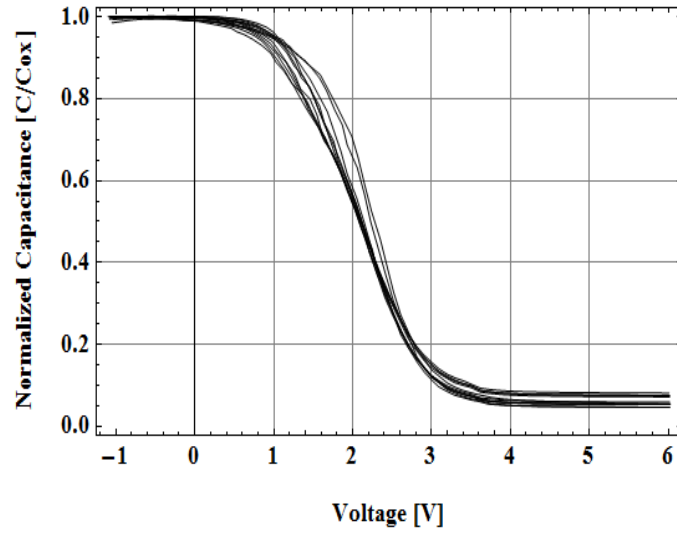


Figure 72. Normalized capacitance of all  $5 \times 10^8 \frac{\text{ions}}{\text{cm}^2}$  irradiations illustrate the trend for formation of oxide and interface trapped charge.

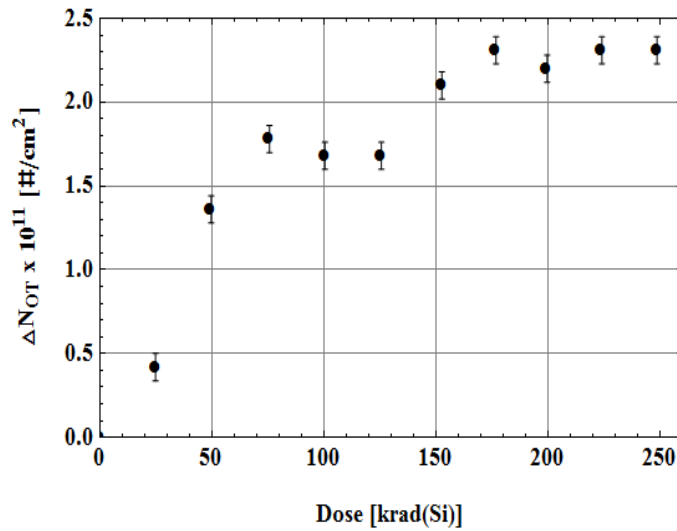


Figure 73. The change in oxide trap density with increasing dose appears to saturate for 10 irradiations of  $5 \times 10^8 \frac{\text{ions}}{\text{cm}^2}$ .

**Table 14. ALD #23:  $5 \times 10^8 \frac{\text{ions}}{\text{cm}^2}$  Oxide Trap Analysis**

Shot #	Total Dose [krad(Si)]	$V_{MG}$ [V]	$\Delta V_{MG}$ [V]	$\Delta N_{OT} \times 10^{11} [\frac{\#}{\text{cm}^2}]$
0	0	2.24	0	0
1	$25 \pm 7$	2.20	$-0.04 \pm 0.01$	$0.42 \pm 0.08$
2	$50 \pm 10$	2.11	$-0.13 \pm 0.01$	$1.36 \pm 0.08$
3	$76 \pm 13$	2.07	$-0.17 \pm 0.01$	$1.78 \pm 0.08$
4	$100 \pm 16$	2.08	$-0.16 \pm 0.01$	$1.68 \pm 0.08$
5	$126 \pm 19$	2.08	$-0.16 \pm 0.01$	$1.68 \pm 0.08$
6	$153 \pm 22$	2.04	$-0.20 \pm 0.01$	$2.10 \pm 0.08$
7	$177 \pm 25$	2.02	$-0.22 \pm 0.01$	$2.31 \pm 0.08$
8	$200 \pm 28$	2.03	$-0.21 \pm 0.01$	$2.20 \pm 0.08$
9	$224 \pm 30$	2.02	$-0.22 \pm 0.01$	$2.31 \pm 0.08$
10	$249 \pm 33$	2.02	$-0.22 \pm 0.01$	$2.31 \pm 0.08$

Schroder [40], page 343. In order to quantify the level of interface traps a plot of the change in interface trap density as a function of dose was constructed. In order to do this, a calculation of the  $V_{FB}$  was required. Subsequently, many other parameters required plotting and calculation. The substrate doping concentration is given as Equation 14 from page 63 of [40].

$$N_{SUB} = \frac{2}{q \times \epsilon_s \times A^2 \times \left(\frac{\Delta 1/C^2}{\Delta V_G}\right)}, \quad (14)$$

where  $N_{SUB}$  is the substrate doping concentration in [ $\text{cm}^{-3}$ ],  $\epsilon_s$  is the permittivity of silicon in a vacuum ( $1.053 \times 10^{-12}$  [F/cm]),  $A$  is the gate area ( $0.0057 \text{ cm}^2$ ),  $\left(\frac{\Delta 1/C^2}{\Delta V_G}\right)$  is the slope from a  $1/C^2$  versus voltage plot. A plot of  $1/C^2$  versus voltage is shown in Figure 74. The slope was taken between 3 and 6 V and a value of  $9 \times 10^{19}$  [ $\text{F}^2/\text{V}$ ] was obtained. Next, a calculation of the extrinsic Debye length was required. The Debye length is used to represent electrical interaction range. It indicates how far an electrical event can be sensed within a semiconductor. This is given from [18] page 63 as Equation 15,

$$\lambda = \sqrt{\frac{\epsilon_s \times k \times T}{q^2 \times N}}, \quad (15)$$

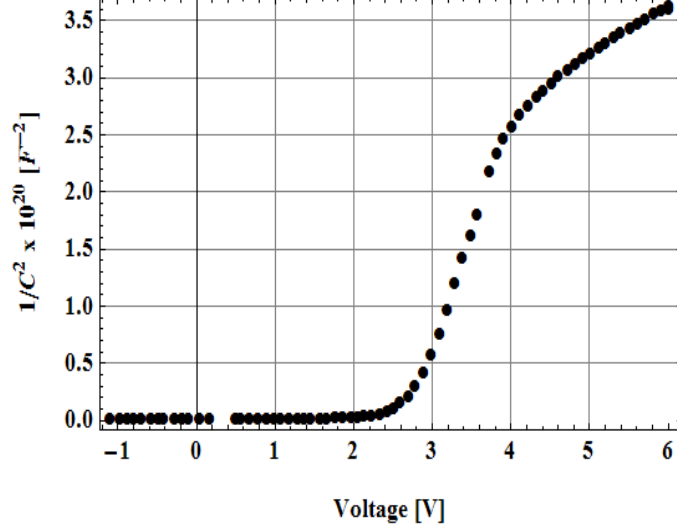


Figure 74. In order to calculate the Debye length, the substrate doping density was needed. In order to calculate the doping density, the slope from this pre irradiation plot was needed. The slope value was taken by constructing a trend line from -3 to 6 V. A value of  $9 \times 10^{19}$  [F/V<sup>2</sup>] was obtained and used for calculations.

where  $\lambda$  is the extrinsic Debye length in [cm] and  $k \times T$  is thermal energy at room temperature (293K)( $4.046 \times 10^{-21}$  J). All other parameters have been introduced previously. The flat band capacitance was needed to extract the  $V_{FB}$ . This calculation, from [18] page 487, was Equation 16

$$C_{FB} = \frac{1}{(1/C_{OX}) + (\lambda/\epsilon_s)}, \quad (16)$$

where  $C_{FB}$  is in units of [F/cm<sup>2</sup>]. Thus, this value needed to be multiplied by the area to obtain the actual flat band capacitance value. Once this value was obtained,  $V_{FB}$  was extracted by matching  $C_{FB}$  to the gate voltage value in the experimental data. Lastly, once  $V_{FB}$  was obtained,  $\Delta N_{IT}$  could be calculated in Equation 17 from [4] where all parameters have been introduced previously.

$$\Delta N_{IT} = \frac{C_{OX} \times (\Delta V_{FB} - \Delta V_{MG})}{q \times A} \quad (17)$$

This calculation was performed for all 10 irradiations. A plot of the change in interface trap density as a function of dose is shown in Figure 75. This plot illustrates linearity

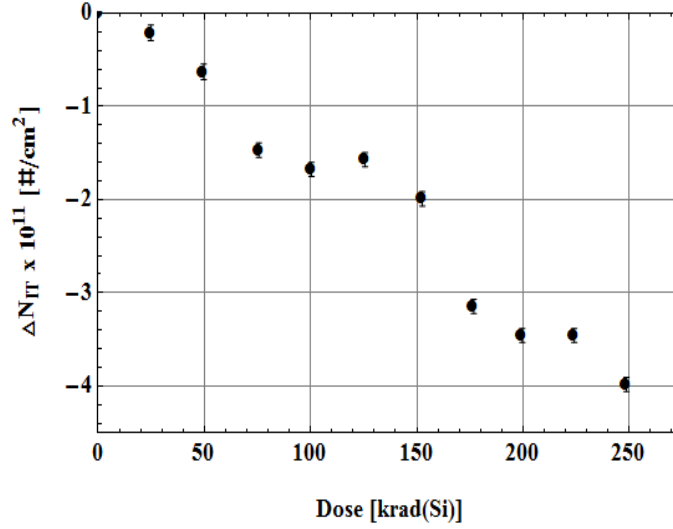


**Figure 75.** The change in interface trap density appears linear with increasing dose for ALD #23. This is different than an observation of saturation in the oxide trap density.

with increasing dose as opposed to the oxide trap density where it had appeared saturated. A summary of all calculations and values from this analysis is given in Table 15.

**Table 15. ALD #23:  $5 \times 10^8 \frac{ions}{cm^2}$  Interface Trap Analysis**

Shot #	Total Dose [krad(Si)]	$V_{FB}$ [V]	$\Delta V_{FB}$ [V]	$\Delta N_{IT} \times 10^{11} [\frac{\#}{cm^2}]$
0	0	2.29	0	0
1	$25 \pm 7$	2.23	$-0.06 \pm 0.01$	$-0.21 \pm 0.08$
2	$50 \pm 10$	2.10	$-0.19 \pm 0.01$	$-0.63 \pm 0.08$
3	$76 \pm 13$	1.98	$-0.31 \pm 0.01$	$-1.47 \pm 0.08$
4	$100 \pm 16$	1.97	$-0.32 \pm 0.01$	$-1.68 \pm 0.08$
5	$126 \pm 19$	1.98	$-0.31 \pm 0.01$	$-1.57 \pm 0.08$
6	$153 \pm 22$	1.90	$-0.39 \pm 0.01$	$-1.99 \pm 0.08$
7	$177 \pm 25$	1.77	$-0.52 \pm 0.01$	$-3.14 \pm 0.08$
8	$200 \pm 28$	1.75	$-0.54 \pm 0.01$	$-3.46 \pm 0.07$
9	$224 \pm 30$	1.74	$-0.55 \pm 0.01$	$-3.46 \pm 0.07$
10	$249 \pm 33$	1.69	$-0.60 \pm 0.01$	$-3.98 \pm 0.07$

Upon inspection of all pre-irradiated ALD CV plots, it seems there is either a large

metal semiconductor work function or a lot of inherent negatively trapped charge. A qualitative review of negatively trapped charge was given in the expectation section of the first chapter. Since  $V_{FB}$  was calculated above it is convenient to study  $V_{FB}$ . The  $V_{FB}$  shift can be attributed to the difference between two values as defined in Equation 18 from [18] page 426,

$$V_{FB} = W_{MS} - Q_{EFF}, \quad (18)$$

where  $W_{MS}$  is the metal semiconductor work function and  $Q_{EFF}$  is trapped charge.  $Q_{EFF}$  includes interface trapped charge, oxide trapped charge, or mobile charges.  $W_{MS}$  can be calculated from Equation 19 in [18] page 465,

$$W_{MS} = W_M - [W_S + (\frac{E_{BG}}{2}) - \phi_B], \quad (19)$$

where  $W_M$  is the metal work function (Gold = 5.1 eV [41]),  $W_S$  is the silicon work function (4.6 eV [41]),  $E_{BG}$  is the energy band gap of silicon (1.12 eV [18]), and  $\phi_B$  is the bulk potential all in [eV].  $\phi_B$  is given by Equation 20 in [18] page 465,

$$\phi_B = \frac{-k \times T}{q} \times \ln(\frac{N_{SUB}}{N_i}), \quad (20)$$

where  $(k \times T/q)$  is 0.026 [eV] at room temperature,  $N_{SUB}$  is the calculated substrate doping concentration (approximately  $4 \times 10^{15} \text{ cm}^{-3}$ ), and  $N_i$  is the intrinsic doping concentration ( $1.45 \times 10^{10} \text{ cm}^{-3}$  [40]). With these numbers,  $W_{MS}$  is approximately -0.4 V. With flat band voltages in the 2 V range, as illustrated in Table 16, this would indicate a lot of negatively trapped charge possibly due to the way  $\text{HfO}_2$  was deposited on silicon through the ALD process. RBS revealed a larger concentration of oxygen atoms which could contribute to this negative charge. It is understandable



that the voltage shifts with irradiation were moving toward less positive values due to a large density of negatively trapped charge. It is surprising however that only small shifts ( $0.2 V_{MG}$  and  $-0.6 V_{FB}$ ) were observed.

### 6.3 Annealing Effects

Annealing was observed in the  $5 \times 10^8$  ion/cm<sup>2</sup> irradiation for sample 23. Specifically, the  $C_{OX}$  capacitance would drastically reduce (approximately 400-600 pF) immediately after every irradiation, then it would partially recover to higher values as 3 voltage sweeps were performed. This observation for 3 voltage sweeps immediately following irradiation 9 as shown in Figure 76. This was observed after every

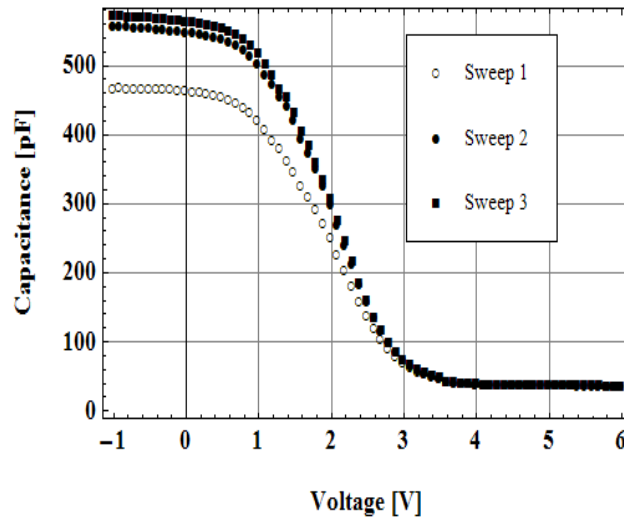


Figure 76. Showing the 3 sweeps that were taken after  $5 \times 10^8 \frac{ions}{cm^2}$  irradiations # 9. Most annealing occurs immediately after sweep 1. Notice the small difference between sweeps 2 and 3. 3 sweeps were taken after every shot initially for statistics. Rather the sweeps captured annealing effects. Each sweep was approximately 1 minute long and could not be altered due the measurement equipment setup used.

irradiation in Table 16 which gives the  $C_{OX}$  value at -1 V for all 3 sweeps.

A graphical representation of Table 16 is shown in Figure 77 which confirms this observation. It is unclear if the annealing was occurring due to the application of

**Table 16.  $C_{OX}$  at -1 V for 10 Irradiations of  $5 \times 10^8 \frac{ions}{cm^2}$**

Shot #	Sweep 1 [pF]	Sweep 2 [pF]	Sweep 3 [pF]	$\Delta (C_3-C_1)$ [pF]
Pre	956	956	956	0
1	931	941	943	12
2	835	909	915	80
3	691	855	868	177
4	675	814	830	155
5	686	787	803	117
6	620	746	762	142
7	496	655	676	180
8	469	594	614	145
9	466	556	572	106
10	430	511	527	97

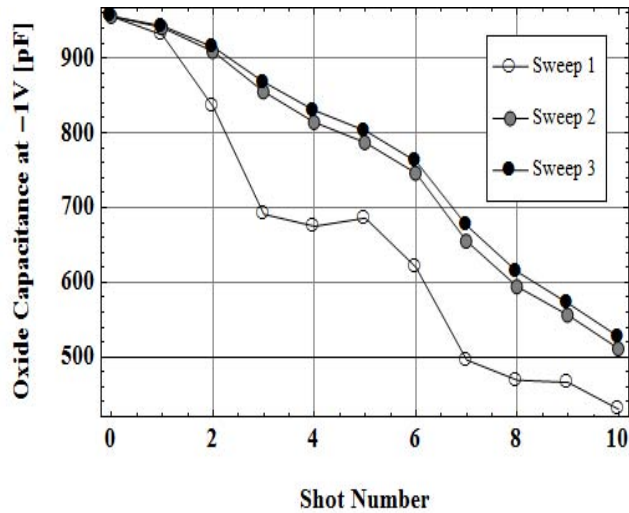


Figure 77. All sweeps indicated a decrease in the oxide capacitance. Sweep 1 shows a leveling off for a couple shots possibly indicating that the full irradiation shot did not hit the sample. However, sweeps 2 and 3 illustrate a linear decrease with each shot. Only sweep 1 was used for the previous plots of the ALD sample #23  $5 \times 10^8 \frac{ions}{cm^2}$  irradiations.

voltage. Upon inspection of Figure 76, it appears that there are clear interface traps due to slope differences. In order to check this theory, Figure 78 shows this plot of normalized capacitance for all three sweeps. These plots are almost identical which

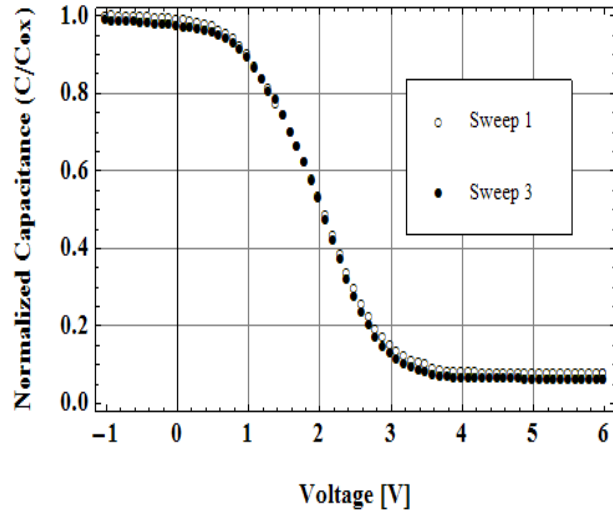


Figure 78. Showing a normalized version of Figure 76. These plots are almost identical which indicates neither oxide or interface trap differences.

indicates neither oxide or interface trap differences. It seems that most of the annealing is occurring in the silicon substrate at the oxide interface where the depletion region exists. This would explain the increasing  $C_{OX}$  and slope recovery.

## VII. Conclusions

This work explored the radiation effects on hafnium oxide-based MOS capacitors through analysis of CV plots and voltage shifting due to recombination of trapped charge as a function of dose. Gamma, neutron, and ion irradiations were performed on PLD devices. Only gamma and ion irradiations were performed on the ALD devices. In order to take measurements and isolate effects that might occur in the oxide, most measurements were taken in situ. This required device fabrication including: metalization, packaging, and wire bonding. The poor electrical characteristics of PLD samples drove further investigation into device fabrication. Samples were polished, cleaned, and annealed in order to improve pre-irradiation electrical characteristics. Also, various contact metals in different combinations were used in an effort to improve device response and to allow for wire bonding. Much of this effort was unsuccessful. However 200Å titanium followed by 2800Å gold proved to be the recipe of choice for successful wire bonding. The presence of pin holes and other residual laser deposition effects shown in Figure 41 in the oxide from the PLD samples is believed to be the source of poor electrical response. An RBS experiment verified that no contamination of the samples occurred, however, it highlighted that the oxide thickness in PLD devices was not uniform with two "thin" samples, approximately 82 nm and 140 nm respectively.

The ALD devices exhibited uniformity in the RBS experiment providing the same value of approximately 50 nm from two different sides of a wafer. They also exhibited better electrical response that facilitated quantitative analysis. Both gamma and ion irradiations illustrated  $V_{MG}$  shifting no more than approximately 0.2 V. The  $5 \times 10^8$  ions/cm<sup>3</sup> Si ion irradiation illustrated interface effects in addition to oxide trap effects. Quantitatively this resulted in a  $V_{FB}$  shift of approximately 0.6 V. All shifting occurred toward less positive voltages. It is believed that this shifting is the

result of recombination of positive charge with negatively charged oxide and interface traps. After quantifying the  $W_{MS}$  and the pre-irradiation  $V_{FB}$ , it is believed that the ALD samples contain approximately 2 V worth of negatively trapped charge. This supports the theory that elimination of negative trapped charge was occurring through recombination.

Other notable effects were the seemingly non-dependence on gate bias in the gamma irradiation, the decreasing  $C_{OX}$  with increasing ion dose, and the rapid annealing occurring in the ion irradiation. The little dependence on gate bias was found by comparing the CV plot of both the 0 V and 5 V bias applied between measurements during the gamma irradiation. No other description other than rapid annealing or quick recombination could explain this occurrence. The decreasing  $C_{OX}$  was due to the deposition of the bombarding silicon ions into the metal forming a metal/oxide layer. This was unavoidable due to the thickness of the metal contacts required for wire bonding and the ion energy required to reach the oxide layer. Rapid annealing was witnessed with the  $5 \times 10^8$  ions/cm<sup>3</sup> irradiation.  $C_{OX}$  initially dropped between 400 and 600 pF after each shot but subsequently increased between 100 to 200 pF after 3 voltage sweeps. It is unclear whether the application of voltage forced the annealing.

If this work was to be repeated, especially with ALD samples, a few device parameters would be changed in order to improve experimentation and measurement. Specifically, the capacitance correction equations require use if measurements are taken with the samples in packages. However, in order to use the capacitance correction equations, the conductance values require improvement into the  $\mu\text{S}$  range. Smaller metal contacts in both area and thickness and the addition of a passivation layer on top of the  $\text{HfO}_2$  but around the metal contacts might reduce conductance. A reduction of contact area would be required not only for improved conductance but

also to ensure that the area does not push capacitance values beyond the range of the CV meter. Thinner contacts, (no less than  $1000\text{\AA}$ ), would not only help conductance but also might allow for the ability to deposit ions in only the oxide layer if the ion irradiation experiment was to be repeated. This would illustrate quantitative voltage shifts real time and not require normalization to determine the presence of oxide or interface traps.

This work could proceed in many different directions. Thickness dependence experiments could be performed with the several ALD wafers obtained from this work. Temperature dependent irradiations were not performed and could easily be performed in gamma, neutron, or ion experiments. This would be useful in analyzing annealing effects. Since the combination of CV and IV during irradiation was attempted with only partial success with CV plots, a focused effort at obtaining pre- and post-irradiation IV plots would be useful and provide insight into leakage current. Also, further comparisons between PLD and ALD samples would be welcome in hopes to improve the PLD samples for capacitance measurement. Originally, the goal of this work was to obtain a damage constant ratio between neutron and ion irradiation using the Messenger-Spratt equation, Equation 1. This was attempted through lifetime measurements unsuccessfully.

A well known technique for lifetime measurement is the Zerbst method. It consists of biasing the capacitor from strong accumulation to deep depletion and measuring the capacitance as a function of time. After the measurement, a plot is constructed using the collected data and equations that were developed from first principles [40]. The slope of the plot gives the charge generation lifetime. The difficulty in this measurement comes from determining the bias voltages and measurement times necessary for the accumulation and deep depletion regions.

Pre- and post-irradiation lifetime measurements of both neutron and ion irra-

diations would provide the necessary information in order to calculate the damage constant from Equation 1. The damage equivalence between the two would prove useful for future irradiations; if only one was performed, the damage from the other type could be predicted. Lifetime measurements for HfO<sub>2</sub> based devices has not been found in literature. This type of investigation would provide a great deal of insight not only into the method of obtaining lifetime values but also insight into carrier lifetime and mobility which could help explain effects in the oxide due to irradiation. Good starting references are [42, 43, 44, 45].

## Bibliography

- [1] John Markoff. Intel says chips will run faster, using less power. *The New York Times*, 2007.
- [2] M. Houssa, L. Pantisano, L. Ragnarsson, R. Degraeve, T. Schram, G. Pourtois, S. De Gendt, G. Groeseneken, and M. M. Heyns. Electrical properties of high- $\kappa$  gate dielectrics: Challenges, current issues, and possible solutions. *Materials Science and Engineering: R: Reports*, 51(4-6):37–85, 4/30 2006.
- [3] R. K. Nahar, Vikram Singh, and Aparna Sharma. Study of electrical and microstructure properties of high dielectric hafnium oxide thin film for mos devices. *Journal of Materials Science: Materials in Electronics*, 18(6):615–619, 2007.
- [4] F. Belgin Ergin, Rasit Turan, Sergiu T. Shishiyanu, and Ercan Yilmaz. Effect of  $\gamma$ -radiation on hfo<sub>2</sub> based mos capacitor. *Nuclear Instruments and Methods in Physics Research Section B: Beam Interactions with Materials and Atoms*, 268(9):1482–1485, 5/1 2010.
- [5] A. Y. Kang, P. M. Lenahan, and J. F. Conley Jr. The radiation response of the high dielectric-constant hafnium oxide/silicon system. *IEEE Transactions on Nuclear Science*, 49(6):2636–2642, 2002.
- [6] L. W. Massengill, B. K. Choi, D. M. Fleetwood, R. D. Schrimpf, K. F. Galloway, M. R. Shaneyfelt, T. L. Meisenheimer, P. E. Dodd, J. R. Schwank, Y. M. Lee, R. S. Johnson, and G. Lucovsky. Heavy-ion-induced breakdown in ultra-thin gate oxides and high-k dielectrics. *IEEE Transactions on Nuclear Science*, 48(6):1904–1912, 2001.
- [7] P. S. Winokur, J. R. Schwank, P. J. McWhorter, P. V. Dressendorfer, and D. C. Turpin. Correlating the radiation response of mos capacitors and transistors. *IEEE Transactions on Nuclear Science*, 31(6):1453–1460, 1984.
- [8] Andrew Holmes-Siedle and Len Adams. *Handbook of Radiation Effects*. Oxford University Press, New York, NY, 2007.
- [9] J. A. Felix, J. R. Schwank, D. M. Fleetwood, M. R. Shaneyfelt, and E. P. Gusev. Effects of radiation and charge trapping on the reliability of high- $\kappa$  gate dielectrics. *Microelectronics Reliability*, 44(4):563–575, 4 2004.
- [10] J. A. Felix, D. M. Fleetwood, R. D. Schrimpf, J. G. Hong, G. Lucovsky, J. R. Schwank, and M. R. Shaneyfelt. Total-dose radiation response of hafnium-silicate capacitors. *IEEE Transactions on Nuclear Science*, 49(6):3191–3196, 2002.
- [11] T. R. Oldham and F. B. McLean. Total ionizing dose effects in mos oxides and devices. *IEEE Transactions on Nuclear Science*, 50(3):483–499, 2003.



- [12] J.R. Srour. Displacement damage effects in electronic materials, devices, and integrated circuits. In *Tutorial short Course Notes*, page 30. IEEE Nuclear and Space Radiation Effects Conference, July 1988.
- [13] G. C. Messenger and J. P. Spratt. The effects of neutron irradiation on germanium and silicon. *Proceedings of the IRE*, 46(6):1038–1044, 1958.
- [14] I. Ketsman, Y.B. Losovyj, A. Sokolov, J. Tang, Z. Wang, K.D. Belashchenko, and P.A. Dowben. The n-type gd-doped hfo<sub>2</sub> to silicon heterojunction diode. *Applied Physics A: Materials Science amp; Processing*, 89:489–492, 2007. 10.1007/s00339-007-4154-y.
- [15] Ya B. Losovyj, Ihor Ketsman, A. Sokolov, K. D. Belashchenko, P. A. Dowben, Jinke Tang, and Zhenjun Wang. The electronic structure change with gd doping of hfo<sub>2</sub> on silicon. *Applied Physics Letters*, 91(13):132908–132908–3, 2007.
- [16] Anand Deshpande, Ronald Inman, Gregory Jursich, and Christos Takoudis. Atomic layer deposition and characterization of hafnium oxide grown on silicon from tetrakis(diethylamino)hafnium and water vapor. *Journal of Vacuum Science Technology A: Vacuum, Surfaces, and Films*, 22(5):2035–2040, 2004.
- [17] Riikka L. Puurunen, Annelies Delabie, Sven Van Elshocht, Matty Caymax, Martin L. Green, Bert Brijs, Olivier Richard, Hugo Bender, Thierry Conard, Ilse Hoflijck, Wilfried Vandervorst, David Hellin, Danielle Vanhaeren, Chao Zhao, Stefan De Gendt, and Marc Heyns. Hafnium oxide films by atomic layer deposition for high- $\kappa$  gate dielectric applications: Analysis of the density of nanometer-thin films. *Applied Physics Letters*, 86(7):073116–073116–3, 2005.
- [18] Nicollian E.H. and Brews J.R. *MOS (Metal Oxide Semiconductor) Physics and Technology*. John Wiley and Sons, Hoboken, NJ, 2003.
- [19] H. Wong, N. Zhan, K. L. Ng, M. C. Poon, and C. W. Kok. Interface and oxide traps in high-[kappa] hafnium oxide films. *Thin Solid Films*, 462-463:96–100, 2004. Proceedings of the International Conference on Materials for Advanced Technologies (ICMAT 2003), Symposium L: Advances in Materials for Si Microelectronics - From Processing to Packaging.
- [20] W. J. Zhu, Tso-Ping Ma, T. Tamagawa, J. Kim, and Y. Di. Current transport in metal/hafnium oxide/silicon structure. *IEEE Electron Device Letters*, 23(2):97–99, 2002.
- [21] Seok-Woo Nam, Jung-Ho Yoo, Suheun Nam, Hyo-Jick Choi, Dongwon Lee, Dae-Hong Ko, Joo Ho Moon, Ja-Hum Ku, and Siyoung Choi. Influence of annealing condition on the properties of sputtered hafnium oxide. *Journal of Non-Crystalline Solids*, 303(1):139–143, 2002.

- [22] ISO/ASTM 51205-09. *Standard Practice for Use of a Ceric-Cerous Sulfate Dosimetry System*. ASTM International, West Conshohocken, PA, 2009. [www.astm.org](http://www.astm.org).
- [23] K.G. Kerris. Practical dosimetry for radiation hardness testing. In *NSREC Short Course Notes*, pages 1–9, Harry Diamond Laboratories, 1992.
- [24] J.H. Hubbell and S.M. Seltzer. Tables of x-ray mass attenuation coefficients and mass energy-absorption coefficients. [Online]. Available: at <http://physics.nist.gov/PhysRefData/XrayMassCoef/>.
- [25] T.E. Gray. Investigation of gate current in neutron irradiated algal/gan heterostructure field effect transistors using voltage and temperature dependence. Master’s thesis, Air Force Institute of Technology (AU), WPAFB, OH, March 2007.
- [26] J.W. VanDenBerg P.J. Griffen, J.G. Kelly. *User’s Manual for SNL-SAND-II Code*. Sandia National Laboratory, April 1994. Code available from RSICC.
- [27] Knief Ronald A. *Nuclear Engineering - Theory and Technology of Commercial Nuclear Power*. American Nuclear Society, La Grange Park, IL, 2008.
- [28] Joe Talnagi. personal correspondence, November 2010.
- [29] ASTM Standard E722. *Standard Practice for Characterizing Neutron Energy Fluence Spectra in Terms of an Equivalent Monoenergetic Neutron Fluence for Radiation Hardness Testing of Electronics*. ASTM International, West Conshohocken, PA, 1994 (2002). [www.astm.org](http://www.astm.org).
- [30] Gyorgy Vizkelethy. personal correspondence, November 2010.
- [31] Ziegler J.F., Biersack J.P., and Ziegler M.D. *The Stopping and Range of Ions in Solids*. Pergamon Press, New York, NY, 2009.
- [32] Keithley, 28775 Aurora Rd., Solon, Ohio, 44139. *Model 4200 Semiconductor Characterization System Reference Manual*, September 2010. Available: at <http://www.keithley.com>.
- [33] Keithley, 28775 Aurora Rd. Solon, Ohio 44139. *Model 590 CV Analyzer Instruction Manual*, February 1999. Available: at <http://www.keithley.com>.
- [34] Boonton, 25 Eastmans Rd. Parsippany, New Jersey 07054. *Model 7200 Capacitance Meter Instruction Manual*, December 1995. Available: at <http://www.boonton.com>.

- [35] Byoung Hun Lee, Laegu Kang, Wen-Jie Qi, Renee Nieh, Yongjoo Jeon, Katsunori Onishi, and J.C. Lee. Ultrathin hafnium oxide with low leakage and excellent reliability for alternative gate dielectric application. In *Electron Devices Meeting, 1999. IEDM Technical Digest. International*, pages 133–136, 1999.
- [36] M. Mayer. Simnra, a simulation program for the analysis of nra, rbs and erda. Proceedings of the 15th International Conference on the Application of Accelerators in Research and Industry, J. L. Duggan and I.L. Morgan (eds.), American Institute of Physics Conference Proceedings 475, 1999.
- [37] Jim Banks. personal email correspondence, January 2011.
- [38] Chu Wei-Kan, Mayer J.W., and Nicolet M.A. *Backscattering Spectrometry*. Academic Press, New York, NY, 1978.
- [39] Wang Yongqiang and Nastasi M.A. *Handbook of Modern Ion Beam Materials Analysis*. Materials Research Society, New York, NY, 2009.
- [40] Schroder Dieter K. *Semiconductor Material and Device Characterization*. John Wiley and Sons Inc., Hoboken, NJ, 2006.
- [41] *CRC handbook on Chemistry and Physics*. Taylor and Francis Group, 2008.
- [42] Pierret R.F. and Small D.W. A modified linear sweep technique for mos-c generation rate measurements. *IEEE Transactions on Electron Devices*, 22(11):1051–1052, November 1975.
- [43] Marinella M.J., Schroder D.K., Chung G.Y., Loboda M.J., Isaacs-Smith T., and Williams J.R. A probe-lift mos-capacitor technique for measuring very low oxide leakage currents and their effect on generation lifetime extraction. *Electron Devices, IEEE Transactions on*, 55(2):565–571, February 2008.
- [44] Baliga B.J. and Adler M.S. Lifetime profile measurements in diffused layers. In *1977 International Electron Devices Meeting*, volume 23, page 505, 1977.
- [45] B.J. Baliga and M.S. Adler. Measurement of carrier lifetime profiles in diffused layers of semiconductors. *IEEE Transactions on Electron Devices*, 25(4):472–477, April 1978.

<b>REPORT DOCUMENTATION PAGE</b>				<i>Form Approved</i> OMB No. 074-0188	
<p>The public reporting burden for this collection of information is estimated to average 1 hour per response, including the time for reviewing instructions, searching existing data sources, gathering and maintaining the data needed, and completing and reviewing the collection of information. Send comments regarding this burden estimate or any other aspect of the collection of information, including suggestions for reducing this burden to Department of Defense, Washington Headquarters Services, Directorate for Information Operations and Reports (0704-0188), 1215 Jefferson Davis Highway, Suite 1204, Arlington, VA 22202-4302. Respondents should be aware that notwithstanding any other provision of law, no person shall be subject to a penalty for failing to comply with a collection of information if it does not display a currently valid OMB control number.</p> <p><b>PLEASE DO NOT RETURN YOUR FORM TO THE ABOVE ADDRESS.</b></p>					
<b>1. REPORT DATE (DD-MM-YYYY)</b> 24-03-2011		<b>2. REPORT TYPE</b> Master's Thesis		<b>3. DATES COVERED (From - To)</b> Jun 2010-Mar 2011	
<b>4. TITLE AND SUBTITLE</b>  Radiation Effects on the Electrical Properties of Hafnium Oxide Based MOS Capacitors				<b>5a. CONTRACT NUMBER</b>	
				<b>5b. GRANT NUMBER</b>	
				<b>5c. PROGRAM ELEMENT NUMBER</b>	
<b>6. AUTHOR(S)</b>  Foster, Jesse, C., Capt., USAF				<b>5d. PROJECT NUMBER</b>	
				<b>5e. TASK NUMBER</b>	
				<b>5f. WORK UNIT NUMBER</b>	
<b>7. PERFORMING ORGANIZATION NAMES(S) AND ADDRESS(S)</b>  Air Force Institute of Technology Graduate School of Engineering and Management (AFIT/EN) 2950 Hobson Way WPAFB OH 45433-7765				<b>8. PERFORMING ORGANIZATION REPORT NUMBER</b>  AFIT/GNE/ENP/11-M07	
<b>9. SPONSORING/MONITORING AGENCY NAME(S) AND ADDRESS(ES)</b> Defense Threat Reduction Agency COL Mark Mattox 1900 Wyoming Blvd SE Kirtland AFB, NM 87117-5669				<b>10. SPONSOR/MONITOR'S ACRONYM(S)</b> DTRA/OP-CSU	
				<b>11. SPONSOR/MONITOR'S REPORT NUMBER(S)</b>	
<b>12. DISTRIBUTION/AVAILABILITY STATEMENT</b> APPROVED FOR PUBLIC RELEASE; DISTRIBUTION UNLIMITED					
<b>13. SUPPLEMENTARY NOTES</b>					
<b>14. ABSTRACT</b> Hafnium oxide-based MOS capacitors were investigated to determine electrical property response to radiation environments. In situ capacitance versus voltage measurements were analyzed to identify voltage shifting as a result of changes to trapped charge with increasing dose of gamma, neutron, and ion radiation. In situ measurements required investigation and optimization of capacitor fabrication to include dicing, cleaning, metalization, packaging, and wire bonding. A top metal contact of 200 angstroms of titanium followed by 2800 angstroms of gold allowed for repeatable wire bonding and proper electrical response. Gamma and ion irradiations of atomic layer deposited hafnium oxide on silicon devices both resulted in a midgap voltage shift of no more than 0.2 V toward less positive voltages. This shift indicates recombination of radiation induced positive charge with negative trapped charge in the bulk oxide. Silicon ion irradiation caused interface effects in addition to oxide trap effects that resulted in a flatband voltage shift of approximately 0.6 V also toward less positive voltages. Additionally, no bias dependent voltage shifts with gamma irradiation and strong oxide capacitance room temperature annealing after ion irradiation was observed. These characteristics, in addition to the small voltage shifts observed, demonstrate the radiation hardness of hafnium oxide and its applicability for use in space systems.					
<b>15. SUBJECT TERMS</b> Hafnium Oxide, MOS Capacitors, gamma radiation, ion radiation					
<b>16. SECURITY CLASSIFICATION OF:</b>			<b>17. LIMITATION OF ABSTRACT</b>  UU	<b>18. NUMBER OF PAGES</b>  115	<b>19a. NAME OF RESPONSIBLE PERSON</b> LTC John McClory
a. REPORT U	b. ABSTRACT U	c. THIS PAGE U			<b>19b. TELEPHONE NUMBER (Include area code)</b> (937)255-6565, ext 7308 (john.mcclory@afit.edu)